

Fall 2018

# Investigation of the Performance and Emissions Characteristics of Dual Fuel Combustion in a Single Cylinder IDI Diesel Engine

Johnnie L. Williams Jr

Follow this and additional works at: <https://digitalcommons.georgiasouthern.edu/etd>



Part of the [Computer-Aided Engineering and Design Commons](#), and the [Heat Transfer, Combustion Commons](#)

---

## Recommended Citation

Williams, Johnnie, "Investigation of the Performance and Emissions Characteristics of Dual Fuel Combustion in a Single Cylinder IDI Diesel Engine" (2019). Electronic Theses and Dissertations. 2991.

This thesis (open access) is brought to you for free and open access by the Graduate Studies, Jack N. Averitt College of at Digital Commons@Georgia Southern. It has been accepted for inclusion in Electronic Theses and Dissertations by an authorized administrator of Digital Commons@Georgia Southern. For more information, please contact [digitalcommons@georgiasouthern.edu](mailto:digitalcommons@georgiasouthern.edu).

INVESTIGATION OF THE PERFORMANCE AND EMISSIONS CHARACTERISTICS OF  
DUAL FUEL COMBUSTION IN A SINGLE CYLINDER IDI DIESEL ENGINE

by

JOHNNIE LEE WILLIAMS JR

(Under the Direction of Valentin Soloiu)

ABSTRACT

Restrictions in the allowable exhaust gas emissions of diesel engines has become a driving factor in the design, development, and implementation of internal combustion (IC) engines. A dual fuel research engine concept was developed and implemented in an indirect injected engine in order to research combustion characteristics and emissions for non-road applications. The experimental engine was operated at a constant speed and load 2400 rpm and 5.5 bar indicated mean effective pressure (IMEP). n-Butanol was port fuel injected at 10%, 20%, 30%, and 40% by mass fraction with neat ultra-low sulfur diesel (ULSD#2). Peak pressure, maximum pressure rise rates, and heat release rates all increased with the increasing concentration of n-Butanol. MPRR increased by 127% and AHRR increased by 30.5% as a result of the shorter ignition delay and combustion duration. Ignition delay and combustion duration were reduced by 3.6% and 31.6% respectively. This occurred despite the lower cetane number of n-Butanol as a result of increased mixing due to the port fuel injection of the alcohol. NO<sub>x</sub> and soot were simultaneously reduced by 21% and 80% respectively. Carbon monoxide and unburned hydrocarbons emissions were increased for the dual fuel combustion strategies due to valve overlap. Results display large emission reductions of harmful pollutants, such as NO<sub>x</sub> and soot.

INDEX WORKS: Combustion, Port fuel injection, Emissions, Diesel, NO<sub>x</sub>, n-Butanol, Soot,  
Dual fuel combustion

INVESTIGATION OF THE PERFORMANCE AND EMISSIONS CHARACTERISTICS OF DUAL  
FUEL COMBUSTION IN A SINGLE CYLINDER IDI DIESEL ENGINE

by

JOHNNIE LEE WILLIAMS JR

B. S., Georgia Southern University, 2018

A Thesis Submitted to the Graduate Faculty of Georgia Southern University in Partial

Fulfillment of the Requirements for the Degree

MASTER OF SCIENCE

STATESBORO, GEORGIA

©2018

JOHNNIE WILLIAMS

All Rights Reserved

INVESTIGATION OF THE PERFORMANCE AND EMISSIONS CHARACTERISTICS OF DUAL  
FUEL COMBUSTION IN A SINGLE CYLINDER IDI DIESEL ENGINE

by

JOHNNIE LEE WILLIAMS JR

Major Professor: Valentin Soloiu

Committee: Marcel Ilie

Mosfequr Rahman

Electronic Version Approved:

December 2018

## DEDICATION

To my family support who has encouraged me along every step of my journey  
and my girlfriend Anya for her continued and future support.

## ACKNOWLEDGMENTS

I would like to acknowledge with sincere gratitude Dr. Valentin Soloiu for his time, effort, advice, and support in the preparation and execution of this research and thesis project. Thanks go to all of the faculty and staff of the Allen E. Paulson Department of Mechanical at Georgia Southern University. Thanks to the entire Automotive and Aerospace Combustion laboratory as well. Special thanks to Cesar Carapia and Ryan Davis for their support.



## TABLE OF CONTENTS

ACKNOWLEDGMENTS.....	3
LIST OF TABLES .....	7
LIST OF FIGURES.....	9
LIST OF EQUATIONS .....	12
ABBREVIATIONS.....	13
CHAPTER 1: INTRODUCTION .....	17
1.1 Diesel Engines.....	17
1.2 Diesel Exhaust Emissions .....	19
1.3 Statement of the Purpose.....	24
1.4 Hypothesis.....	25
CHAPTER 2: LITERATURE REVIEW .....	26
2.1 Renewable Energy Policy .....	26
2.2 Non-road Engines.....	27
2.3 Alcohol Fumigation in Internal Combustion Engines.....	27
2.4 n-Butanol.....	35
CHAPTER 3: METHODOLOGY .....	36
3.1 Overview .....	36
3.2 Research Implementation.....	36
3.3 Fuel Analysis.....	37

3.4 Engine Operating Procedures .....	42
3.5 Experimental Engine Setup .....	43
3.5.1 Pressure Transducers .....	48
3.5.2 Charge Amplifier .....	56
3.5.3 Rotary Encoder .....	57
3.5.4 Temperature .....	58
3.5.5 Flow Meters .....	59
3.5.6 Emissions Analyzers .....	63
3.6 Port Fuel Injection System Design .....	65
3.6.1 Intake Manifold Design .....	67
3.6.2 Injector Selection and Calibration .....	74
3.6.3 ECU Selection and Programming .....	79
3.6.4 Trigger Mechanism Design .....	83
3.7 Metrics for Success .....	86
CHAPTER 4: DATA ANALYSIS .....	87
4.1 Fuel Properties .....	87
4.1.1 Dynamic Viscosity .....	88
4.1.2 Ignition Quality .....	89
4.1.3 Thermo-Gravimetric and Differential-Thermal Analysis .....	93
4.1.4 Mie Scattering Spray Analysis .....	96

4.2 Thermodynamic Combustion Analysis .....	98
4.2.1 Combustion Pressure .....	98
4.2.2 Apparent Heat Release .....	101
4.2.3 Mass Fraction Burned.....	105
4.2.4 Instantaneous Volume Averaged Maximum Gas Temperature .....	107
4.2.5 Ringing Intensity.....	109
4.2.6 Cylinder Heat Fluxes and Heat Transfer .....	110
4.3 Emissions and Efficiencies Investigation.....	114
4.3.1 Nitrogen Oxides and Soot.....	114
4.3.2 Carbon Monoxide and Unburned Hydrocarbons .....	117
4.3.3 Aldehyde Emissions .....	120
4.3.4 Efficiencies and Specific Fuel Consumption .....	121
CHAPTER 5: CONCLUSIONS .....	124
5.1 Conclusions .....	124
5.2 Future Work .....	126
REFERENCES .....	128

## LIST OF TABLES

Table I: Nonroad Compression Ignition Engines: Exhaust Emission Standards.....	20
Table II: Kubota Engine Specifications .....	46
Table III: Kistler Type 6056A Specifications.....	50
Table IV: Kistler Type 6053CC Specifications .....	52
Table V: Kistler Type 6229A Transducer Specifications.....	55
Table VI: Technical Data for Kistler 5010B Amplifier.....	57
Table VII: MKS Main Measured Species.....	63
Table VIII: Port Fuel Injection System Components .....	66
Table IX: Boundary Conditions.....	69
Table X: Mesh Validation and Analytical Solution Comparison.....	70
Table XI: Simulation Convergence Criteria .....	71
Table XII: PL2-155 Injector Specifications.....	76
Table XIII: Main Injector Mass Flow Rate at 2400 RPM .....	78
Table XIV: Total Fuel Mass Flow Rate at 2400 RPM .....	78
Table XV: Fuel Mass Flow Rate for the Port Fuel Injector at 2400 RPM .....	78
Table XVI: Port Fuel Injector Duration at 2400 RPM .....	79
Table XVII: Frequency Analysis Results 3000 RPM.....	86
Table XVIII: Fuel Properties .....	87
Table XIX: Thermal Gravimetric Analysis .....	95
Table XX: Particle Size Distribution by Volume ( $\mu\text{m}$ ) .....	97
Table XXI: Maximum Combustion Pressure and Respective Crank Angle .....	100
Table XXII: Maximum Apparent Heat Release Rate and Respective CAD .....	105

Table XXIII: Mass Fraction Burned .....	107
Table XXIV: Combustion Duration.....	107

## LIST OF FIGURES

Figure 1 Composition of Diesel Exhaust Gases .....	21
Figure 2 Composition of Particulate Matter in Diesel Exhaust Gases.....	22
Figure 3 Brookfield Viscometer and Shell and Tube Heat Exchanger.....	38
Figure 4 Parr 6772 Digital Calorimeter .....	39
Figure 5 Shimadzu DTG-60 TGA-DTA .....	40
Figure 6 Malvern Spraytec Mie Scattering He-Ne Laser .....	41
Figure 7 PAC ID510 Combustion Chamber.....	42
Figure 8 Experimental Engine Schematic .....	44
Figure 9 Triple Vortex Combustion Chamber .....	45
Figure 10 Fuel Consumption, Power, and Torque vs. Engine Speed .....	47
Figure 11 Test Cell Setup .....	48
Figure 12 Kistler Main Chamber Transducer .....	49
Figure 13 Kistler Swirl Chamber Transducer.....	51
Figure 14 Kistler Glow Plug Adapter .....	53
Figure 15 Kistler Type 6229A Fuel Line Pressure Transducer .....	54
Figure 16 Kistler Clamp on Adapter.....	54
Figure 17 Kistler 5010B Dual Mode Charge Amplifier .....	56
Figure 18 Omron E6C2 Rotary Encoder .....	58
Figure 19 Omron E5CS Thermocouple Controllers .....	59
Figure 20 Meriam 50MC2 Series Laminar Flowmeter and Integral Flow Computer .....	60
Figure 21 Max Machinery P001 Piston Flow Meter .....	60
Figure 22 Arduino Mega2560 Microcontroller .....	61

Figure 23 Arduino Mass Flow Rate Sketch.....	62
Figure 24 Arduino Serial Monitor Displaying Flow Rate Measurements.....	63
Figure 25 MKS MultiGas 2030 FTIR.....	64
Figure 26 AVL 415s Smoke/Soot Meter .....	64
Figure 27 Port Fuel Injection System Schematic.....	67
Figure 28 CFD Residuals.....	71
Figure 29 Velocity Contour and PFI Pathlines .....	72
Figure 30 Intake Design 3D Model .....	73
Figure 31 Custom Intake Manifold and Injector.....	74
Figure 32 PL2-155 Peak and Hold Injector .....	75
Figure 33 Developed Injector Calibration Test Bench .....	75
Figure 34 PL2-155 Peak and Hold Injector Calibration Curves.....	76
Figure 35 Calibration Curves for the PL2-155 .....	77
Figure 36 Wire Schematic for Engine Control Unit.....	80
Figure 37 Sample Fuel Map from the EMS 8860.....	81
Figure 38 PL2-155 Port Fuel Injection Fuel Map Inputs.....	82
Figure 39 EMS 8860 Setup Parameters .....	82
Figure 40 VR Sensor Solid Model and Fabricated Part.....	84
Figure 41 Trigger Wheel Solid Model and Fabricated Part.....	84
Figure 42 Mass Evaluation of the Trigger Wheel .....	85
Figure 43 Campbell Plot of the Trigger Wheel.....	85
Figure 44 Viscosity vs. Temperature of All Tested Fuels .....	89
Figure 45 Combustion Pressure of ULSD and n-Butanol in a CVCC.....	90

Figure 46 Heat Release Rate of ULSD and n-Butanol in a CVCC .....	91
Figure 47 Combustion Temperature of ULSD and n-Butanol in a CVCC .....	92
Figure 48 TGA for ULSD#2 and n-Butanol .....	94
Figure 49 DTA for ULSD#2 and n-Butanol .....	95
Figure 50 Sauter Mean Diameter and Droplet Frequency Distribution .....	97
Figure 51 Maximum Combustion Pressure .....	99
Figure 52 Maximum Pressure Rise Rate .....	100
Figure 53 P-V Diagrams for CDC and 20% n-Butanol .....	101
Figure 54 Apparent Heat Release Rate .....	103
Figure 55 Apparent Heat Release Rate- Detail .....	104
Figure 56 Mass Fraction Burned .....	106
Figure 57 Instantaneous Volume Averaged Maximum Gas Temperature .....	108
Figure 58 Ringing Intensity .....	110
Figure 59 Heat Fluxes .....	112
Figure 60 Heat Losses for Conventional Diesel Combustion .....	113
Figure 61 Heat Losses for Dual Fuel Combustion at 40% of the Total Fuel Mass Flow Rate .....	114
Figure 62 Nitrogen Oxide Emissions for increasing n-Butanol Concentrations .....	115
Figure 63 Soot Emissions for increasing n-Butanol Concentrations .....	117
Figure 64 Carbon Monoxide Emissions for increasing n-Butanol Concentrations .....	118
Figure 65 Unburned Hydrocarbons Emissions for increasing n-Butanol Concentrations .....	119
Figure 66 Formaldehyde Emissions for increasing n-Butanol Concentrations .....	120
Figure 67 Mechanical and Thermal Efficiencies for increasing n-Butanol Concentrations .....	122
Figure 68 Diesel Equivalent BSFC for increasing n-Butanol Concentrations .....	123



## LIST OF EQUATIONS

Equation 1 .....	21
Equation 2 .....	21
Equation 3 .....	21
Equation 4 .....	69
Equation 5 .....	69
Equation 6 .....	69
Equation 7 .....	69
Equation 8 .....	69
Equation 9 .....	70
Equation 10 .....	74
Equation 11 .....	74
Equation 12 .....	92
Equation 13 .....	102
Equation 14 .....	109
Equation 15 .....	111
Equation 16 .....	111
Equation 17 .....	111
Equation 18 .....	111
Equation 19 .....	122

## ABBREVIATIONS

A – cylinder area

AHRR – apparent heat release rate

ASTM - American Society for Testing and Materials

ATDC – After Top dead center

BSFC - brake specific fuel consumption

BTDC – Before top dead center

CA10 – crank angle for 10% mass fraction burned

CA50 – crank angle for 50% mass fraction burned

CA90 – crank angle for 90% mass fraction burned

CAD - crank angle degree [deg.]

CD – combustion duration

CDC – conventional diesel combustion

CI – compression ignition

CN - Cetane Number

CO - Carbon monoxide

CO<sub>2</sub> - Carbon dioxide

cP – centipoise

CVCC – constant volume combustion chamber

d – derivative term

D - bore [mm]

DCN – derived cetane number

DAQ - data acquisition system

DOC - diesel oxidation catalyst

DPF - diesel particulate filter

DTA - differential thermal analysis

$Dv(10)$  – largest droplet size of 10% of the fuel spray volume

$Dv(50)$  – largest droplet size of 50% of the fuel spray volume

$Dv(90)$  – largest droplet size of 90% of the fuel spray volume

EGR - exhaust gas recirculation

EPA - Environmental Protection Agency

ESFC – energy specific fuel consumption

$i$  - number of cylinders

IC – internal combustion

IMEP - indicated mean effective pressure

ITE – indicated thermal efficiency

kW-h – kilowatt-hour

LHV - lower heating value

$N$  - engine speed [rpm]

NMHC – non methane hydrocarbons

$NO_x$  - nitrous oxides

$P$  – combustion pressure

$P_e$  - engines effective power [kW]

PFI – port fuel injection

PM – Particulate matter (PM10 less than 10 microns, 2.5 less than 2.5 microns)

$Q$  – heat release

R – ideal gas constant

Re - in-cylinder Reynolds number

RI – ringing intensity

rpm – rotations per minute

S - stroke [mm]

SCR – selective catalytic reduction

SI – spark ignition

SMD – Sauter mean diameter

SOI - Start of Injection

T<sub>A</sub> – Cylinder volume-averaged instantaneous gas temperature [K]

T<sub>w</sub> - cylinder wall average temperature [K]

TA10 – temperature at which 10% of the fuel vaporized

TA50 – temperature at which 50% of the fuel vaporized

TA90 – temperature at which 90% of the fuel vaporized

TDC - top dead center

TGA - thermal-gravimetric analysis

UHC - unburned hydrocarbons

ULSD# 2 - Ultra low sulfur diesel #2

V – Volume in heat release equation

$\alpha$  - crank angle degree (heat transfer and piston slap)

$\beta$  - ringing intensity constant

$\varepsilon$  - emissivity

$\gamma$  - specific heat of air

$\lambda_A$  thermal conductivity of air

$\sigma$  - Stefan- Boltzmann constant

$q$  - heat flux

$\omega$  - angular velocity

$\rho$  - density of in-cylinder gas [ $\text{kg/m}^3$ ]

$\theta$  - crank angle degree

## CHAPTER 1: INTRODUCTION

### 1.1 Diesel Engines

Internal combustion engines provide mechanical power by harvesting the chemical energy contained in the combusted fuel. The fuel-air mixture, and combustion products serve as the working fluids. The engine's output comes from the work transfer between these fluids and the mechanical components of the engine (Heywood 1988). Two engine design concepts lead the engine market. These are the compression ignition (CI) engine and the spark ignition (SI) engine. The prevalence of the two designs comes from their simplicity, ruggedness, and high power to weight ratios (Norman 2016).

Heat engines have existed in one form or another for over two and a half centuries, but it wasn't until the 1860s that innovations in design made them a practical reality. Early engines used steam in addition to fuel and air as a working fluid. J.J. E. Lenoir (1822-1900), is credited with developing the first marketable engine of this type. The first half of the piston stroke inducted gas and air. During the second half of the stroke a spark was used to initiate combustion. Combustion products would be cleared from the cylinder during the second stroke (Cummins 1976).

Efficiencies for these engines were at best 5%. In 1867 Nicolaus A. Otto (1832-1891) and Eugen Langens (1833-1895) introduced their atmospheric engine. The pressure rise on the power producing stroke was used to accelerate a free piston and rack assembly and generate a vacuum in cylinder with atmospheric pressure on the other side. The pressure gradient created moved the piston and generated mechanical power. This allowed for thermal efficiencies of up to 14%.

In 1876 Otto released a prototype that made use of four strokes per cycle. This allowed for a reduction in the weight and volume of the engine and an increase in efficiency. This breakthrough

is credited as being the beginning of the modern IC engine industry. Five years prior Alphonse Beau de Rochas (1815-1893) filled a patent which described the four stroke process implemented by Otto. Despite this Otto is credited as the inventor of the modern IC engine because he actually put the idea into practice (Heywood 1988).

In 1892 following Otto's developments for SI engines, Rudolf Diesel (1858-1913) proposed a compression ignition concept. Diesel drew inspiration for his engine design from Nicholas Carnot's idea of a cycle in heat engine operation (Norman 2016). In Diesel's concept fuel is injected into compressed air in cylinder at high temperatures and pressures which causes the liquid fuel to auto ignite. This concept allowed him to increase efficiency to 30%. The increase was a result of higher compression ratios and a more stoichiometric air-fuel charge (Heywood 1988).

Diesel unveiled his engine to the public in Munich in 1898. Interest was high and Diesel immediately sold licensing rights to companies in France, England, Germany, Russia, and the United States. Early applications for his engine were focused on marine applications. The size of the engine as well as the requirements for the auxiliary systems made it impractical for use in automobiles. The first seafaring diesel powered-ship made its' maiden voyage from England to Bangkok in 1912. The 7000 ton Danish Selandia was powered by two 1000 horsepower, eight cylinder diesel engines (Norman 2016).

Two key milestones led to the development of the automotive diesel engine. In the 1920s solid fuel injection was perfected. This allowed for fuel to be injected directly into the combustion chamber without the use of an air compressor. Bosch in Stuttgart developed a compact and more reliable fuel pump. These developments allowed for the production of smaller, lighter, and faster

diesel engines. With these breakthroughs in technology Daimler-Benz introduced the first production model diesel automobile in 1936 (Norman 2016).

Diesel engines can be classified according to their injection method. Direct injection (DI) engines inject fuel directly into the combustion chamber. This is advantageous because it reduces heat loss. This combined with more precise fuel metering increases fuel efficiency. Direct injection engines also have better cold start behavior. Direct injection methods can increase the costs of injectors due to the high injection pressure required to inject in cylinder. They also increase particulate matter emissions.

Indirect injection (IDI) works by injecting fuel into a smaller combustion chamber, often called a precombustion or swirl chamber, connected to the main combustion chamber by a narrow throat (Stone 1993). This allows for an increase in mixing as the working fluid heats up and expands through the throat into the main chamber. The increase in air speed as the fluid passes through the narrow throat is what promotes the increased mixing. This speeds up the combustion process allowing for an increase in power output due to an increase in engine operating speeds. These engines are easier to design and manufacture due to more flexible tolerances, and lower injection pressures. Indirect injection suffers from lower fuel efficiencies due to heat loss from increased surface area, and poor cold start behavior (Dempsey 2007).

## 1.2 Diesel Exhaust Emissions

Exhaust emissions from IC engines reduce environmental protection and contribute to climate change and air pollution. The transportation sector is one of the main producers of environmental pollution. The transportation sector is responsible for over 55% of NO<sub>x</sub> emissions 10% of VOCs, and 10% of PM<sub>2.5</sub> and PM<sub>10</sub> emissions in the U.S. (EPA 2014) Organizations like



the Environmental Protection Agency (EPA) and the California Air Resources Board (CARB) set and enforce regulations to reduce the impact of tailpipe emissions. EPA emissions standards for nonroad compression ignition engines producing 8 kW of power or less can be seen in Table I below.

**Table I:** Nonroad Compression Ignition Engines: Exhaust Emission Standards  
(Environmental Protection Agency 2016)

<b>Rated Power (kW)</b>	<b>Tier</b>	<b>Model Year</b>	<b>NMHC + NO<sub>x</sub> (g/kWh)</b>	<b>PM (g/kWh)</b>	<b>CO (g/kWh)</b>
<b>≤ 8 kW</b>	<b>1</b>	2000 – 2004	10.5	1.0	8.0
	<b>2</b>	2005 – 2007	7.5	0.80	8.0
	<b>4</b>	2008+	7.5	0.40	8.0

Diesel exhaust pollutants account for 1% of the total exhaust gases produced. These pollutant gases are primarily composed of nitrogen oxides and particulate matter. NO<sub>x</sub> accounts for up to 50% of exhaust gas pollution. Hydrocarbon and carbon monoxide emissions are kept to a minimum due to the lean burning nature of diesel combustion. Sulfur dioxide is also reduced due to the implementation of ultra-low sulfur diesel.

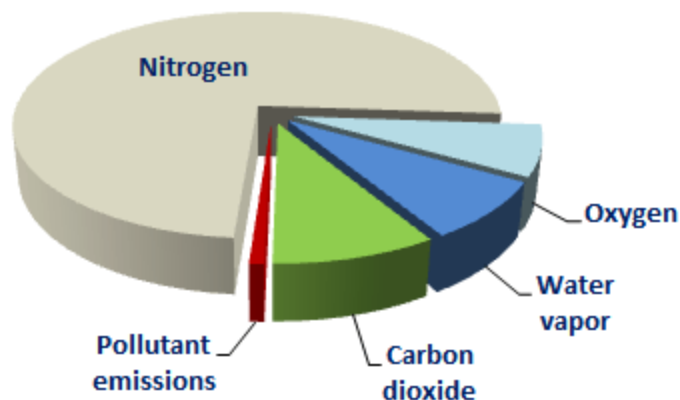


**Figure 1** Composition of Diesel Exhaust Gases (Majewski 2012)

Principle diesel exhaust emissions include water (12%), diatomic oxygen (17%), diatomic nitrogen (58%), and carbon dioxide (12%). CO<sub>2</sub> is of great concern due to its environmentally hazardous effects as a greenhouse gas.

Nitrogen oxides are composed of nitrogen oxide (NO) and nitrogen dioxide (NO<sub>2</sub>). NO constitutes up to 85 – 95% of NO<sub>x</sub> (Majewski and Khair 2006). NO is a colorless and odorless gas while NO<sub>2</sub> is a reddish brown gas with a pungent odor. NO is principally produced from the oxidation of atmospheric nitrogen. NO can be produced from the oxidation of fuel nitrogen but the contribution is minimal and the mechanism by which it forms isn't very well understood. NO formation is a temperature dependent reaction happening at temperatures above 1600 °C through the Zeldovich mechanism presented below (Heywood 1988).



Most of the NO<sub>x</sub> formation occurs early in the combustion process when the piston is near top dead center where in-cylinder pressures and temperatures are the highest. NO<sub>x</sub> is hazardous to the environment because it contributes to ozone formation and smog formation which can also develop into acid rain. Nitrogen oxide emissions also pose a health risk to people as they can contribute to lung disease. (EPA 1999).

Particulate matter in compression ignition engines is a carbonaceous material called soot. It is produced from the incomplete combustion of hydrocarbon fuel and to a lesser extent lubricating oil. Soot is principally clusters of smaller particles of carbon and hydrogen with individual diameters of 15 to 30 nm (Heywood 1988). The formation of soot is dependent on many factors such as the combustion and expansion processes, sulfur content, ash content, lubrication oil quality, combustion temperature, and exhaust gas cooling (Burtscher 2005). Typical particle composition of a heavy-duty diesel engine is classified as 41 % carbon, 7 % unburned fuel, 25 % unburned oil, 14 % sulfate and water, 13 % ash and other components.

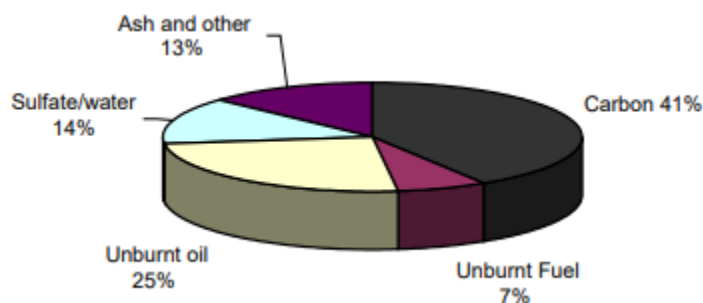


**Figure 2** Composition of Particulate Matter in Diesel Exhaust Gases (Kittelson 1998)

Particle size is directly linked to their potential health effects. Particles less than 10  $\mu\text{m}$  in diameter pose the greatest risk because they can get deep into the lungs and may even pass into the bloodstream causing heart complications. Larger particles pose less danger, but they can still irritate your eyes, nose, and throat (EPA 2003). These emissions contribute to pollution of air,

water, and soil; soiling of buildings; reductions in visibility; impact agriculture productivity; global climate change. The World Health Organization estimated that around 2.4 million people die every year due to air pollution (WHO 2007).

Carbon monoxide emissions result from the incomplete combustion of fuel. The concentration of CO is dependent on the air/fuel equivalence ratio. CO emissions are highest in fuel rich mixtures where  $\lambda$  is less than 1. Diesel combustion is a lean operation where CO emissions are generally low. In dual fuel combustion modes, CO can increase due to the low reactivity fuel's partial oxidation and unburned fuel entering the exhaust due to valve overlap (Soloiu and Moncada<sup>B</sup> 2018). CO is also produced if the droplets in a diesel engine are too large or if insufficient turbulence or swirl is created in the combustion chamber. CO concentrations increase greatly in fuel rich combustion because there is an oxygen deficiency and all the carbon cannot be converted to CO<sub>2</sub> (Resitoğlu and Altinisik 2016). Carbon monoxide is an odorless and colorless gas. In humans, CO binds to hemoglobin and inhibits its ability to transfer oxygen leading to asphyxiation. This can result in impaired concentration, slow reflexes, and confusion (CDC 2017).

Unburned hydrocarbon emissions also known as organic emissions, are produced from the incomplete combustion of hydrocarbon fuel. Factors that influence UHC emissions include temperature and mixing (Heywood 1988). Hydrocarbon emissions are higher at idle or part load. Under these conditions the quantity of mixture at the perimeter of the reaction zone is too lean to burn. Under-mixing or over-fueling can also increase UHC concentration by creating a rich air/fuel mixture (Stone 1993). Engine exhaust fumes contain a wide variety of hydrocarbon compounds with varying levels of toxicity. They can contribute to the formation of ground level ozone, and have the potential to cause respiratory tract irritation and cancer (Krzyzanowski et al 2005).

Exhaust gas after-treatment systems used to treat the exhaust gases from diesel combustion include diesel oxidation catalysts (DOC), diesel particulate filters (DPF), and selective catalytic reduction (SCR) systems. SCR technology is used for the reduction of nitrogen oxide emissions.  $\text{NO}_x$  is reduced to water and  $\text{N}_2$  through the use of urea. Lean  $\text{NO}_x$  traps (LNT) reduce  $\text{NO}_x$  emissions under lean operating conditions. During lean operation the LNT stores  $\text{NO}_x$  on a catalyst wash coat. Under rich operating conditions the  $\text{NO}_x$  emissions are released and allowed to react by the usual three-way reaction.

The primary function of a DOC is to oxidize CO and UHC emissions. They also play a role in the reduction of particulate matter by oxidizing some of the HC that would be absorbed into the carbon particles (Wang et al. 2008). CO and HC are oxidized to form  $\text{CO}_2$  and  $\text{H}_2\text{O}$ . DOCs also oxidize NO to form  $\text{NO}_2$ . The increase in  $\text{NO}_2$  in the exhaust gases increases efficiency of downstream reduction technology like SCR and DPF. DPF remove particulate matter from exhaust gas through physical filtration. As the filters accumulate PM negative effects can take hold such as increased fuel consumption, engine failure, and stress in the filter. To prevent these negative effects, the DPF has to be regenerated by burning trapped PM (Resitoğlu and Altinisik 2015).

### 1.3 Statement of the Purpose

Federal regulations covering tailpipe emissions are some the most challenging design constraints placed on engine manufacturers today. Depleting petroleum reserves also create concerns regarding energy security. Dual fuel combustion strategies were developed to operate in low temperature combustion regions where  $\text{NO}_x$  and particulate matter production is reduced. Dual fuel strategies can make use of fuels from both fossil fuels and renewable resources. Bio-butanol fermented from energy crops and agricultural byproducts in the south east present an

immediate and sustainable solution over current petroleum based fuels. *This study is the first investigation into the combustion properties of dual fuel combustion using ultra-low sulfur diesel and n-butanol in an indirect injection diesel engine.* It is being done to understand the combustion characteristics that relate to low emission levels to potentially find a replacement for diesel fuel in the future.

#### 1.4 Hypothesis

If a dual fuel combustion strategy involving the port fuel injection of n-butanol is used in conjunction with the indirect injection of ultra-low sulfur diesel, then engine out emissions for nitrogen oxides and particulate matter in single cylinder, off-road diesel engines can be reduced below Tier 4 EPA standards while maintaining engine performance.

## CHAPTER 2: LITERATURE REVIEW

### 2.1 Renewable Energy Policy

The United States transportation sector consumes 68% of the nation's total energy demand. This is expected to rise to 73% by the year 2030 (Soloiu 2015). The growing demand for petroleum products, decrease in finite fossil fuel reserves, and instability in petroleum-rich countries have led to uncertainty in the cost and availability of energy. As a result, the development of alternative transportation fuels has become a national priority. The 2007 Energy Independence and Security Act established regulations and programs to move the U.S. toward a secure and energy independent state. The act sought to increase the production, development, and infrastructure of renewable fuels. The EISA fuel economy standards required that automakers reach a minimum average fuel economy for all passenger vehicles in increasing proportion per year. With the mandate stating that the total fleet reach an average of 35 mpg by the year 2020 (U.S. Energy Information Administration, 2014). It also established a goal of 36 billion barrels of biofuel to be blended into fossil fuel resources by 2022 (EISA 2007).

Alternative fuels are also of interest from an environmental perspective. Legislative bodies like the Environmental Protection Agency and a California Air Resources Board were established to investigate and address the impact of energy production on human health and the environment. Legislation like the Clean Air Act of 1970 was established to address concerns surrounding the byproducts produced from the burning of fossil fuels. Revisions to the act were made in 1977 and 1990 to address the newly recognized issues of smog, acid rain, and ozone layer depletion. EPA established a tier system for the systematic reduction of tailpipe emissions. Tier 1, 2 3, and 4 standards were enacted in 1998, 2004, 2006, and 2008. Since The passing of the Clean Air Act of

1970 stationary source pollution from industry has been reduced by nearly 70%. Mobile source pollution from automobiles has been reduced by more than 90%. These reductions have caused the six most commonly found air pollutants to decrease by more than 50 percent (EPA 2007). Although great progress has been made in addressing the negative impacts of burning fossil fuels areas of possible improvement still exist.

## 2.2 Non-road Engines

Small displacement non-road engines have been found by the EPA to cause a significant amount of air pollution. EPA research (EPA 2008) concluded that 26% of mobile source volatile organic compound (VOC) emissions and 23% of mobile source carbon monoxide emissions are produced by these engines. Mobile source pollution includes cars, light and heavy trucks, buses, non-road recreational vehicles, farm and construction equipment, marine engines, aircraft, locomotive and lawn and garden equipment. This is a substantial contribution when the broad definition of mobile source is taken into account. Road vehicle emissions have been regulated for decades. New policy has shifted the focus to off road vehicles. One possible approach to the problem is the implementation of dual fuel combustion.

## 2.3 Alcohol Fumigation in Internal Combustion Engines

Fossil fuels have a major impact on the sphere of modern civilization including industrial development, transportation, and power generation. The rapid increase in use of fossil fuel over the past two centuries has destructive effects on environment. The depletion of reserves coupled with the increase in consciousness has created a drive to reduce emissions while preserving performance. The scope of research into dual fuel combustion strategies for compression ignition engines is split between fuel blends and fuel fumigation. Fuel blends involves the mixing of fuel



before injection. Fumigation techniques involve the injection of a secondary fuel into the intake air charge. This literature review will focus on the fumigation aspect of dual fuel combustion. Relevant research first explored fumigation using gasoline, and then alcohol, and natural gas as the secondary fuel. Due to the scope of my research this literature review will focus on alcohol fumigation. Alcohol fumigation is a dual fuel engine operation technology in which alcohol fuels are premixed with incoming air (Imran 2013). Alcohol fumigation is being explored as an effective measure to reduce emissions from diesel engine vehicles.

Park et al (2014) examined the effects of bioethanol and gasoline as a premixed injection source on the combustion performance and exhaust emissions characteristics of a dual-fuel combustion engine. The ignition source of dual-fuel combustion was biodiesel derived from soybean oil. The premixing ratio was calculated based on the total input energy and was varied from 0.2 through 0.8. Experimental results show that dual-fuel combustion had a higher maximum combustion pressure, shorter ignition delay, significantly lower NO<sub>x</sub>, and soot emissions. Hydrocarbon and carbon monoxide emissions were shown to increase when compared to single-fuel combustion. In a comparison of bioethanol and gasoline during dual-fuel combustion, biodiesel–bioethanol dual-fuel combustion showed lower maximum pressure, longer ignition delay, and higher IMEP than biodiesel–gasoline dual-fuel combustion. The increase in the premixing ratio for both dual-fuel combustion modes increased the ignition delay and IMEP, and decreased the maximum combustion pressure. With the increase in the premixing ratio, fuel consumption increased during biodiesel–gasoline dual-fuel combustion, but decreased during biodiesel–bioethanol dual-fuel combustion. NO<sub>x</sub> significantly decreased during biodiesel–bioethanol dual-fuel combustion; however, biodiesel–gasoline dual-fuel combustion had a limited effect on NO<sub>x</sub> reduction. Hydrocarbon and carbon monoxide emissions were increased by

bioethanol or gasoline premixing. The biodiesel–bioethanol dual-fuel combustion mode showed higher hydrocarbon emissions than the biodiesel–gasoline dual-fuel combustion mode, and the carbon monoxide emission level was similar in both combustion modes.

Sarjovaara et al (2015) studied, E85 as the primary fuel in a dual-fuel combustion concept. The E85 blend was injected at low pressure into the intake manifold and the mixture was ignited via a diesel fuel injection near top dead center. The research engine was based on a heavy-duty diesel engine equipped with a common-rail injection system. Only the duration of the diesel injection was modified in the diesel injection system during the tests – the other diesel injection parameters were not changed. The goal was to study the possibilities of using the waste material-based E85 ethanol blend on dual-fuel concept as a promising future bio-fuel option. The results were promising, though the engine was not optimized for the combustion concept being studied and minimum modifications were done to the engine. High E85 rates (up to 89%) by energy content were achieved, especially under medium load conditions. On the high and low load portions were lower, but the E85 rates were higher than 30% even in these cases. For most of the cases, the limiting issue was the pressure rise rate, but in cases with the highest portions of E85 the limiting factor was the minimum quantity of the diesel fuel enabling two phase diesel fuel injection. In all cases the E85 increased carbon-monoxide and un-burned hydrocarbon emission, but the nitrogen oxide emission decreased simultaneously in most of the cases. Smoke emissions were low in all cases, but at highest E85 rate smoke emissions further decreased to near zero value.

Tutak et al (2015) investigated the impact of both methanol and E85 (85% ethanol and 15% gasoline) as additional fuels added to a diesel fueled engine on its combustion characteristics and exhaust emissions. These fuels were added by injection into an intake manifold in amounts expressed by their energy percentage of 20%, 50%, 75% and 90% with respect to total diesel fuel–

methanol or diesel fuel–E85 blends. The tests in a compression ignition engine contained analysis of heat release rate and combustion parameters as well as analysis of exhaust toxic emission NO<sub>x</sub>, THC, CO and soot. It was observed that with increase in methanol or E85 peak combustion temperature decreases as well as temperature of the mixture at the end of compression stroke that affects combustion duration. For methanol or E85 two characteristic peaks in the heat release rate profile were observed. The first peak represents burning the diesel fuel and the second burning methanol or E85. Hence, diesel fuel injection timing should be corrected, if alcohols, even in small amounts, are applied. Furthermore, as advantage, slight increase in brake efficiency was observed. Next, radical reduction in soot, particularly at 50% alcohol (methanol or E85) addition was also managed as important advantage. On the other hand, increase by 16% in NO<sub>x</sub> emission was observed, while 20% methanol or E85 were added. Summing up, addition of methanol or E85 to the diesel fueled engine is justified, however, it significantly changes entire combustion process. Especially, intensive research should be undertaken on reducing higher NO<sub>x</sub> emission.

Tutak (2014) investigated the potential of E85 fueling in a diesel engine. Researches were performed using a three-cylinder a direct injection diesel engine. A dual-fueling technology is implemented such that E85 is introduced into the intake manifold using a port-fuel injector while diesel is injected directly into the cylinder. The primary aim of the study was to determine the operating parameters of the engine powered on E85 bioethanol fuel in dual fuel system. The parameters that were accounted for are: engine efficiency, indicated mean effective pressure, heat release rate, combustion duration and ignition delay, combustion phasing and exhaust toxicity. With E85 fuel participation, NO<sub>x</sub> and soot emissions were reduced, whereas CO and HC emissions increased considerably. It was found that E85 participation in a combustible mixture reduced the

excess air factor for the engine and this led to increased emissions of CO and HC, but decreased emissions of nitrogen oxides and soot.

Abu-Qudais et al (2000) investigated and compared the effects of ethanol fumigation and ethanol–diesel fuel blends on the performance and emissions of a single cylinder diesel engine have been. An attempt was made to determine the optimum percentage of ethanol that gives lower emissions and better performance at the same time. This was done by using a simple fumigation technique. The results show that both the fumigation and blends methods have the same behavior in affecting performance and emissions, but the improvement in using the fumigation method was better than when using blends. The optimum percentage for ethanol fumigation is 20%. This percentage produces an increase of 7.5% in brake thermal efficiency, 55% in CO emissions, 36% in HC emissions and reduction of 51% in soot mass concentration. The optimum percentage for ethanol–diesel fuel blends is 15%. This produces an increase of 3.6% in brake thermal efficiency, 43.3% in CO emissions, 34% in HC and a reduction of 32% in soot mass concentration.

Imran et al (2013) identified the potential use of alcohols in fumigation mode on diesel engines. In their review, the effect of ethanol and methanol fumigation on engine performance and emission of diesel engine has been critically analyzed. A variety of fumigation ratios from 5% to 40% have been applied in different types of engines with various types of operational mode. It has been found that the application of alcohol fumigation technique leads to a significant reduction in the more environment concerning emissions of carbon dioxide (CO<sub>2</sub>) up to 7.2%, oxides of nitrogen (NO<sub>x</sub>) up to 20% and particulate matter (PM) up to 57%. However, increase in carbon monoxide (CO) and hydrocarbon (HC) emission have been found after use of alcohol fumigation. Alcohol fumigation also increases the BSFC due to having higher heat of vaporization. Brake thermal efficiency decreases at low engine load and increases at higher engine load.

Liu et al (2014) investigated the combustion and emissions of n-butanol/biodiesel dual-fuel injection on a diesel engine through experiments and simulations. n-Butanol was injected into the intake port, while soybean biodiesel was directly injected into the cylinder. Three different premixed ratios (rp) were investigated, including 80%, 85% and 90%. The injection timings of biodiesel were adjusted to keep the 50% burn point (CA50) between 2° CA and 10° CA after top dead center for achieving stable operation. The EGR (exhaust gas recirculation) rates were changed from 35% to 45%. Results demonstrate that the same CA50 can be achieved by the early or late-injection of biodiesel. For both early- and late-injection, the auto-ignition is triggered by the biodiesel reaction. Increasing premixed ratios can retard the combustion phasing and reduce the pressure rise rate, while the indicated thermal efficiency (ITE) reduces by about 0.6% as increasing rp to 90%. The early-injection has lower NO<sub>x</sub> emissions compared to the late-injection due to lower combustion temperature. The soot emissions are comparable for both early- and late-injection. With the increase of EGR, the NO<sub>x</sub> and soot emissions decrease, while the HC (hydrocarbons) and CO (carbon monoxide) emissions increase. The ITE reduces by 1–2% as increasing EGR to 45%.

Chen et al (2013) conducted an experimental investigation on a direct injection (DI) diesel engine with exhaust gas recirculation (EGR), coupled with port fuel injection (PFI) of n-butanol. Effects of butanol concentration and EGR rate on combustion, efficiency, and emissions of the tested engine were evaluated, and also compared to a DI mode of diesel–butanol blended fuel. The results show butanol concentration and EGR rate have a coupled impact on combustion process. Under low EGR rate condition, both the peak cylinder pressure and the peak heat release rate increase with increased butanol concentration, but no visible influence was found on the ignition delay. Under high EGR rate condition, however, the peak cylinder pressure and the peak heat

release rate both decrease with increased butanol concentration, accompanied by longer ignition delay and longer combustion duration. As regard to the regulated emissions, HC and CO emissions increase with increased butanol concentration, causing higher indicated specific fuel consumption (ISFC) and lower indicated thermal efficiency (ITE). It is also noted that butanol PFI in combination with EGR can change the trade-off relationship between NO<sub>x</sub> and soot, and simultaneously reduce both into a very low level. Compared with the DI mode of diesel–butanol blended fuel, however, the DI diesel engine with butanol PFI has higher HC and CO emissions and lower ITE. Therefore, future research should be focused on overcoming the identified shortcomings by an improved injection strategy of butanol PFI.

Al-Hasan an Al-Momany (2008) investigated the effect of using iso-butanol and diesel fuel blends. The engine used was a single cylinder four stroke CI engine Type Lister 1-8. The tests were performed at engine speeds from 375 to 625 in intervals of 42 rpm at different loads. The fuel blends were 10, 20, 30 and 40% butanol to diesel by volume. The overall engine performance parameters measured included air-fuel ratio (AFR), exhaust gas temperature, brake power (Bp), brake specific fuel consumption (bsfc) and brake thermal efficiency ( $\eta_{th}$ ). The experimental results show that AFR, exhaust gas temperature, (Bp) and ( $\eta_{th}$ ) decreased and bsfc increased with iso-butanol addition compared to neat diesel fuel. The results indicate that the engine performance parameters were optimal when using up to 30% iso-butanol in fuel blends.

Soloiu and Moncada<sup>A</sup> (2018) studied the direct injection of methyl oleate and PFI of n-butanol in RCCI operation to minimize exhaust emissions in reference to conventional diesel combustion. An experimental common rail engine was operated in RCCI and conventional diesel combustion modes under constant boost and similar combustion phasing. The RCCI strategy used two pulses of direct injections with a fixed first injection at 60° before top dead center and a varied

second injection for smooth combustion. Ringing intensity was reduced by 70% for methyl oleate RCCI compared to diesel conventional diesel combustion. The molecular oxygen from methyl oleate allowed a reduction in soot by 75% and 25% compared to diesel in RCCI and conventional diesel combustion operation, respectively. Compared to conventional diesel combustion, NO<sub>x</sub> and soot decreased for RCCI by several orders of magnitude with both emissions approaching near zero levels at low load. The fuels produced a stable RCCI operation where mechanical efficiency was sustained within 2% for same-load points and the coefficient of variation of indicated mean effective pressure was limited to 2.5%.

Soloiu and Gaubert (2018) investigated low temperature combustion was by introducing an 80% mass fraction of n-butanol in a reactivity controlled compression ignition (RCCI) mode. A 60% mass fraction of n-butanol was port fuel injected (PFI) and the additional 20% was directly injected through a blend of n-butanol (Bu) with Fischer-Tropsch gas to liquid synthetic paraffinic kerosene (GTL) with ULSD as a reference. The blended fuels GTL20-Bu80 and ULSD20-Bu80 reduced cetane for improved combustion phasing control compared to the reference RCCI mode with direct injection of neat ULSD and n-Butanol PFI (ULSD40-Bu60). RCCI strategies delayed ignition and increased peak heat release rates due to prolonged mixing time and reactivity stratification, inducing faster flame speeds. In RCCI mode, the ringing intensity (RI) increased up to 85% higher than in CDC. NO<sub>x</sub> and soot were reduced up to 90% with ULSD40-Bu60 compared to CDC. The butanol blends decreased CO by 25% compared to ULSD RCCI. CO levels overlaid each other for GTL20-Bu80 and ULSD20-Bu80 across loads, suggesting that the butanol was the influencing factor. ULSD and ULSD20-Bu80 RCCI increased mechanical efficiencies compared to CDC by 3–4% across loads. ULSD20-Bu80 had the lowest cetane and displayed the greatest improvement in the overall emissions and efficiencies in RCCI compared to CDC.

It has been found that the application of alcohol fumigation technique leads to a significant reduction in the emissions of carbon dioxide, nitrogen oxides, and particulate matter without a serious reduction in engine performance. However, carbon monoxide and unburned hydrocarbon emissions have been found to increase after use of alcohol fumigation. Alcohol fumigation also increases the BSFC due to having higher heat of vaporization, which leads to a lower indicated thermal efficiency. The literature reviewed suggests that applying alcohol fumigation to an IDI diesel engine will yield positive results.

#### 2.4 n-Butanol

Growing energy demand has created a need to shift from finite fossil fuels to renewable bio-fuels. The ever decreasing worldwide petroleum reserves have led to efforts in the search for alternative energy sources such as nuclear, geothermal, biomass, and others (Al-Hasan and Al-Momany 2008). Butanol blends can be used as a drop-in replacement in blends or as a secondary fuel for dual fuel combustion concepts. Butanol has many advantages over other alcohol based fuels. Butanol has a lower vapor pressure and is less corrosive of components of the fuel system. Butanol can be refined from petroleum or produced by fermentation resulting in bio-butanol. The petroleum based butanol is produced from propylene feedstock (Atsumi 2008). Butanol is used in a variety of industries ranging from paint thinners to an additive in personal hygiene. A new application for bio-butanol has recently emerged as an alternative fuel source to petroleum (Dürre 2008) Bio-butanol can be produced through acetone-butanol-ethanol fermentation from renewable sources like sugar beets, sugar cane, corn, wheat, cassava, switch grass, guayule, bagasse, and straw (Qureshi 2006).



## CHAPTER 3: METHODOLOGY

### 3.1 Overview

The purpose of this study was to investigate the emissions of a single cylinder experimental IDI engine, and to optimize the emissions and efficiency of this engine. The experimental test bed consisted of the Kubota EA330-E3-NB1 engine, EMS 8860 engine management computer, port fuel injection system, dynamometer, Kistler piezoelectric pressure transducers, Fourier transform infrared spectroscopy emissions analysis systems, and National Instruments data acquisition boards. It was crucial to design and develop a system that can be used to obtain repeatable results for different fuels. The electronic fuel injection system was developed with the goal of injecting the low reactivity n-butanol into the intake manifold of the engine as a percentage by mass of the total fuel flow. The methods for the development of the port fuel injection system, engine instrumentation, data collection, and fuel analysis are discussed in this section. To control the injection event of the n-butanol an aftermarket ECU was installed and programmed to provide the optimal injection timing. This also allows for precise control of the mass flow rate of the port fuel injector based on engine speed and load. This is of importance because it allows for the percentage of n-butanol to be adjusted based on its' percentage of the total mass of both fuels. This is of significance because the percentage of the injected alcohol fuel has a direct impact on the overall emissions of the research engine.

### 3.2 Research Implementation

To understand the correlations between the chemical and thermo-physical properties of the test fuel analysis of the reference fuel ULSD#2 and n-butanol was performed. This includes; Cetane number, thermos-gravimetric analysis, differential thermal analysis, and dynamic

viscosity. Next the influence of dual fuel combustion using alcohol with respect to conventional diesel combustion was observed. This includes combustion pressure, ignition delay, heat release, mass fraction burned, maximum volume averaged in cylinder gas temperature, cylinder heat fluxes, and heat transfer. Finally, the characteristics of combustion in terms of emissions, and thermal, mechanical, and overall efficiency were determined.

### 3.3 Fuel Analysis

Determination of a fuels quality was performed. Technical functionality and performance of a fuel are prevalent concerns when determining a fuel's quality. Both the physical and chemical properties influence the ignition and combustion of the fuel, which in turn influences the performance and emissions characteristics. The properties of the fuel will also affect the longevity of the engine and of its critical components. In order to verify the quality of the biofuel, experimental determination of lower heating value, calorific value, stability, and values of dynamic viscosity were performed.

#### *3.3.1 Viscosity*

The viscosity of a fuel can affect its' atomization quality as well as the wear of the injection system. The viscosity of the test fuels was determined using a Brookfield Viscometer DV-II Pro Type. Testing occurred over a temperature gradient of 26-60°C with viscosity values measured in cP. The viscometer measures the torque of a rotating motor attached to a spindle submerged in the fuel sample. Shear stress can be determined based on the torque values and spindle geometry. Dynamic viscosity can be then be derived using the shear stress and shear rate. For this thesis 7 mL of fuel was tested using a SC-18 spindle. Figure 3 below shows the Brookfield Viscometer used in testing.

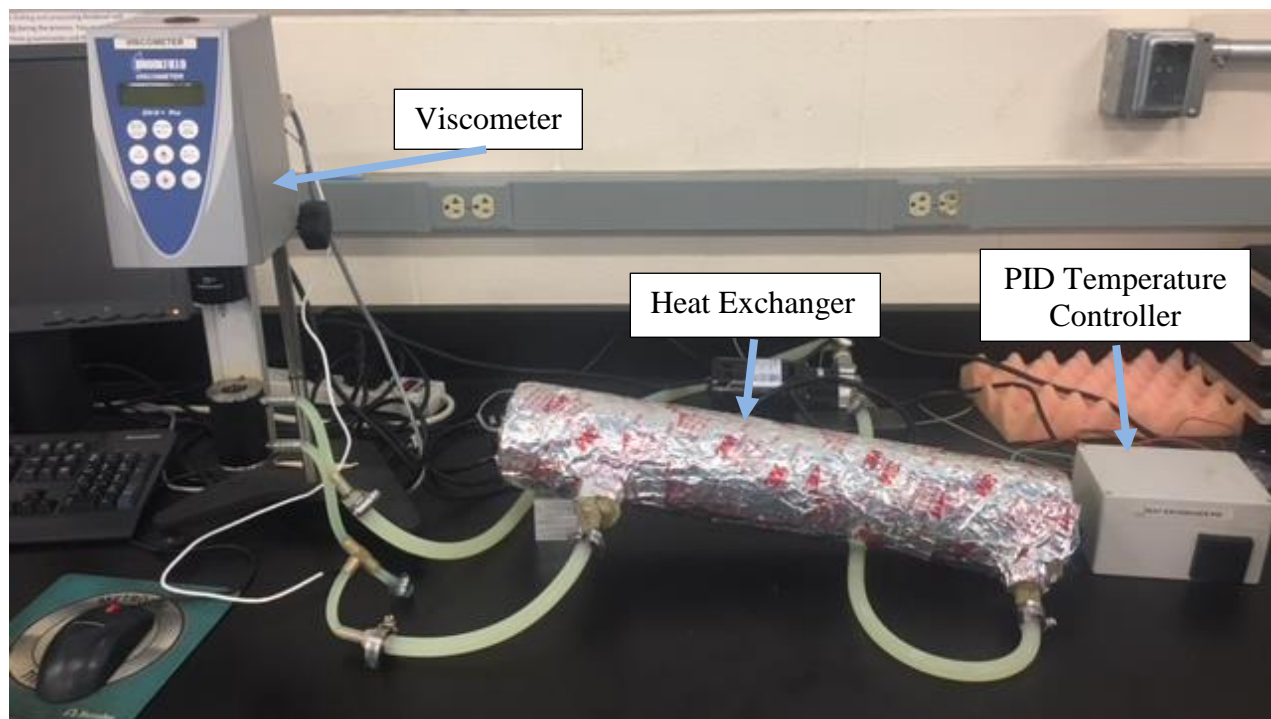


**Figure 3** Brookfield Viscometer and Shell and Tube Heat Exchanger

### 3.3.2 Lower Heating Value

The lower heating value (LHV) of the test fuel and fuel blends was determined using a Parr 6772 Digital Calorimeter. The LHV determines the energy content of the fuel. The sample being studied is placed in a pressurized chamber filled with  $O_2$ . The chamber is submersed completely in distilled and deionized water to thermodynamically isolate the system. A fuse wire inside the calorimeter ignites the sample. A thermocouple is then used to measure the change in water temperature from the heat release. A gross heating value for the process is found. The lower heating value is then derived by subtracting the latent heat of vaporization of water. This is based on the ASTM D240 standard. The constant volume calorimeter can be seen in Figure 4 below.

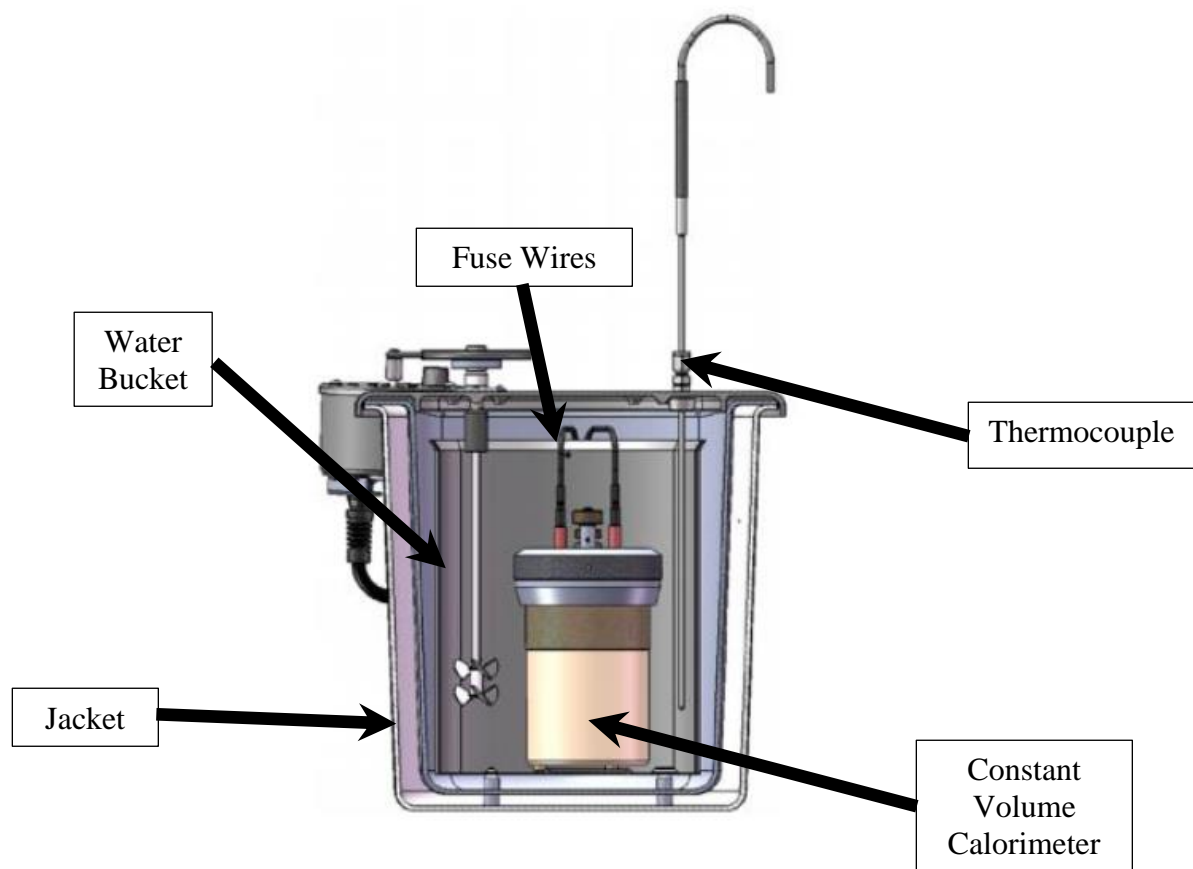


**Figure 4** Parr 6772 Digital Calorimeter (Parr 2014)

### 3.3.3 Thermal Gravimetric and Differential Thermal Analysis

The thermal gravimetric and differential thermal analysis was determined using a DTG-60 from Shimadzu. Data was recorded using the TA-60WS thermal analysis workstation. Thermal gravimetric analysis shows how a sample burns and the mass changes over a temperature gradient 0°C-600°C. This gives insight to the volatility of the fuel being tested. The differential thermal analysis shows how the sample of test fuel will absorb and release energy over the same temperature gradient. Tests were conducted at a constant temperature rise rate of 20 °C/min and a constant flow rate of oxygen at 5 mL/min. This is done to simulate the environment of an IC engine. The DTG-60 apparatus can be seen in Figure 5 below.

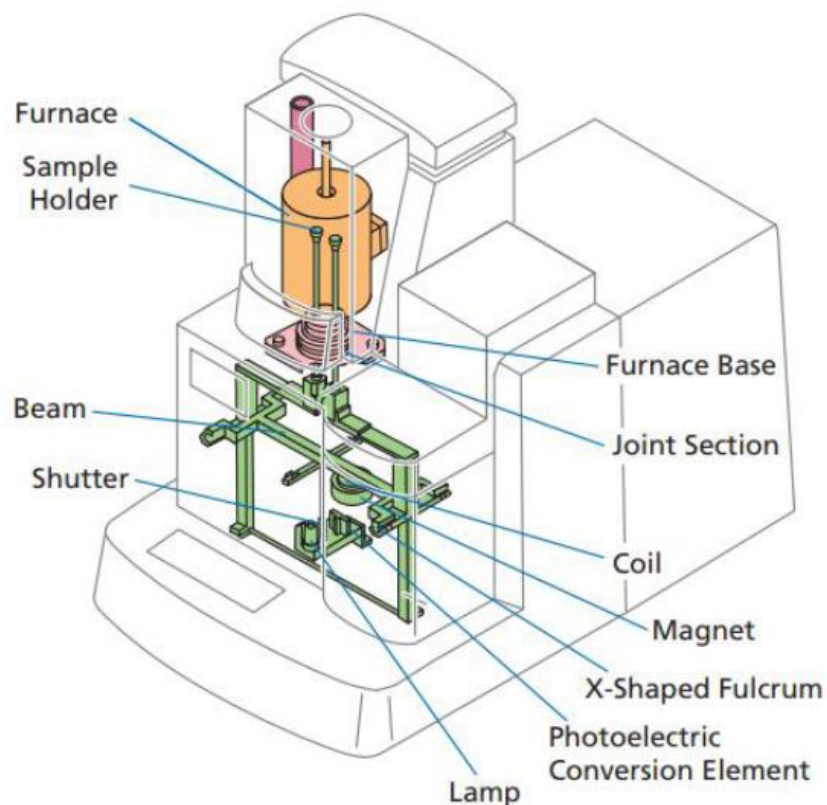


**Figure 5** Shimadzu DTG-60 TGA-DTA (Shimadzu Corporation 2012)

### 3.3.4 He-Ne Mie Scattering

The droplet size, Sauter Mean Diameter ( $\mu\text{m}$ ) with respect to time and the volume frequency distribution (%) of the fuel spray was analyzed with a Malvern Spraytec Mie scattering He-Ne laser. A reduction in the Sauter Mean Diameter of a fuel's spray creates a larger surface to volume ratio, which increases combustion efficiency and reduces ignition delay. The test setup of the experimental apparatus is displayed in Figure 6. Calculations are performed by measuring the light scattered by the spherical particles injected through the laser (Malvern 2006). The test setup places the injector 14 cm from the center of the laser beam with an injection pressure of 80 bar. Data collection began 0.1 ms after initiating the spray and stopped at 2 ms. The sampling rate was

set to 10 kHz for 3 ms. The Helium-Neon laser is 10 mm diameter with a wavelength of 632.8 nm.

The SMD determination is based on the British Standard BS2955:1993.

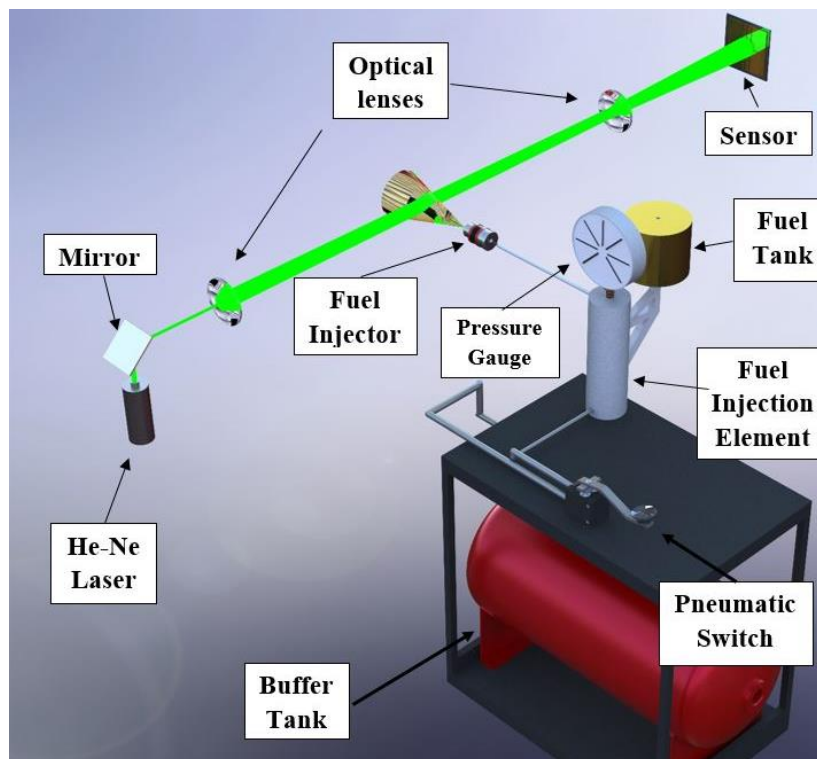


**Figure 6** Malvern Spraytec Mie Scattering He-Ne Laser in the Engine Laboratory

### 3.3.5 Constant Volume Combustion Chamber

The Derived Cetane Number (DCN) is calculated based on testing in accordance with ATSM Standard D7668-14a for the determination of derived cetane number (DCN) of diesel fuel oil-ignition delay and combustion delay using a constant volume combustion chamber (CVCC) (ASTM 2014). The CVCC, shown in Figure 7, utilizes a fuel sample as low as 60 mL to determine the DCN, Ignition Delay (ID), Combustion Delay (CD), Negative Temperature Coefficient Region (NTC), and Low Temperature Heat Release (LTHR). For this study, a PAC CID510 constant volume combustion chamber was used. Low temperature heat release is a low magnitude natural luminosity associated with the injection of fuel. LTHR encompasses the NTC region where the

thermal characteristics of a fuel cause the fuel to ignite for a small amount of time until a ‘cool flame’ reduces the energy output of the reaction until high temperature heat release (HTHR).

A constant volume combustion chamber is a useful tool to observe LTHR through conventional combustion analysis (Szybist 2007). For this study, a PAC CID510 constant volume combustion chamber was used to observe and compare the LTHR behavior of ULSD#2 and n-butanol.

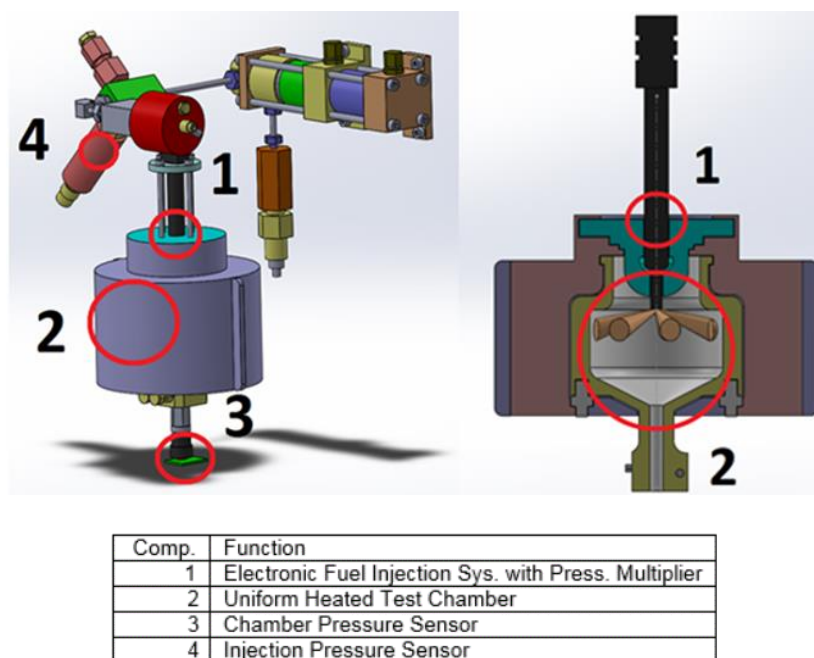


**Figure 7** PAC ID510 Combustion Chamber

### 3.4 Engine Operating Procedures

The purpose of this investigation was to demonstrate the dual fuel combustion capability of an IDI engine using ULSD#2 and n-butanol. The basis of data acquisition was centered on the pressure from combustion and the crank angle. A schematic of the experimental engine is presented in Figure 8 and Figure 9 below. In general, the auxiliary chambers are designed to produce high temperatures and high velocity swirl, which causes the fuel and air to mix well before

ignition. This will cause the fuel blends to exhibit very similar combustion characteristics with almost identical ignition delay in spite of variations in fuel properties. Load was applied to the engine from a dynamometer and testing was commenced at increasing loads over increasing concentrations of n-butanol by mass. Continuous testing was performed and the engine was allowed to run for a 2 minute transition period before switching to a different concentration of n-butanol. Measurements were taken at a constant engine load of 5.5 bar indicated mean effective pressure and a constant speed of 2400 rpm. The concentration of n-butanol was varied from 10% to 40% by mass of the total fuel flow rate. Injection timing was fixed at 24 CAD BTDC for the main injector and at TDC twice per cycle for the port fuel injector. A total of 100 engine cycles were averaged for each research point.

### 3.5 Experimental Engine Setup

The engine used in this research was an indirect injection, single cylinder Kubota EA330-E3-NB1. The engine is liquid cooled, naturally aspirated, uses compression ignition, and has 2 valves per cylinder. The engine contains a three vortex separate combustion chamber with no exhaust gas recirculation and no turbo or supercharging. The engine is limited to 3000RPM, and is capable of producing 6 HP of continuous power. The injection system was a plunger type pump with a  $1 \times 0.200$ mm pintle tip needle injector. In cylinder pressure was obtained using a Kistler 6053cc non-cooled piezoelectric pressure transducer and the fuel line pressure was measured using a Kistler 6229 inline injection pressure sensor with a Kistler 6533A11 clamp adaptor. An Omron 2000 pulse/rev rotary encoder gave a time line for the engine. Data was obtained using a high speed Yokogawa DL750 data acquisition system (DAQ) that is capable of 1 MS/s. Torque was measured with an Omega TQ513 torque cell. The mass flow rate of air was measured with a Merriam Z50MC2-2 laminar flow meter equipped with a probe that automatically adjusts air



density for test cell ambient conditions. The emissions data was gathered from an AVL 415S Smoke Meter, Horiba MEXA-720NO<sub>x</sub> analyzer, and a MKS Multigas 2030 FTIR.

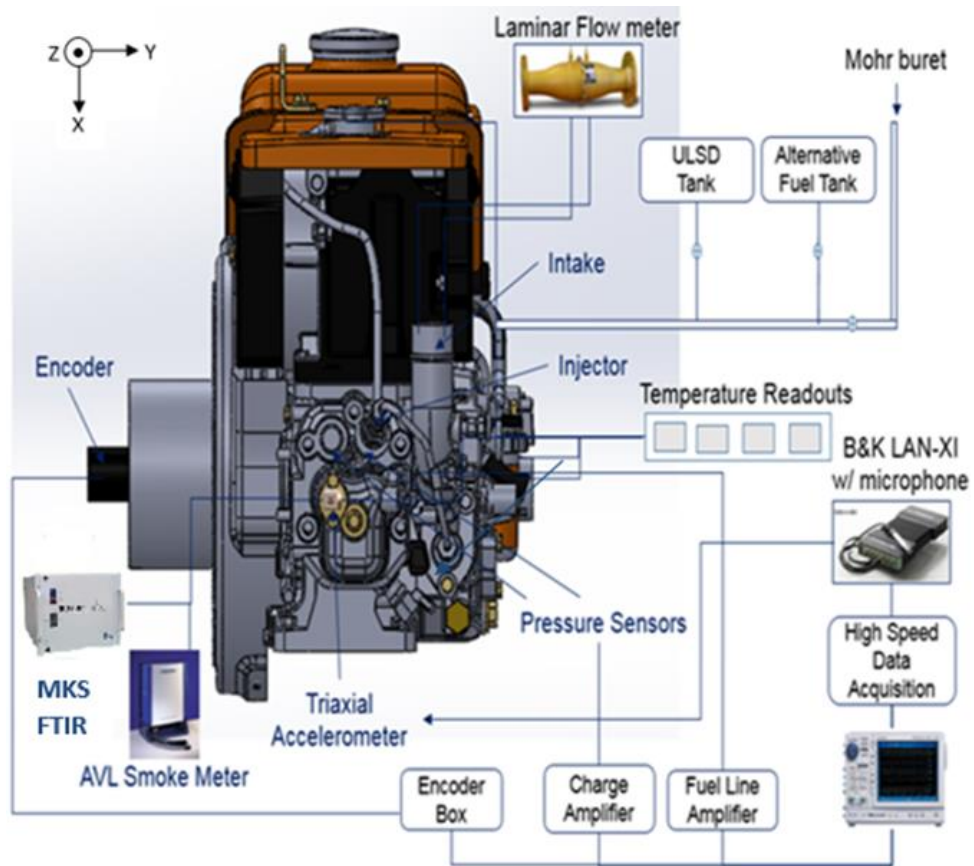


**Figure 8** Experimental Engine Schematic (Kubota Tractor Corporation)

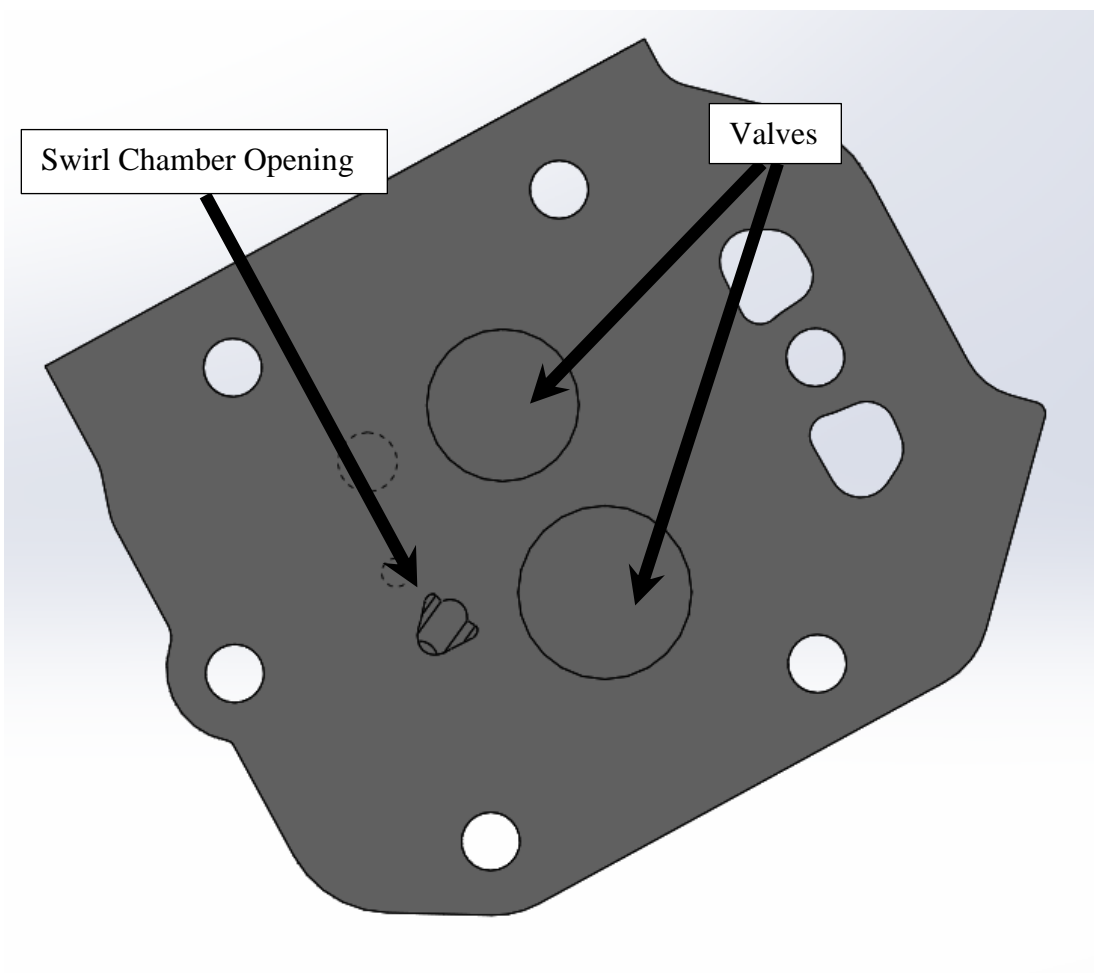
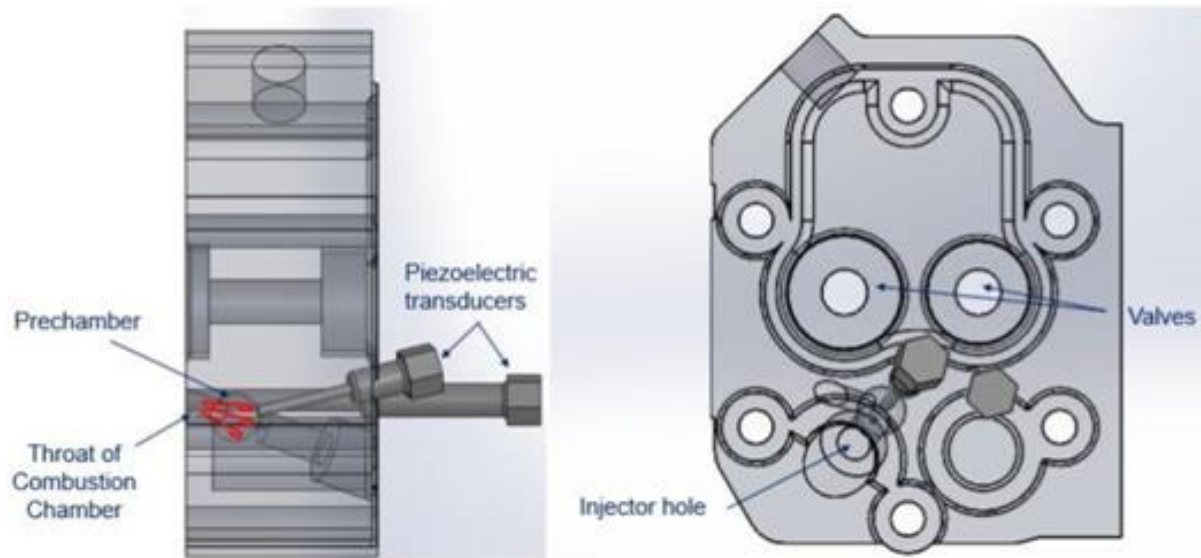


**Figure 9** Triple Vortex Combustion Chamber

**Table II:** Kubota Engine Specifications (Kubota 2014)

<b>Model</b>		<b>EA330-E3-NB1</b>
<b>Emission Regulation</b>		Tier 4
<b>Type</b>		Horizontal 4-cycle liquid cooled Diesel
<b>Number of Cylinders</b>		1
<b>Bore</b>	mm (in)	77 (3.03)
<b>Stroke</b>	mm (in)	70 (2.76)
<b>Displacement</b>	L (cu.in)	0.325 (19.83)
<b>Combustion System</b>		IDI (TVCS)
<b>Aspiration</b>		Naturally Aspirated
<b>Maximum Speed</b>	rpm	3000
<b>Output: Net Intermittent</b>	kW	5.15
	HP	6.9
	PS	7.0
<b>Oil Pan Capacity</b>	L (gal)	1.3 (0.34)
<b>Starter Capacity</b>	V-kW	12-0.8
<b>Alternator Capacity</b>	V-A	12-3.5
<b>Length</b>	mm (in)	566 (22.28)
<b>Width</b>	mm (in)	411 (16.18)
<b>Height (1)</b>	mm (in)	457 (17.99)
<b>Dry Weight</b>	kg (lb)	54 (119)

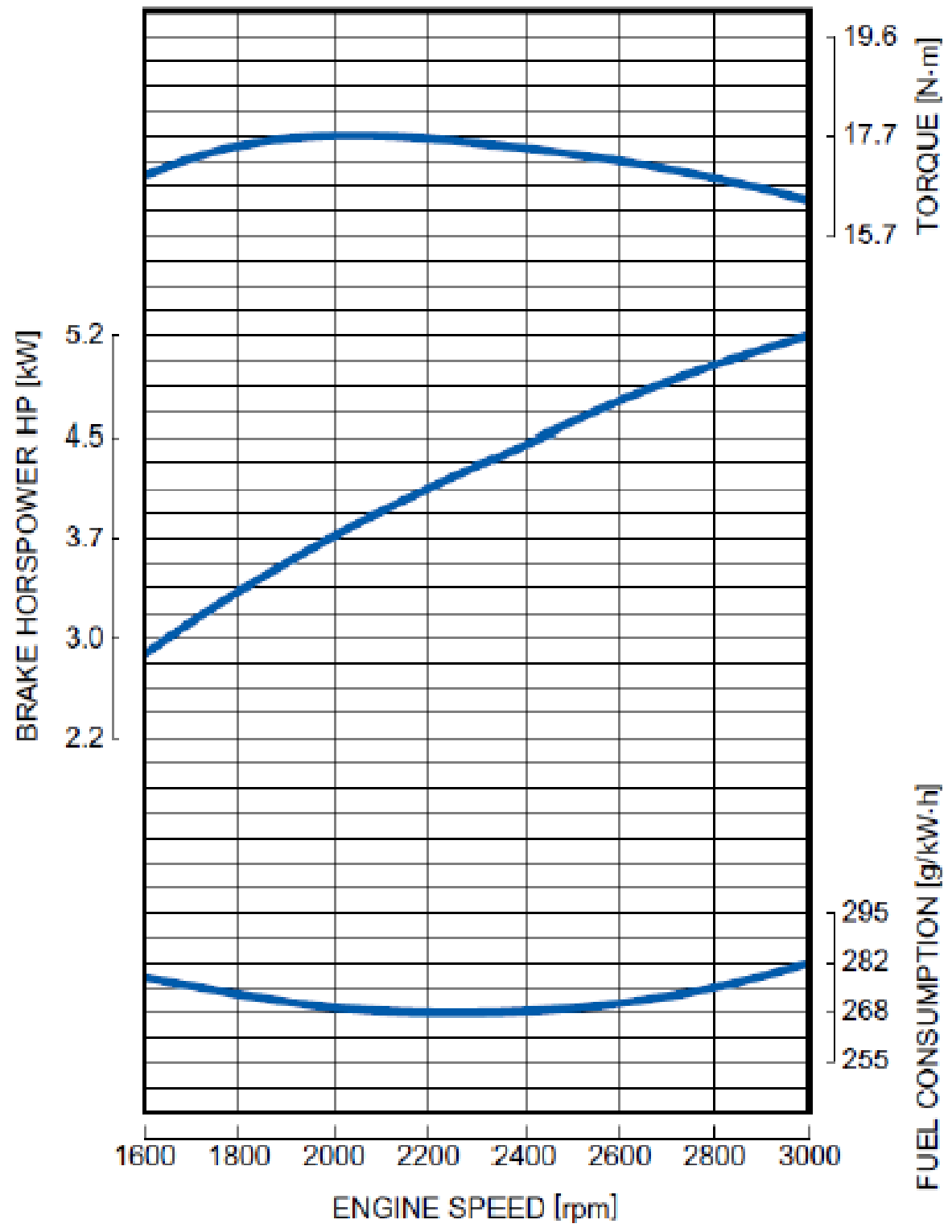
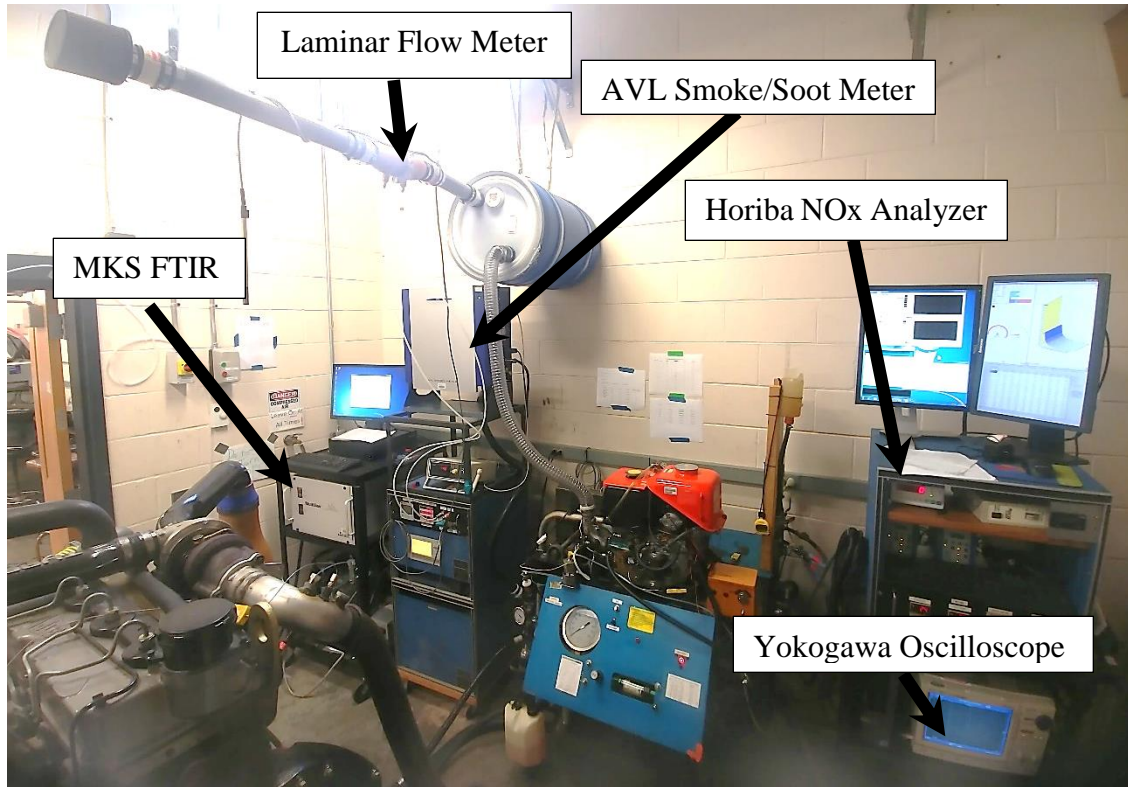


Figure 10 Fuel Consumption, Power, and Torque vs. Engine Speed (Kubota 2014)



**Figure 11** Test Cell Setup

### 3.5.1 Pressure Transducers

In-cylinder pressure is obtained using two piezoelectric pressure sensors introduced to the combustion chamber via a specially manufactured sleeve for the main chamber and a glow plug adapter for the swirl chamber. These sensors combined with the rotary shaft encoder is used to obtain the combustion pressures during the engine cycle. A Kistler Type 6053CC was mounted in the main combustion chamber.

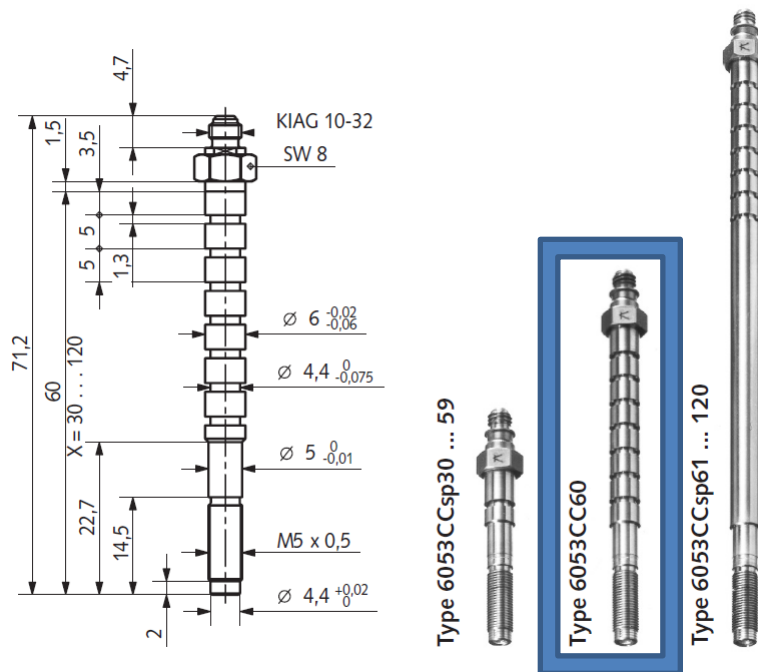


**Figure 12** Kistler Main Chamber Transducer (Kistler 2011)

The pressure sensor used for the swirl chamber was a Kistler 6056A piezoelectric pressure transducer, Figure 13. This sensor is housed in a glow plug fitting, Figure 14, which enables the sensor to be in direct contact with the in-cylinder gases during combustion.

**Table III:** Kistler Type 6056A Specifications

Measuring range	bar	0 – 250	Sensitivity change 23 – 350 °C	%	$\leq \pm 2$
Calibrated sub-ranges	bar	0 – 50, 0 – 100, 0 – 150, 0 - 250	Thermal shock error	bar	$\leq \pm 0.5$
Overload	bar	300	$\Delta p_{\text{MIN}}$	%	$\leq \pm 2$
Sensitivity	pC/bar	$\approx -20$	$\Delta p_{\text{MAX}}$	%	$\leq \pm 1$
Natural frequency, nominal	kHz	$\approx 160$	Insulation resistance at 23 °C	$\Omega$	$< 10^{13}$
Linearity at 23 °C	%FSO	$\leq \pm 0.03$	Shock resistance	g	2000
Acceleration sensitivity	bar/g	$< 0.0002$ $< 0.0005$	Tightening torque	Nm	1.5
Operating temperature range	°C	- 20 – 360	Weight	g	10
Connector	°C	200	Connector (PTFE)	-	KIAG 10-32

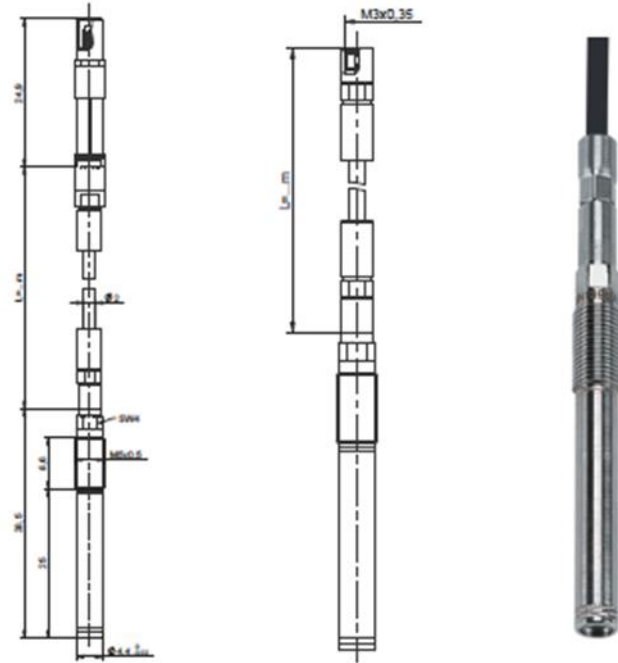


**Figure 13** Kistler Swirl Chamber Transducer (Kistler 2017)



**Table IV: Kistler Type 6053CC Specifications**

<b>Range</b>	bar	0 – 250
<b>Calibrated ranges</b>	bar	0 – 50, 0 – 100, 0 – 150, 0 – 250
<b>Overload</b>	bar	300
<b>Sensitivity</b>	pC/bar	-20
<b>Natural frequency</b>	kHz	≈ 160
<b>Linearity</b>	%FSO	≤ ± 0.03
<b>Acceleration sensitivity</b>	bar/g	< 0.0005
<b>Shock resistance</b>	g	2,000
<b>Thermal shock error <math>\Delta p</math></b>	bar	≤ ± 0.7
<b>Operating temperature range</b>	°C	-20 - 350
<b>Capacitance</b>	pF	5
<b>Insulation resistance at 23 °C</b>	TΩ	≥ 10 <sup>13</sup>
<b>Tightening torque</b>	Nm	1.5
<b>Weight</b>	g	30
<b>Connector</b>	-	M3X0.35

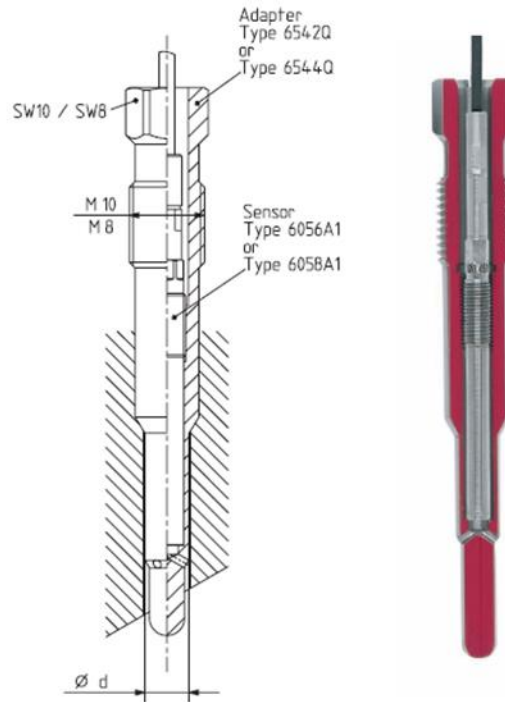


**Figure 14** Kistler Glow Plug Adapter (Kistler 2013)

The pressure transducers are housed in a stainless steel case with coaxial cables on one end and stainless steel diaphragms on the other. The diaphragm covers a cavity that houses the piezoelectric crystal sensing element. The cylinder pressures act on the piezoelectric crystal in the Kistler sensor resulting in an output charge that is proportional to the measured pressures. The signal from the pressure sensors was conditioned and amplified by a Kistler 5010B dual charge amplifier.

A clamp style pressure transducer has been installed to measure fuel pressure. A Kistler 6229 inline injection pressure sensor with a Kistler 6533A11 clamp adapter were chosen for the application. The type 6229 is capable of making high pressure measurements within the fuel pump or through the fuel lines up to 500 bar.



**Figure 15** Kistler Type 6229A Fuel Line Pressure Transducer (Kistler 1997)

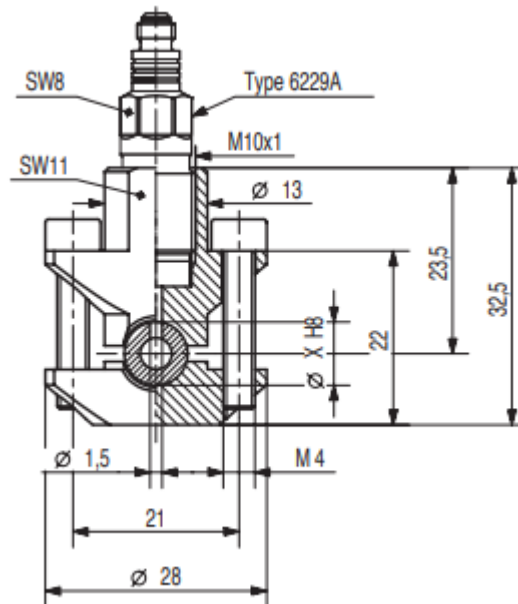


**Figure 16** Kistler Clamp on Adapter (Kistler 1997)

**Table V: Kistler Type 6229A Transducer Specifications**

<b>Range</b>	bar	0 – 5000
<b>Calibrated partial range</b>	bar	0 – 500
<b>Overload</b>	bar	6000
<b>Sensitivity</b>	pC/bar	-2.5
<b>Natural frequency</b>	kHz	>200
<b>Rise time</b>	μs	1
<b>Linearity</b>	%FSO	≤ ± 1
<b>Acceleration sensitivity</b> axial and transverse	bar/g	< 0.004 < 0.01
<b>Shock resistance</b> axial and transverse	g	10,000 5,000
<b>Temperature coefficient of sensitivity</b>	% /°C	+ 0.02
<b>Operating temperature range</b>	°C	-50 - 200
<b>Capacitance</b>	pF	≈ 8
<b>Insulation resistance</b>	TΩ	50
<b>Tightening torque</b>	Nm	20
<b>Weight</b>	g	12
<b>Service life</b>	number of cycles from 0-3000 bar	> 10 <sup>7</sup>

### 3.5.2 Charge Amplifier

The Kistler Dual Mode Amplifier is an amplifier used for signal conditioning of various types of transducers. In the case of this research, the amplifier was used in the charge amplifier mode required for high impedance piezoelectric pressure transducers such as the Kistler 6053CC used in the experimental setup. Figure 17 is a depiction of the Kistler 5010B Dual Mode Charge Amplifier used for in-cylinder pressure signal conditioning.



**Figure 17** Kistler 5010B Dual Mode Charge Amplifier (Kistler 2010)

The amplifier converts the charge from the pressure transducer into a usable 0-10V output. The conversion is based on the sensitivity of the transducer, obtained from transducer calibration certificate, and the measurement scale. The measurement scale used by the amplifier is in Measuring Units per Volt (MU/V), and the transducer sensitivity is in pC/MU. The unit MU is used on the amplifier because it is not specific to the pressure transducer. The amplifier can be used with sensors that measure force, strain, acceleration, and other parameters requiring

piezoelectric transducers. Technical data for the Kistler 5010B amplifier can be found in Table VI.

**Table VI:** Technical Data for Kistler 5010B Amplifier (Kistler 2010)

Specifications	Unit	Type 5010B	Time Constant	Unit	Type 5010B
Measurement range	pC	$\pm 10$ - 999000	Long	sec	0 - 100000
Scale settings 1,2,3,4,5 sequence	MU/V	0.0002 - 10000000	Medium	sec	1 - 10000
Sensor sensitivity	pC/MUmv /MU	0.01 -9990	Short	sec	0.01 - 100
<b>Input</b>			<b>Time constant resistor</b>		
Connector charge, voltage		BNC neg.	Long	$\Omega$	$>10^{14}$
Impedance charge mode	$\Omega$	70	Medium	$\Omega$	$10^{11}$
Impedance voltage mode	$\Omega$	100K	Short	$\Omega$	$10^9$
Voltage max.	V	50	<b>Noise</b>		
Insulation resistance at input	$\Omega$	$10^{14}$	Reffered to with input shield	pCrms	0.0035
Sensor power voltage mode	mA	4	1 pC/V max	$\mu$ Vrms	500
Frequency response	Hz	180000	Drift MOSFET leakage current	pC/s	$\leq \pm 0.03$
Accuracy	%	$\leq \pm 0.050$	Zero offset	mV	0.50

### 3.5.3 Rotary Encoder

In order to measure the angular location of the engine a rotary encoder was implemented. The rotary encoder chosen for the experimental setup was the Omron E6C2-CWZ3E incremental rotary encoder pictured in Figure 18. The rotary encoder was mounted on a plate behind the engine and connected, via a flex coupling, directly to the engine's flywheel. This allowed for the direct measurement of the angular displacement in respect to engine's TDC position with a 1:1 ratio.



**Figure 18** Omron E6C2 Rotary Encoder (Omron 2015)

The rotary encoder is a 2000 pulse per revolution (ppr) optical encoder that features 3 channels (A,B, and Z). Channels A and B output 2000 ppr while channel Z outputs a homing 1 ppr. The Z encoder was mounted and aligned in such a way that the Z channel pulse lined up with the engine TDC. This allowed for the Z channel to sync the 2000 ppr signals in respect with TDC. For the experimental setup channel B was not used. This is because the engine always rotates in a counter-clockwise direction facing the flywheel, and the encoder's capability of determining rotational direction was unnecessary.

#### *3.5.4 Temperature*

Monitoring operational temperatures of the test engine is important in maintaining repeatability throughout the experiment. Drastic changes in operating temperatures will have a direct effect on emissions and performance results. The test engine was instrumented with K- Type thermocouples for measurements of exhaust gas temperature, engine oil temperature, cooling water temperature, and dyno oil temperature.

Omron E5CS temperature controllers were paired with K-Type thermocouples. The Omron E5CS series controller has the capability to display the temperature from a K-Type thermocouple to  $\pm 0.3\%$  accuracy. Fig. 20 is a depiction of the E5CS series of thermocouple controllers and the 1/16DIN size pictured on the left was used in the experimental setup.



**Figure 19** Omron E5CS Thermocouple Controllers (Omron 2015)

The K-Type thermocouple was chosen for its versatility, robustness, and ability to accurately measure the temperatures encountered by an engine. The K-Type thermocouples have a temperature range of  $-200^{\circ}\text{C}$  to  $1250^{\circ}\text{C}$  which is higher than the maximum observed exhaust temperatures by a magnitude of 4.

### *3.5.5 Flow Meters*

The Meriam Laminar Flow Element from the 50MC2 series was used to monitor the incoming air charge. The meter is paired with an integral flow computer that adjusts for test cell pressure, static pressure, temperature and relative humidity to provide the most accurate results possible. Calibration data for up to five meters can be stored in memory and recalled allowing for



quick transitions between experimental engines. Measurements are based on the differential pressure principle.



**Figure 20** Meriam 50MC2 Series Laminar Flowmeter and Integral Flow Computer (Meriam 2018)

Fuel mass flow rates for the port fuel injector were observed using a P001 piston flow meter from Max Machinery. The fuel flow meters are designed with variable output transmitters for optimal resolution and, anti-dithering, and signal dampening. The flow meter is capable of low flow measurement from 0.005 to 200 cc/min (0 to 0.053 gpm).



**Figure 21** Max Machinery P001 Piston Flow Meter (Max Machinery 2017)

Data for the piston flow meter was observed in real time using an Arduino Mega2560 microcontroller. An original sketch was written to convert the analog input reading of the microcontroller which is observed as a number from 0 – 1023 to a voltage. The voltage value was then converted to a mass flow rate in kg/hr based on a linear curve fit acquired from the injector calibration. A preset number of data values were stored to the mega and averaged. The average value was then displayed on a desktop computer within the test cell. Averages were updated every 100 microseconds.

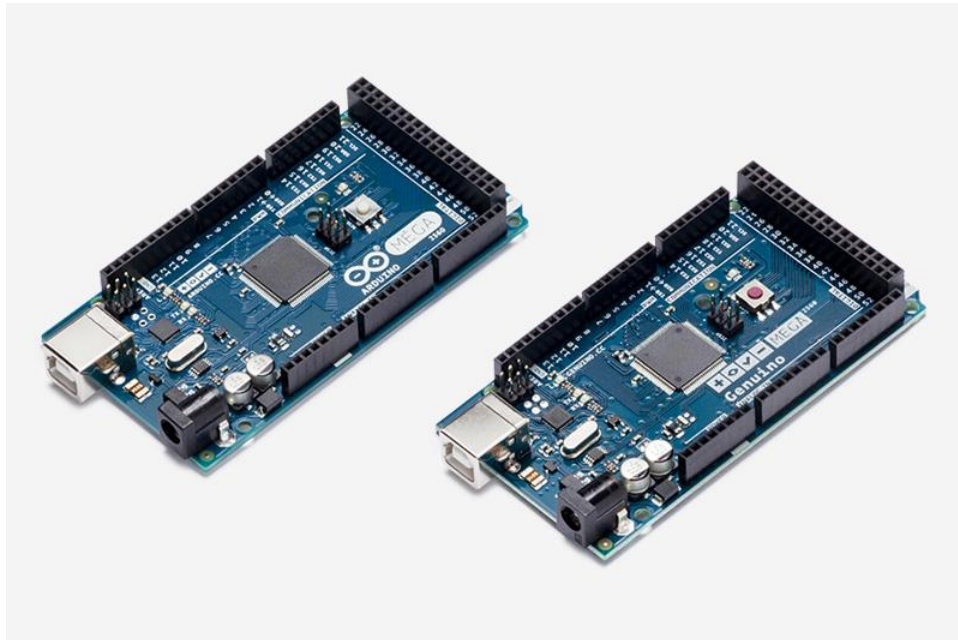
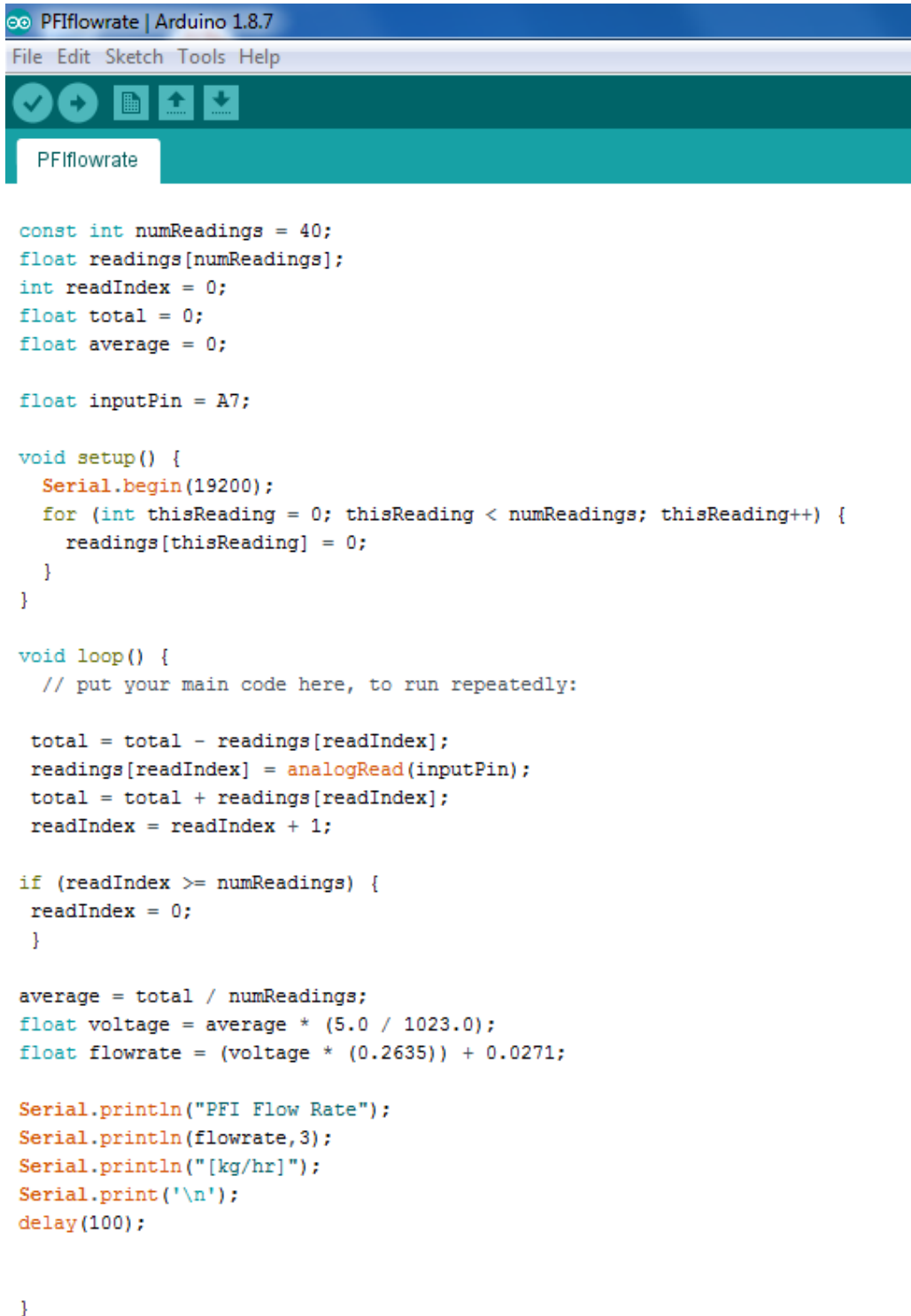


**Figure 22** Arduino Mega2560 Microcontroller (Arduino 2018)



```

Arduino IDE - PFiflowrate | Arduino 1.8.7
File Edit Sketch Tools Help
[Icons: Checkmark, Arrow, Grid, Upload, Download]
PFiflowrate

const int numReadings = 40;
float readings[numReadings];
int readIndex = 0;
float total = 0;
float average = 0;

float inputPin = A7;

void setup() {
  Serial.begin(19200);
  for (int thisReading = 0; thisReading < numReadings; thisReading++) {
    readings[thisReading] = 0;
  }
}

void loop() {
  // put your main code here, to run repeatedly:

  total = total - readings[readIndex];
  readings[readIndex] = analogRead(inputPin);
  total = total + readings[readIndex];
  readIndex = readIndex + 1;

  if (readIndex >= numReadings) {
    readIndex = 0;
  }

  average = total / numReadings;
  float voltage = average * (5.0 / 1023.0);
  float flowrate = (voltage * (0.2635)) + 0.0271;

  Serial.println("PFI Flow Rate");
  Serial.println(flowrate, 3);
  Serial.println("[kg/hr]");
  Serial.print('\n');
  delay(100);
}

```

**Figure 23** Arduino Mass Flow Rate Sketch

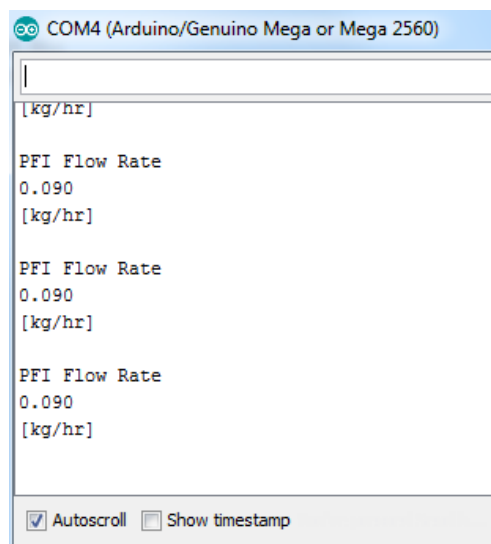


**Figure 24** Arduino Serial Monitor Displaying Flow Rate Measurements

### 3.5.6 Emissions Analyzers

Emissions species from the experiments, were observed using Fourier-transform infrared spectroscopy. The MultiGas 2030 from MKS was used. The instrument is capable of measuring with a sensitivity of 10 – 100 parts per billion. Up to 30 different species can be monitored simultaneously at a 1Hz sampling rate.

**Table VII:** MKS Main Measured Species and Calibration Ranges

Nitrogen Monoxide (NO) 0 -3000 ppm	Carbon Monoxide (CO) 0 – 500 ppm	Ethane (C <sub>2</sub> H <sub>6</sub> ) 0 - 1000
Nitrogen Dioxide (NO <sub>2</sub> ) 0 -2000 ppm	Carbon Dioxide (CO <sub>2</sub> ) 0 – 20 %	Ethylene (C <sub>2</sub> H <sub>4</sub> ) 0 – 3000 ppm
Acetylene (C <sub>2</sub> H <sub>2</sub> ) 0 – 1000 ppm	Isocyanic Acid (HNCO) 0 – 400 ppm	Ammonia (NH <sub>3</sub> ) 0 – 3000 ppm
Methanol (MeOH) 0 – 1000 ppm	Formic Acid (HCOOH) 0 – 100 ppm	Propylene (C <sub>3</sub> H <sub>6</sub> ) 0 – 1000 ppm
Methane (CH <sub>4</sub> ) 0 – 3000 ppm	Nitrous Oxide (N <sub>2</sub> O) 0 – 1040 ppm	Formaldehyde (HCHO) 0 – 500 ppm
Water (H <sub>2</sub> O) 0 – 25 %	Nitrous Acid (HNO <sub>2</sub> ) 0 – 20 ppm	Sulfur Dioxide (SO <sub>2</sub> ) 0 – 300 ppm
Ethanol (C <sub>2</sub> H <sub>6</sub> O) 0 – 10000 ppm	Hydrogen Cyanide (HCN) 0 – 100 ppm	Benzene (C <sub>6</sub> H <sub>6</sub> ) 0 – 1000 ppm



**Figure 25** MKS MultiGas 2030 FTIR (MKS 2017)

The instrument passes an infrared beam through the gas sample. The sample absorbs spectral frequencies from the beam. The absorbed frequencies and their intensities are dependent on the atoms associated with the chemical bond and the strength of those bonds. The absorption spectrum is unique for each gas and can be used to identify and quantify emissions. The instrument is also equipped with a flame ionization detector (FID). Ions can be formed from the combustion of organic compounds in a hydrogen flame. The formation of ions is proportional to the concentration of the organic compound in the sampled gases. The FID can measure the quantity of ions formed. They are primarily used for measuring hydrocarbon content of the exhaust gases.



**Figure 26** AVL 415s Smoke/Soot Meter (AVL 2011)

The AVL 415s Smoke Meter was used to measure soot emissions. It uses the filter paper method in accordance with ISO 10054 to measure filter smoke number, soot concentration, and percent pollution. The instrument measures over a range from 0 to 10 FSN. The minimum detection limit is 0.002 FSN and 0.02 mg/m<sup>3</sup> for soot. The resolution of the instrument is 0.001 FSN and 0.01 mg/m<sup>3</sup>. The smoke meter operates by passing a volume of exhaust gas through clean filter paper. The blackening of the paper due to soot is then detected by an optical reflectometer head.

### 3.6 Port Fuel Injection System Design

The port fuel injection (PFI) fabrication and installation was an integral part of achieving full control of fuel delivery to the engine. The PFI system allowed for precise fuel mass flow rates to be achieved during changing operational conditions. Developing the system composed of manufacturing components specific to the test engine. The required components for the system are listed in Table VIII. The flow path of the system can be seen in Figure 27.

**Table VIII:** Port Fuel Injection System Components

<b>1</b>	Engine Control Unit (ECU) – EMS8860
<b>2</b>	In-port electronic fuel injector – PL2-155
<b>3</b>	Potentiometer
<b>4</b>	Variable Reluctance Crank Sensor
<b>5</b>	12V Battery
<b>6</b>	64 Tooth Ferrous Trigger Wheel
<b>7</b>	Hose fittings
<b>8</b>	High Pressure SAE 30R9 Fuel Line
<b>9</b>	High Pressure Fuel Injection Pump (100psi) +
<b>10</b>	42psi Fuel Pressure Regulator
<b>11</b>	Fuel Tank
<b>12</b>	Fuel Filter
<b>13</b>	Mounting Bracket
<b>14</b>	Power Switch
<b>15</b>	Intake Manifold
<b>16</b>	Fuel Flow Meter

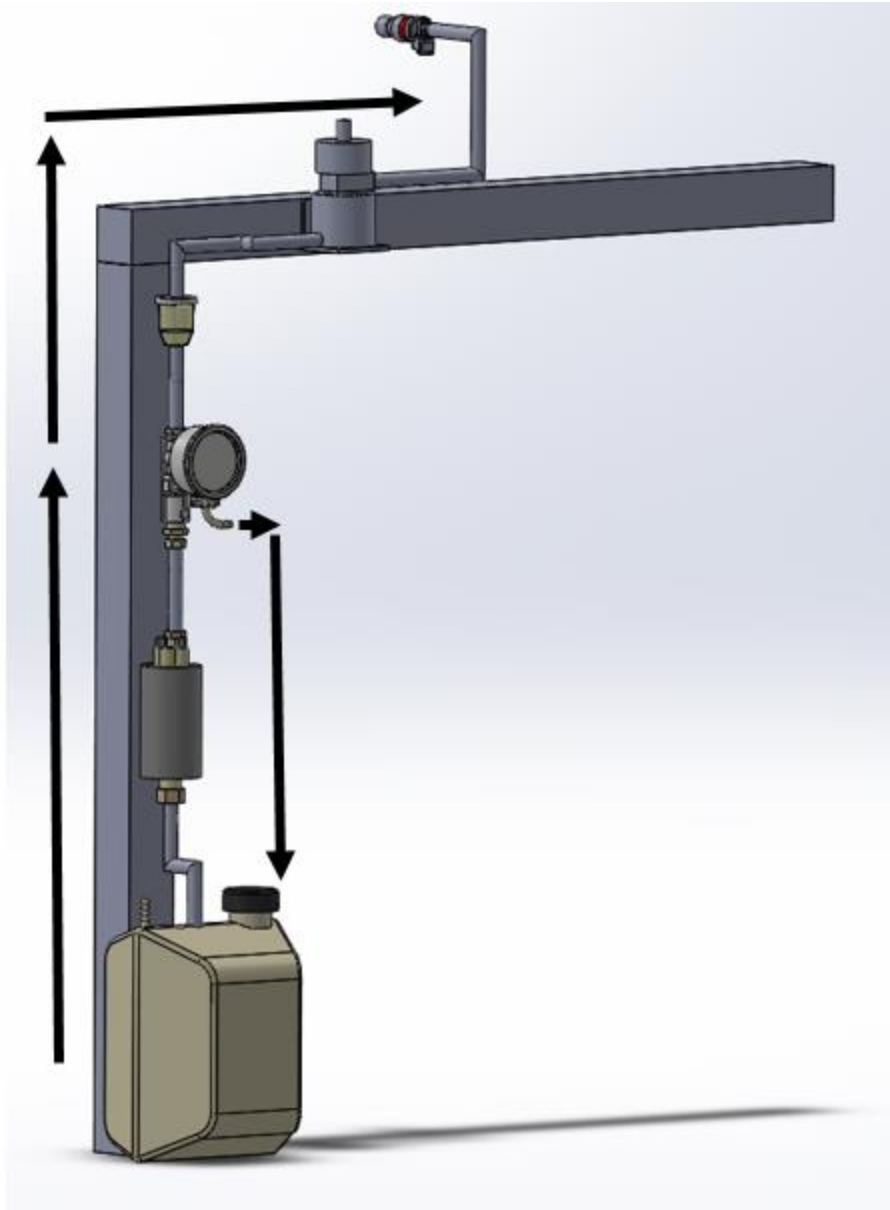


**Figure 27** Port Fuel Injection System Schematic

### *3.6.1 Intake Manifold Design*

A preliminary computational fluid dynamics analysis was performed using Fluent in ANSYS Workbench version 17.1. This was done to provide a baseline for comparison and to understand the flow behavior in the intake. Understanding the fluid motion helps to prevent poor mixing due to wall wetting. To simplify computations the working fluid was



assumed to be incompressible so a pressure based solver was used. The working fluid for the baseline simulation was air and was assumed to be an ideal gas. The simulation with port fuel injection used air and n-butanol as working fluids. Both were predefined by ANSYS. Properties for the working fluid were assumed constant and were evaluated at standard atmospheric temperature and pressure.

The computational domain being modeled was the intake runner from the inlet to the mating surface at the cylinder head. The velocity gradient close to the wall was of great interest, especially the effects that the port fuel injector will have on the flow characteristics. Due to this a mesh with a fine relevance was used. Advanced meshing controls were manually selected. Proximity and curvature were used for the advanced sizing function. Inflation was used at the inlet and outlets to capture the boundary layer behavior. The inflation was program controlled. The transition control was left on the default setting of slow to allow for a smooth transitions. Tetrahedral cells were used to more accurately capture the complex, curved geometry of the injector nozzle. Patch conforming was selected for a high quality mesh and because of the features' compatibility with inflation.

The geometry is divided into five zones. Boundary conditions were set for the inlet, pfi inlet, and outlet zones. Boundary conditions were considered for pressure and temperature, and heat flux. Heat flux was assumed to be zero for all zones. Boundary conditions were taken from experimental data with the exception of the temperature at the inlet which was assumed to be room temperature.

**Table IX: Boundary Conditions**

Zone	Pressure	Temperature
<b>inlet</b>	1.01325 bar	300 °K
<b>pfi inlet</b>	2.75790 bar	300 °K
<b>outlet</b>	0.80000 bar	570 °K

For flows involving heat transfer or compressible flow, the energy equation must be enabled (4).

An Eulerian approach was chosen for particle tracking. Fluent solves three transport equations: continuity (5), momentum (6 & 7).

$$\frac{\partial}{\partial t}(\rho E) + \nabla \cdot (\vec{v}(\rho E + p)) = \nabla \cdot (k_{\text{eff}} \nabla T) + S_h$$

Equation 4

$$\frac{\partial \rho}{\partial t} + \nabla \cdot (\rho \vec{v}) = S_m$$

Equation 5

$$\frac{\partial}{\partial t}(\rho \vec{v}) + \nabla \cdot (\rho \vec{v} \vec{v}) = -\nabla p + \nabla \cdot (\bar{\tau}) + \rho \vec{g} + \vec{F}$$

Equation 6

$$\bar{\tau} = \mu \left[ (\nabla \vec{v} + \nabla \vec{v}^T) - \frac{2}{3} \nabla \cdot \vec{v} I \right]$$

Equation 7

Fluent turbulence models are based off the Reynolds Averaged Navier-Stokes equations. The k-ε turbulence model was selected. The Large Eddy Simulation model could have also been chosen, but ultimately was not to save on computational time. The realizable k-ε model with standard wall functions was chosen. Species transport was enabled to allow for the use of multiple working fluids. The transport equations are as follows. The P terms represent the generation of turbulent kinetic energy (ANSYS 2013).

$$\frac{\partial}{\partial t}(\rho k) + \frac{\partial}{\partial x_j}(\rho k u_j) = \frac{\partial}{\partial x_j} \left[ \left( \mu + \frac{\mu_t}{\sigma_k} \right) \frac{\partial k}{\partial x_j} \right] + P_k + P_b - \rho \epsilon - Y_M + S_k$$

Equation 8

$$\frac{\partial}{\partial t}(\rho\epsilon) + \frac{\partial}{\partial x_j}(\rho\epsilon u_j) = \frac{\partial}{\partial x_j} \left[ \left( \mu + \frac{\mu_t}{\sigma_\epsilon} \right) \frac{\partial \epsilon}{\partial x_j} \right] + \rho C_1 S_\epsilon - \rho C_2 \frac{\epsilon^2}{k + \sqrt{\nu\epsilon}} + C_{1\epsilon} \frac{\epsilon}{k} C_{3\epsilon} P_b + S_\epsilon \quad \text{Equation 9}$$

Table X displays the simulation results for different mesh sizes as well as a comparison to an analytical solution calculated using Bernoulli's equation. This was done to validate the mesh and assess the accuracy of the model. Changing the cell size resulted in a maximum change of 1.26% between solutions which suggest a well meshed model. The percent error between the analytical solution and CFD analysis reached a maximum of 5.32% which shows that the model is well developed.

**Table X:** Mesh Validation and Analytical Solution Comparison

Cell Size (mm)	Velocity (m/s)	% Difference	% Error
0.5	194.15	1.26%	4.01%
1	196.59	0.67%	5.31%
2	195.28	0.67%	4.61%
5	196.60	-----	5.32 %

**Table XI:** Simulation Convergence Criteria

Residual	Convergence Criteria	Final Values
Continuity	1.00e-03	5.76e-03
X-velocity	1.00e-03	2.85e-05
Y-velocity	1.00e-03	3.43e-05
Z-velocity	1.00e-03	3.45e-05
Energy	1.00e-06	5.56e-06
K	1.00e-03	8.24e-04
Epsilon	1.00e-03	1.60e-03

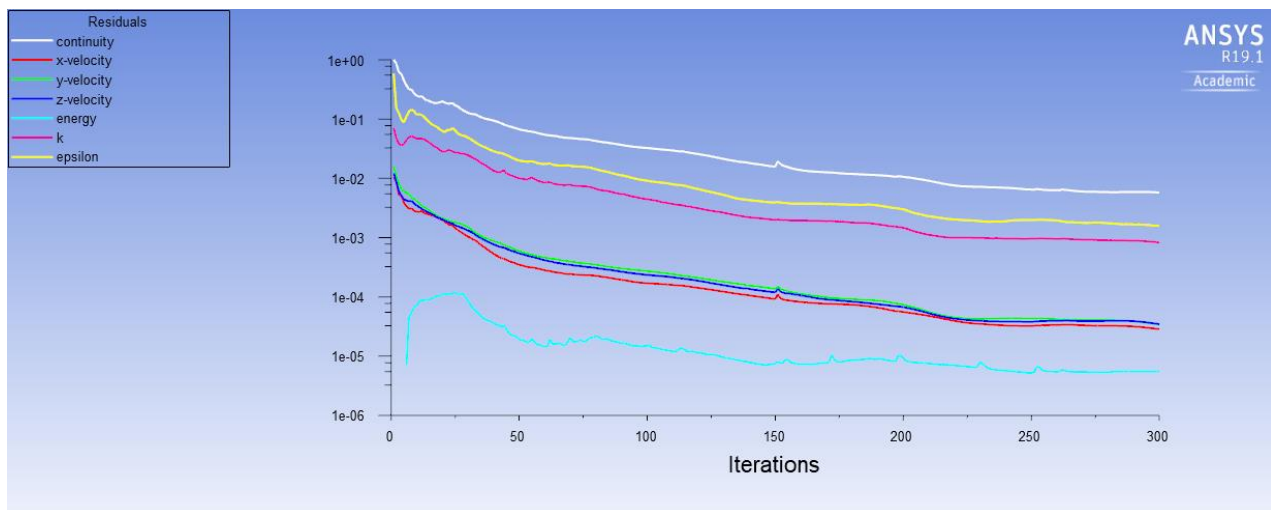
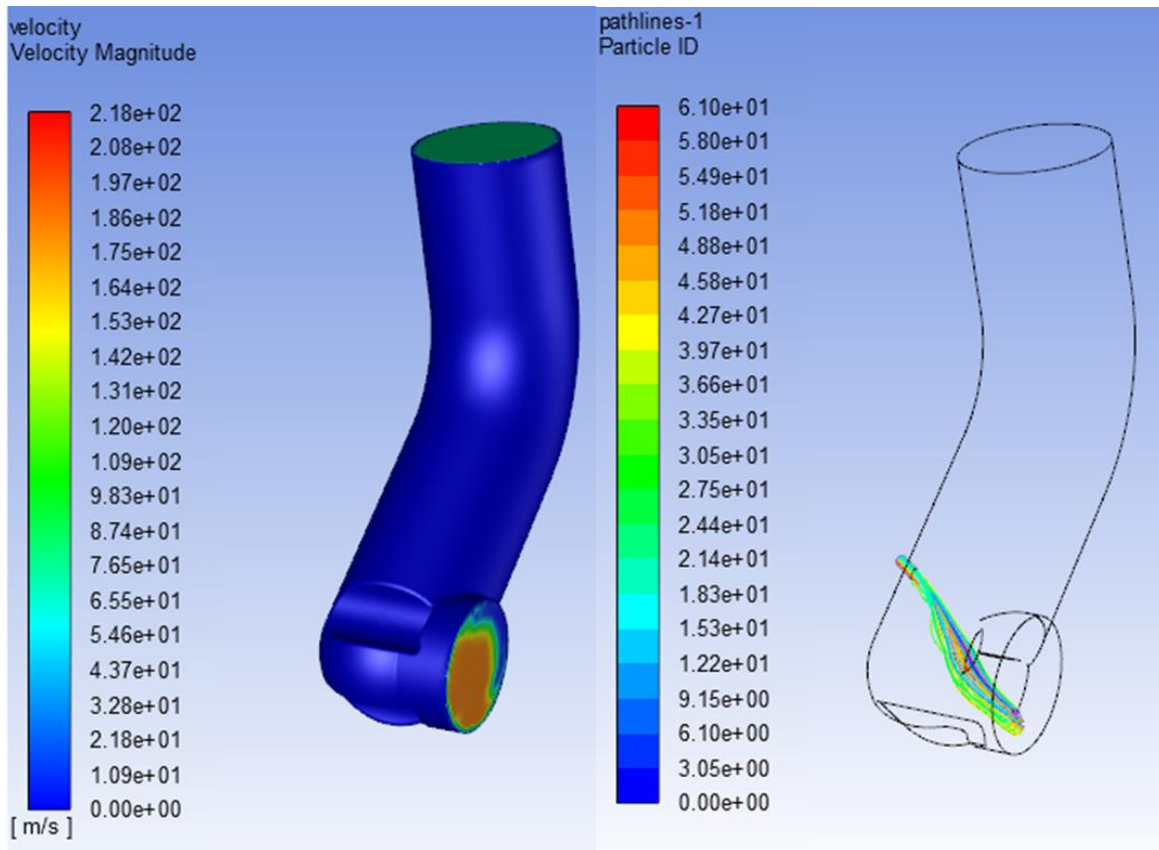
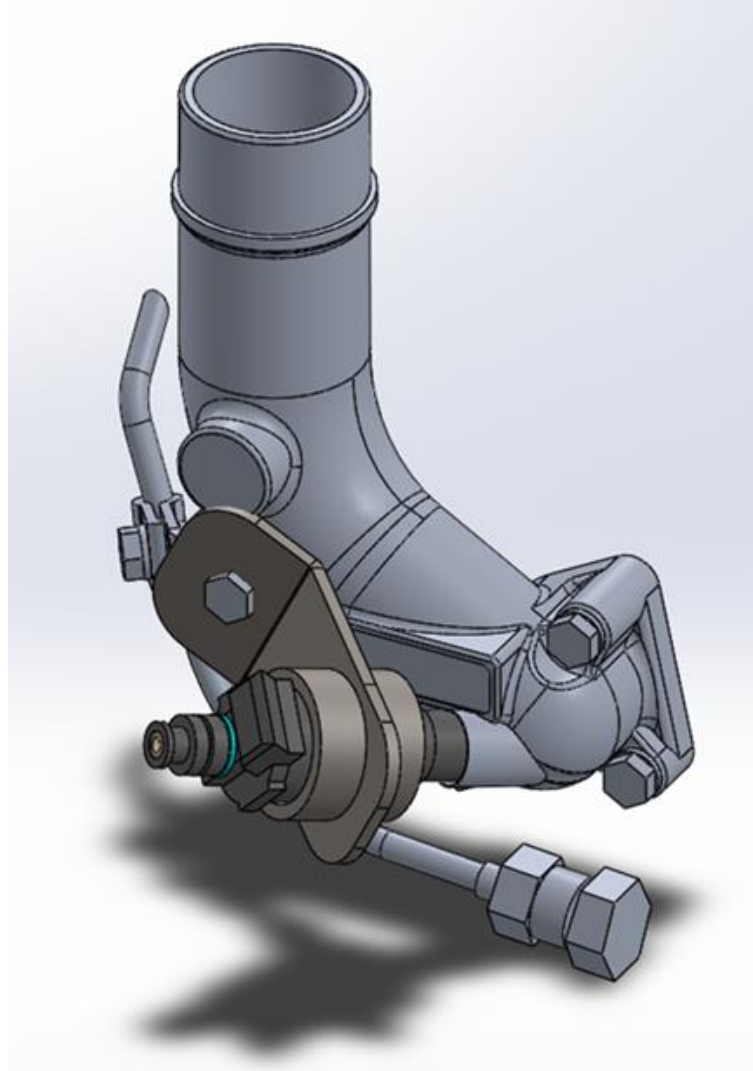
**Figure 28** CFD Residuals

Table XI and Figure 28 display the convergence criteria, and residuals for the simulation. These are displayed to show that convergence was reached. Figure 29 displays the velocity profile of air passing through the intake and the expected pathlines of a butanol injection.



**Figure 29** Velocity Contour (left) and PFI Pathlines (right)

Installation of the port fuel injector required the complete remanufacturing of the OEM intake. A 3D model of the intake design is depicted in Figure 30.



**Figure 30** Intake Design 3D Model

The manifold started out as an OEM aluminum intake, which was milled to make an opening for the port fuel injector. An aluminum collar was TIG welded over the opening and used to seat the injector. Figure 31 is a depiction of the finished intake complete with injector. It is bolted directly to the engine's intake port with the fuel injector pointing at a 70° angle to the face of the cylinder head. The injector was aimed at the intake valve face for optimum combustion characteristics based on the study conducted by Kato, Hayashida, & Lida (2008).

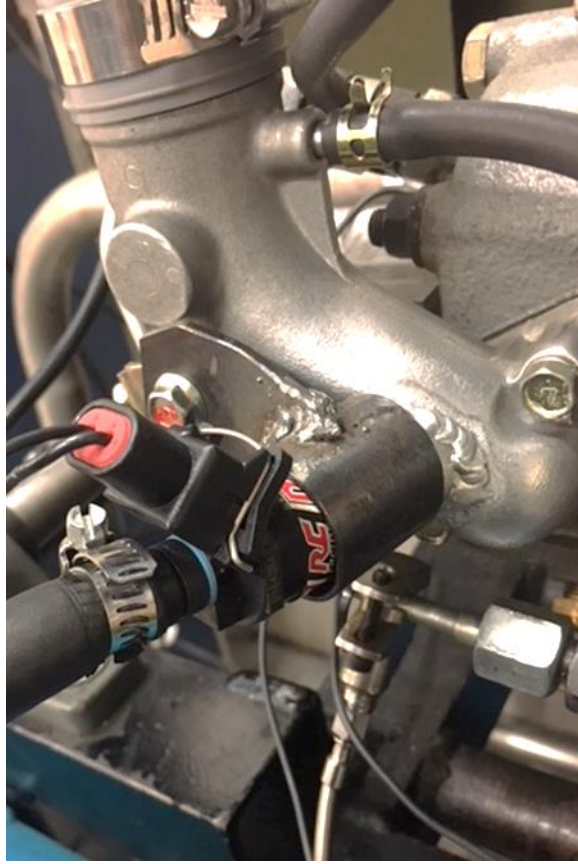


**Figure 31** Custom Intake Manifold and Injector

### 3.6.2 Injector Selection and Calibration

A peak and hold type injector was chosen for the application due to its' precision and response time. A generic sizing formula was used with some simplifying assumptions to size the injector. The average brake specific fuel consumption for a naturally aspirated engine is approximately 0.50 lbs/hr for each horsepower produced. The research engine has a single cylinder that produces 6.7 horsepower. The industry standard is that most injectors will max out at an 80% duty cycle.

$$\mathbf{Flow\ Rate} = \frac{\mathbf{HP*B.S.F.C}}{\mathbf{\#\ of\ Injectors*Duty\ Cycle}} = \frac{\mathbf{6.7*0.80}}{\mathbf{1*0.8}} = \mathbf{6.7\ lbs/hr}$$
 Equation 10

$$\mathbf{Flow\ Rate} = \mathbf{6.7\ \frac{lbs}{hr}} * \frac{\mathbf{0.454\ kg}}{\mathbf{1\ lb}} = \mathbf{3.04\ kg/hr}$$
 Equation 11

Based on calculations the PL2-155 injector from RC engineering was chosen. The

calculations above must be verified experimentally to ensure the accuracy of research done using the PFI system. This was done by measuring the amount of fuel released into a beaker and determining the volume per unit time. The test bench for this was developed in lab. Figure 33 displays the apparatus. An aftermarket ECU was used to control the injector actuation and the engine speed signal from the rotary encoder was simulated using a function generator.



**Figure 32** PL2-155 Peak and Hold Injector (Vivid Racing 2018)

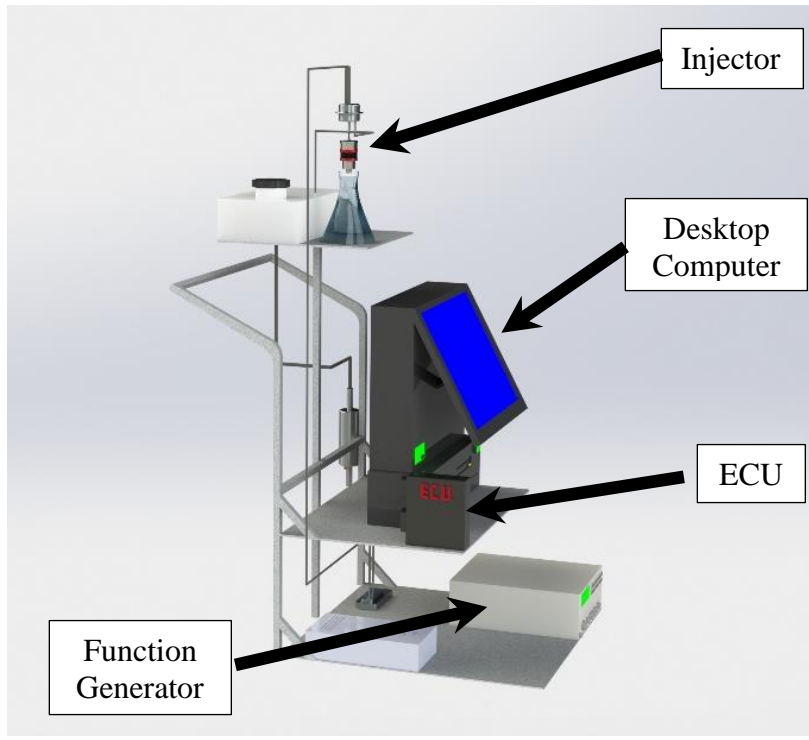


**Figure 33** Developed Injector Calibration Test Bench



Table XII: PL2-155 Injector Specifications

<b>Flow Rate – cc/min</b>	155 at 43.5 psi
<b>Flow Rate – lbs/hr</b>	15 at 43.5 psi
<b>Flow Rate – kg/hr</b>	6.8 at 43.5 psi
<b>Resistance</b>	2.5 ohms at 68 F
<b>Voltage</b>	8 – 15 volts, nominal 13 volts
<b>Amperage</b>	Peak 4 amps/ Hold 1.5 Amps
<b>Pressure</b>	Min 30 psig/Max 100 psig

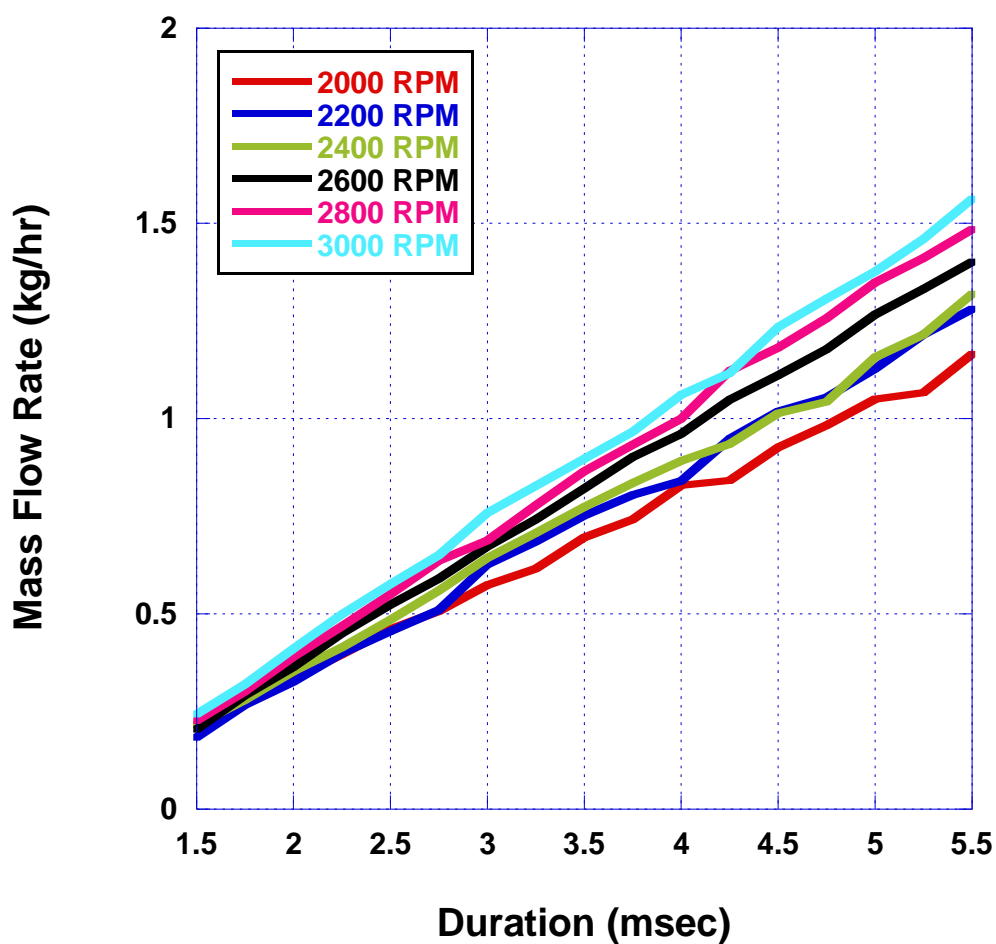
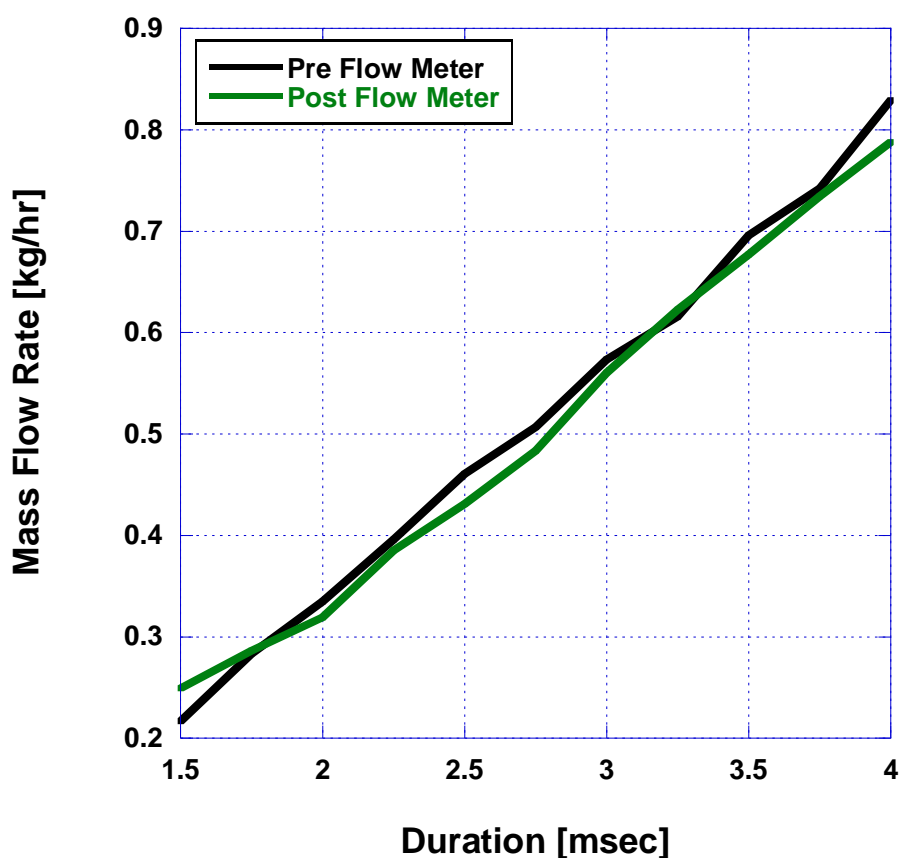


Figure 34 PL2-155 Peak and Hold Injector Calibration Curves

The injector was selected and installed before the flow meter used to record the mass flow rate. To verify that the flow meter had no major impact on the flow characteristics of the PFI system a calibration check was performed. A plot of the mass flow rates for the injector before and after the installation of the flow meter can be seen in Figure 35. This calibration was performed at a constant engine speed of 2000 rpm. An average difference of 4.0% was observed between the data used to generate both curves.



**Figure 35** Calibration Curves for the PL2-155 from Before and After the Flow Meter Installation

Table XIII contains the experimentally obtained mass flow rates of ULSD#2 through the main fuel injector at a constant speed of 2400 RPM and loads of 2, 3, and 4 bar BMEP.

**Table XIII:** Main Injector Mass Flow Rate at 2400 RPM

<b>Dyno Load (bar)</b>	<b>Fuel Mass Flow Rate (kg/hr)</b>
<b>2</b>	0.557
<b>3</b>	0.675
<b>4</b>	0.808

Table XIV contains calculated total mass flow rates to inject n-butanol as a specified percentage of the total mass flow rates from both fuels.

**Table XIV:** Total Fuel Mass Flow Rate at 2400 RPM

<b>Percent PFI</b>	<b>2 bar</b>	<b>3 bar</b>	<b>4 bar</b>
<b>10</b>	0.619	0.750	0.898
<b>20</b>	0.696	0.844	1.010
<b>30</b>	0.795	0.965	1.155
<b>40</b>	0.928	1.125	1.347
<b>50</b>	1.113	1.350	1.617
<b>60</b>	1.392	1.688	2.021
<b>70</b>	1.856	2.251	2.695
<b>80</b>	2.783	3.376	4.042

**Table XV:** Fuel Mass Flow Rate for the Port Fuel Injector at 2400 RPM

<b>Percent PFI</b>	<b>2 bar</b>	<b>3 bar</b>	<b>4 bar</b>
<b>10</b>	0.062	0.076	0.091
<b>20</b>	0.139	0.169	0.202
<b>30</b>	0.239	0.290	0.348
<b>40</b>	0.372	0.452	0.541
<b>50</b>	0.557	0.675	0.808
<b>60</b>	0.835	1.013	1.213
<b>70</b>	1.303	1.580	1.892
<b>80</b>	2.227	2.701	3.233

From the data in Table XIV the mass flow rates through the port fuel injector were calculated. These numbers were then verified using the calibration curve for the port fuel injector. Injector duration for the PFI injector for loads ranging from 2 to 4 bar were calculated. By increasing the injector duration to the maximum of 13.00 ms PFI percentage of 80% can theoretically be supported at all loads. These values can be found in Table XVI.

**Table XVI: Port Fuel Injector Duration at 2400 RPM**

<b>Percent PFI</b>	<b>2 bar</b>	<b>3 bar</b>	<b>4 bar</b>
<b>10</b>	0.90	0.95	1.02
<b>20</b>	1.19	1.30	1.43
<b>30</b>	1.57	1.76	1.97
<b>40</b>	2.06	2.36	2.70
<b>50</b>	2.75	3.20	3.70
<b>60</b>	3.80	4.46	5.21
<b>70</b>	5.55	6.57	7.75
<b>80</b>	9.00	10.87	12.78

### *3.6.3 ECU Selection and Programming*

The EMS 8860 sequential motorsports ECU was selected for control of the fuel delivery. The ECU was chosen because it was already available and researchers are already familiar with the equipment. It is a fully programmable control module capable of closed loop control using either analog or digital inputs. The ECU uses information from sensors and a fuel map developed in this research to calculate the amount of fuel needed for engine operation. The two main feedback sensors required for proper operation are the variable reluctance (VR) speed sensor and the throttle position sensor (TPS). The VR sensor provides the ECU with crank

rotation speed and position in a 360° degree revolution. The TPS sensor measures the percentage of throttle opening from 0-100%. A potentiometer was used to simulate a throttle.

### Electrical

The ECU required an extensive wiring system to provide for the sensor connections and power source supply. For this purpose a wire schematic was designed, as can be seen in Figure 36.

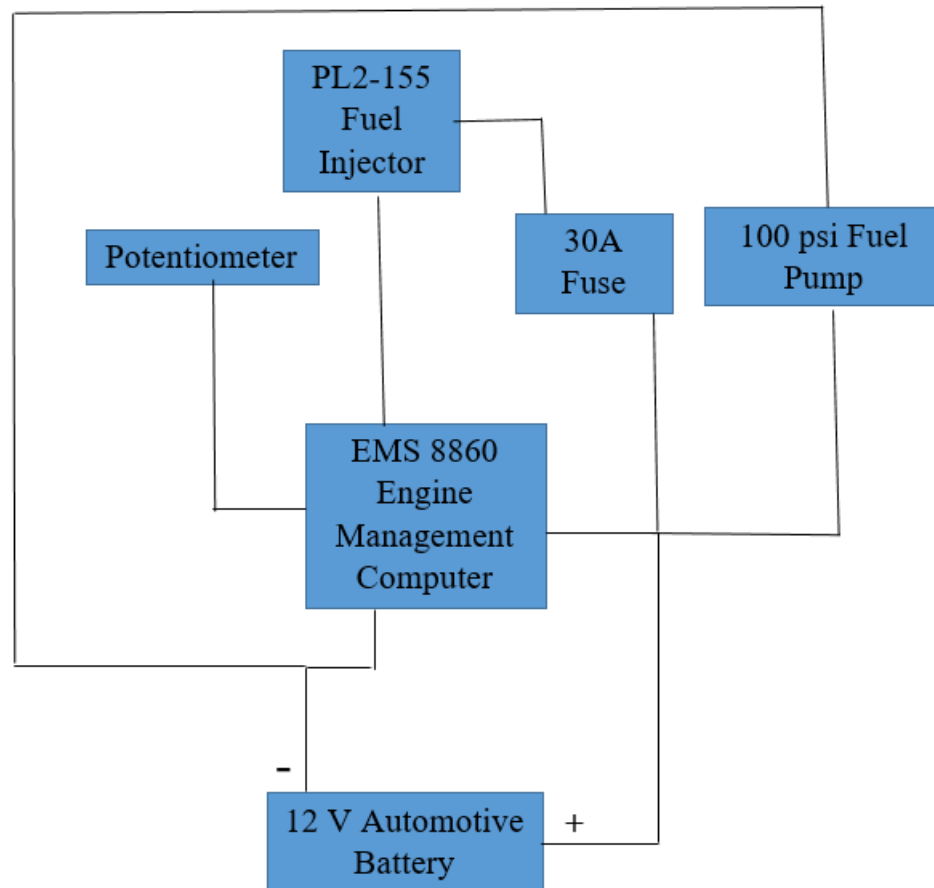


**Figure 36** Wire Schematic for Engine Control Unit

The TPS sensor is a variable potentiometer which required a 5V supply and a sensor GND from the ECU. The signal output is 0-5V. The injector on time has a

maximum value of 20 ms. Each load point allows for 255 increments. Allowing for the injection duration to be varied from 0 – 20 ms in 1/255 increments.

Based on these two sensors the ECU is able to plot its place on a fuel map that is a three dimensional map of speed (RPM), load (TPS %) and amount of fuel to be injected (injector open time). A sample fuel map can be seen in Figure 37 and with the input values shown in Figure 38. The ECU setup parameters are displayed in Figure 39.

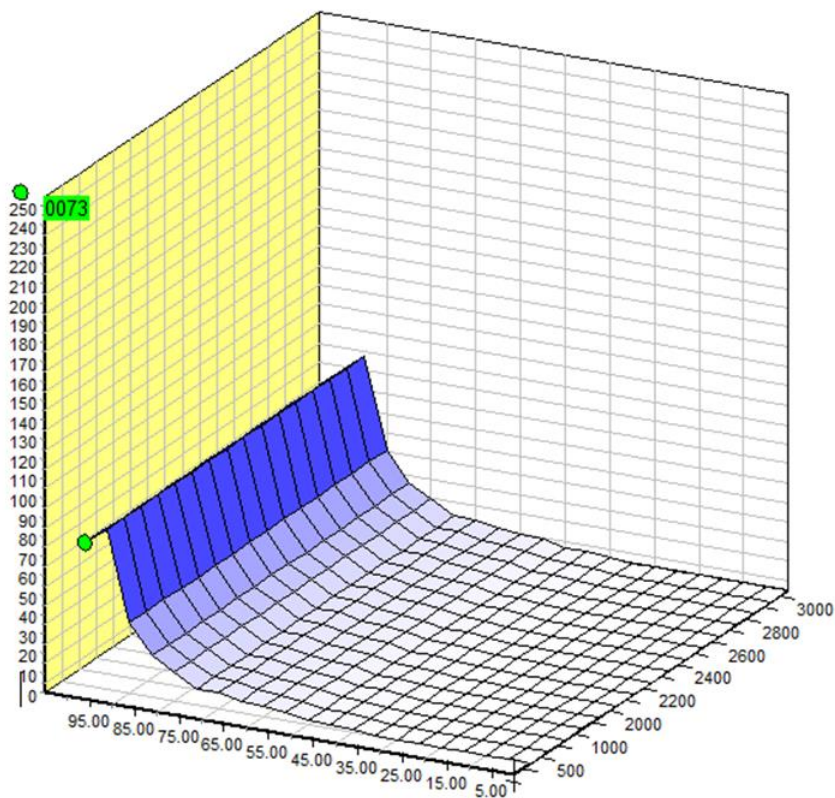


**Figure 37** Sample Fuel Map from the EMS 8860

Fuel Map 1	Fuel Map 2												
21/16	0	500	750	1000	1500	2000	2100	2200	2300	2400	2500	2600	2700
100.00 %	0073	0073	0073	0073	0073	0073	0073	0073	0073	0073	0073	0073	0073
95.00 %	0082	0082	0082	0082	0082	0082	0082	0082	0082	0082	0082	0082	0082
90.00 %	0036	0036	0036	0036	0036	0036	0036	0036	0036	0036	0036	0036	0036
85.00 %	0021	0021	0021	0021	0021	0021	0021	0021	0021	0021	0021	0021	0021
80.00 %	0015	0015	0015	0015	0015	0015	0015	0015	0015	0015	0015	0015	0015
75.00 %	0008	0008	0008	0008	0008	0008	0008	0008	0008	0008	0008	0008	0008
70.00 %	0008	0008	0008	0008	0008	0008	0008	0008	0008	0008	0008	0008	0008
65.00 %	0006	0006	0006	0006	0006	0006	0006	0006	0006	0006	0006	0006	0006
60.00 %	0005	0005	0005	0005	0005	0005	0005	0005	0005	0005	0005	0005	0005
55.00 %	0004	0004	0004	0004	0004	0004	0004	0004	0004	0004	0004	0004	0004
50.00 %	0002	0002	0002	0002	0002	0002	0002	0002	0002	0002	0002	0002	0002
45.00 %	0002	0002	0002	0002	0002	0002	0002	0002	0002	0002	0002	0002	0002
40.00 %	0001	0001	0001	0001	0001	0001	0001	0001	0001	0001	0001	0001	0001
35.00 %	0000	0000	0000	0000	0000	0000	0000	0000	0000	0000	0000	0000	0000
30.00 %	0000	0000	0000	0000	0000	0000	0000	0000	0000	0000	0000	0000	0000
25.00 %	0000	0000	0000	0000	0000	0000	0000	0000	0000	0000	0000	0000	0000
20.00 %	0000	0000	0000	0000	0000	0000	0000	0000	0000	0000	0000	0000	0000

Figure 38 PL2-155 Port Fuel Injection Fuel Map Inputs

EMS MotorSport Tuning System

File ECU Goto Application Settings Help

### ECU Settings

Load Source  
Load Source One: Throttle Position Sensor  
Load Source Two: Off

Sensor Setup  
Trigger Sensor: Mag  
Trigger Edge: Rising (+)  
Trigger Pull Up Resistor: Off  
Sync Sensor: Mag  
Sync Edge: Rising (+)  
Sync Pull Up Resistor: Off

Ignition Setup  
Ignition Type: Normal  
No. of teeth per cam cycle: 64 Teeth  
Static Timing Tooth: None  
Sync sensor used: No

Engine Control  
Injection arrangement: Multi Point 360  
No of Cylinders: 1 Cylinder  
Number of Igniters: 1 Igniter  
Ign Fire Edge: Rising (+)  
Ign Delay Compensation: 0 micro Sec  
Dwell mS: 0 ms  
Injector Ohms: 2.5 ohms  
Sensitivity: Normal  
Aspiration: Normal/Turbo  
Supercharger Boost: -100.0 KPA  
Acceleration Enrichment: 0.00 %  
Enrichment Duration: 0  
Soft Rev limiter: 3000  
Hard Rev limiter: 3500  
Boost Cut: Off  
Deceleration fuel cut: Not used

Calibrate Throttle Position Sensor  
Read Closed Throttle: 0  
Read Open Throttle: 960  
Use Throttle Sensor:

Closed Loop Lambda  
Lambda Sensor: Off  
Allowable Change +/-: 20 %  
Target A/F Ratio: 15.8  
Operating Range: -20 Kpa

Flex Fuel  
Use Flex Fuel Sensor:   
Sensor Failure Default %: 126

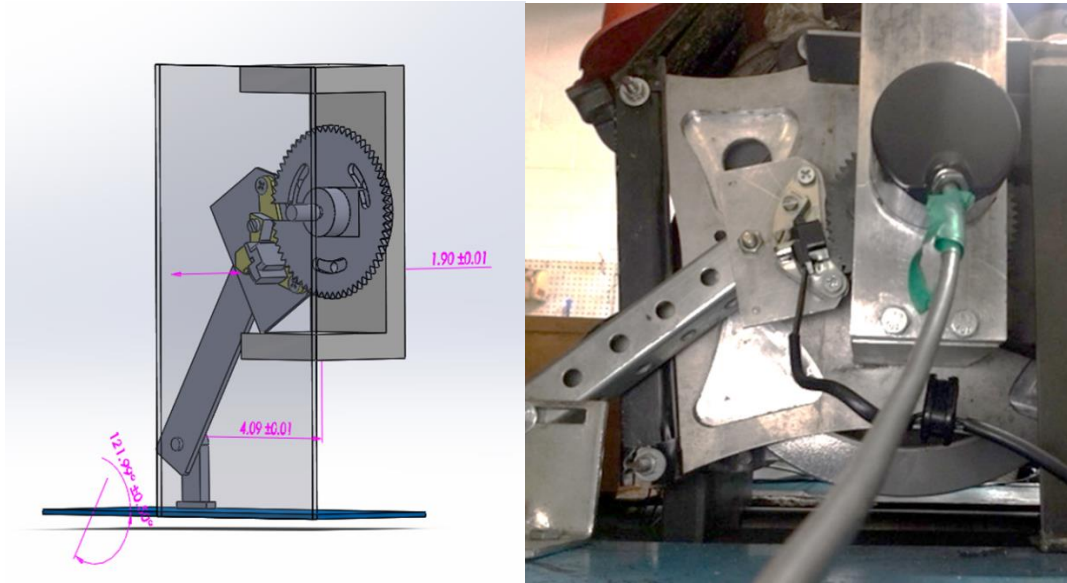
Load Setup Save Setup

Figure 39 EMS 8860 Setup Parameters

### *3.6.4 Trigger Mechanism Design*

The EMS ECU is capable of controlling both the fuel injection and ignition control system for most two and four-stroke engines. For this application only the fuel injection functionality is being used. The ECU only requires a few inputs to accomplish this. Throttle position and an indication of engine speed are all that are required to trigger the injection event. The throttle position was simulated using a potentiometer. The engine speed and injection timing for the port fuel injector was determined by using a standard steel pickup wheel attached to the output shaft of the engine. The trigger wheel for crankshaft position had to be custom fabricated and precisely aligned. The trigger wheel started out as a sheet of ferrous steel that was cut into a 64-tooth drive sprocket with one missing tooth. Cutting operations were conducted using a water jet. A variable reluctance sensor was installed on to the engine test bench and was wired into the ECU. This VR sensor used the trigger wheel as a reference for where the engine was in rotation. For this reason it had to be mounted very precisely and within three thousands of an inch tolerance. Any contact of the trigger wheel and the pickup would destroy the sensor. The trigger wheel also had to be oriented in such a way that the missing tooth would line up with top dead center (TDC) of the engine. This combination of hardware allowed the ECU to determine engine speed and injection timing very precisely.





**Figure 40** VR Sensor Solid Model and Fabricated Part

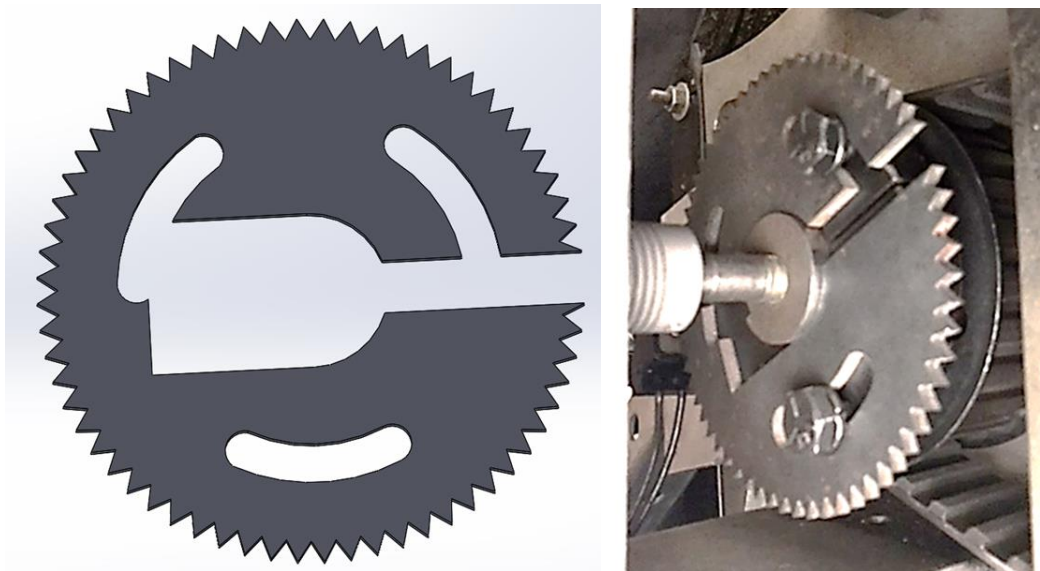


**Figure 41** Trigger Wheel Solid Model and Fabricated Part

Material has been removed from the trigger wheel itself. This serves the function of balancing the wheel. For rotating solid bodies, rotation about an axis not located at the parts center of gravity can cause oscillations that can introduce noise in data acquisition equipment or cause damage to the rotating parts. Figure 42 is a screenshot of mass evaluations for the trigger wheel

and bushing using Solidworks 2018. Because each solid model has its center at the origin and normal to the axis of rotation (Z-axis) the parts needed to have a center of gravity with X and Y coordinates of zero.

Center of mass: ( millimeters )  
 X = 0.10  
 Y = 0.07  
 Z = 1.40

**Figure 42** Mass Evaluation of the Trigger Wheel

A frequency analysis was performed using ANSYS Workbench 18.1 to verify that the trigger wheel design is balanced. The Campbell plot can be seen in Figure 43. The trigger wheel was subjected to a rotational speed ranging from 2000 RPM to 3000 RPM. The first six natural frequencies were found. These can be viewed in Table XVII. Each mode is stable and below the critical speed of the part. This suggest that the trigger wheel is well balanced and can safely be used for the application.

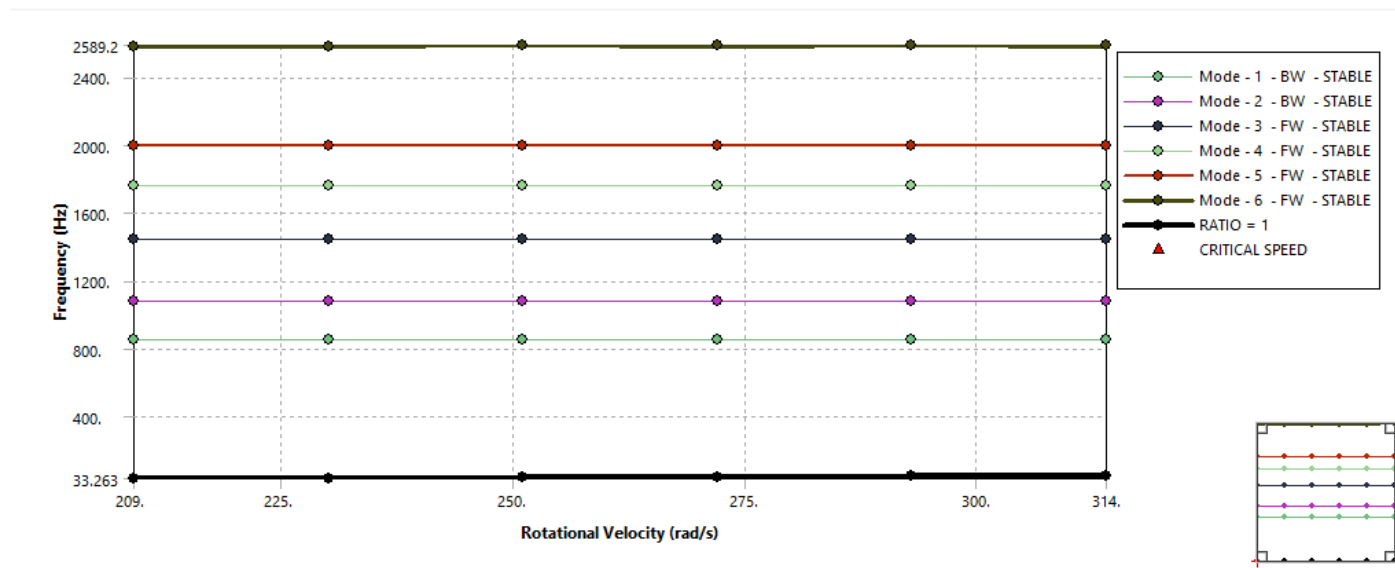


**Figure 43** Campbell Plot of the Trigger Wheel

**Table XVII:** Frequency Analysis Results 3000 RPM

<b>Mode</b>	<b>Whirl Direction</b>	<b>Mode Stability</b>	<b>Critical Speed</b>	<b>Natural Frequency</b>
<b>1</b>	BW	Stable	None	851.7 Hz
<b>2</b>	BW	Stable	None	1079.9 Hz
<b>3</b>	FW	Stable	None	1443.1 Hz
<b>4</b>	FW	Stable	None	1764.4 Hz
<b>5</b>	FW	Stable	None	1998.7 Hz
<b>6</b>	FW	Stable	None	2589.2 Hz

### 3.7 Metrics for Success

The metrics for success are defined by simultaneously reducing NO<sub>x</sub> and soot emissions with dual fuel combustion while exceeding or meeting EPA regulations for small displacement, non-road diesel engines. Engine out NO<sub>x</sub> + UHC emissions must be lower than 7.5 g/kWhr, soot emissions must be lower than 0.4 g/kWh, and CO emissions must be lower than 8.0 g/kWhr without the need for exhaust after-treatment systems. An optimal dual fuel strategy must be developed to produce these emission reductions while maintaining desirable combustion characteristics.

## CHAPTER 4: DATA ANALYSIS

## 4.1 Fuel Properties

Both the physical and chemical properties influence the ignition and combustion of the fuel, which in turn influences the performance and emissions characteristics. The properties of the fuel will also affect the longevity of the engine and of its critical components. Due to this, the quality of the fuel being used must be assessed to fully understand the effect it will have on the combustion process.

The values that were determined experimentally were comparable to values found in the literature. Table XVIII below presents the fuel properties of ULSD#2 and n-butanol.

**Table XVIII: Fuel Properties**

<b>Property</b>	<b>ULSD #2</b>	<b>n-Butanol</b>
<b>Cetane Number<sup>A</sup></b>	47.21	16.4
<b>Density @ 20°C (g/cm<sup>3</sup>)<sup>A</sup></b>	0.850	0.790
<b>Dynamic Viscosity @ 40° C (cP)<sup>A</sup></b>	2.34	1.78
<b>LHV (MJ/kg)<sup>A</sup></b>	42.6	33.7
<b>Ignition Delay (ms) (CVCC)<sup>A</sup></b>	3.47	40.16
<b>Combustion Delay (ms) (CVCC)<sup>A</sup></b>	5.12	81.25
<b>Latent Heat of Vaporization (kJ/kg)*</b>	233	595
<b>Flashpoint (°C)**</b>	53.5	35

\*(Lapuerta et al. 2010), \*\*(Soloiu and Moncada<sup>A</sup> 2018), <sup>A</sup> Determined experimentally in lab

#### *4.1.1 Dynamic Viscosity*

Viscosity is one of many important factors that go into determining if a fuel is applicable for commercial use. It influences droplet diameter and vaporization rate. Increased viscosity can cause poor atomization which can lead to soot production and deposit formation, and lower viscosities can accelerate injector wear due to a decrease in lubricity (Soloiu and Moncada<sup>A</sup> 2018). The viscosity of the test fuels was determined using a Brookfield Viscometer DV-II Pro Type. The viscosity was determined over a temperature range of 26-60°C in increments of 2°C. Figure 44 below presents the viscosity vs. temperature diagram for each of the tested fuels. The n-butanol had a lower viscosity than ULSD at all points. This was expected given the lower density and lubricity of the alcohol based fuel when compared to diesel.

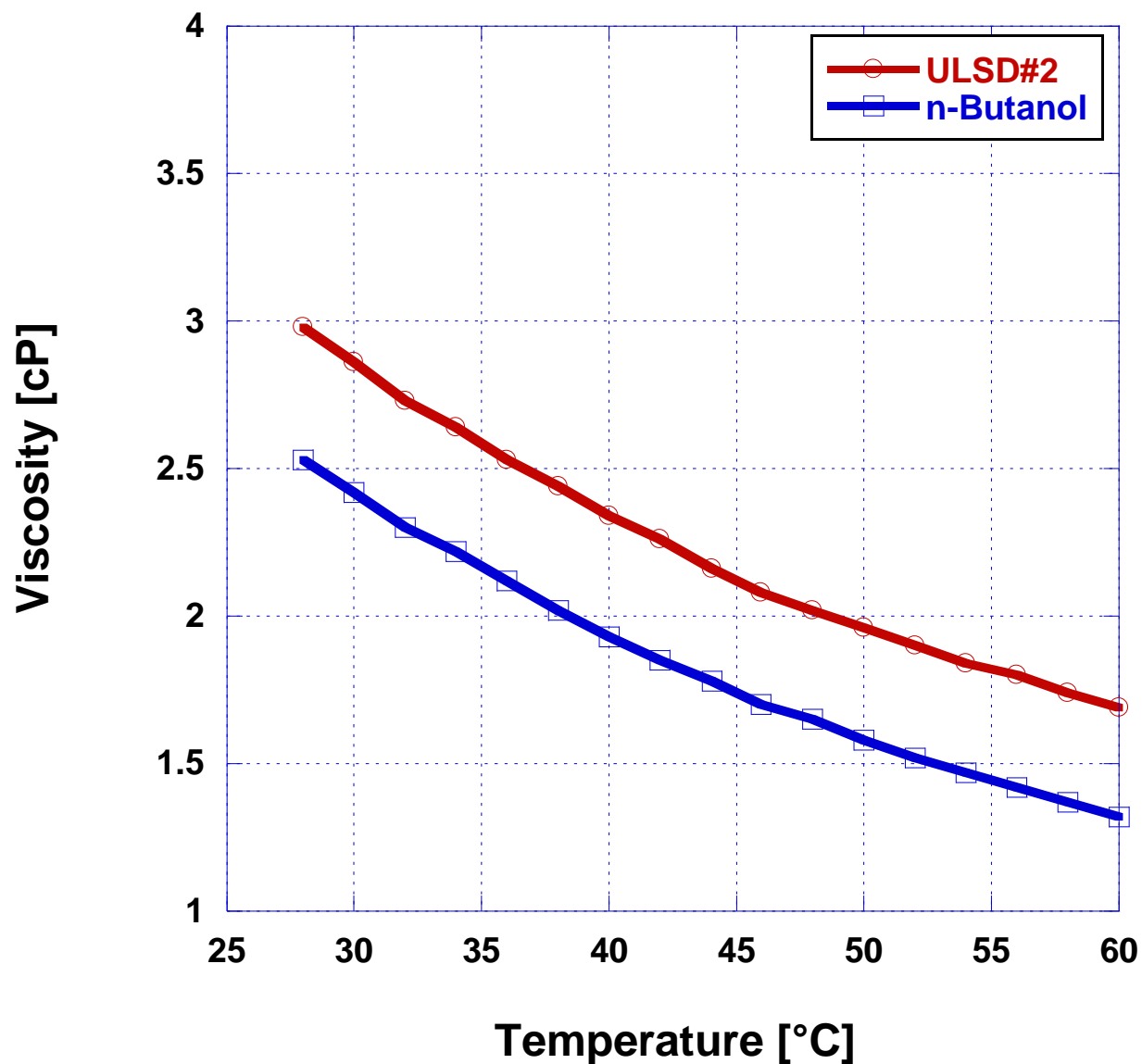
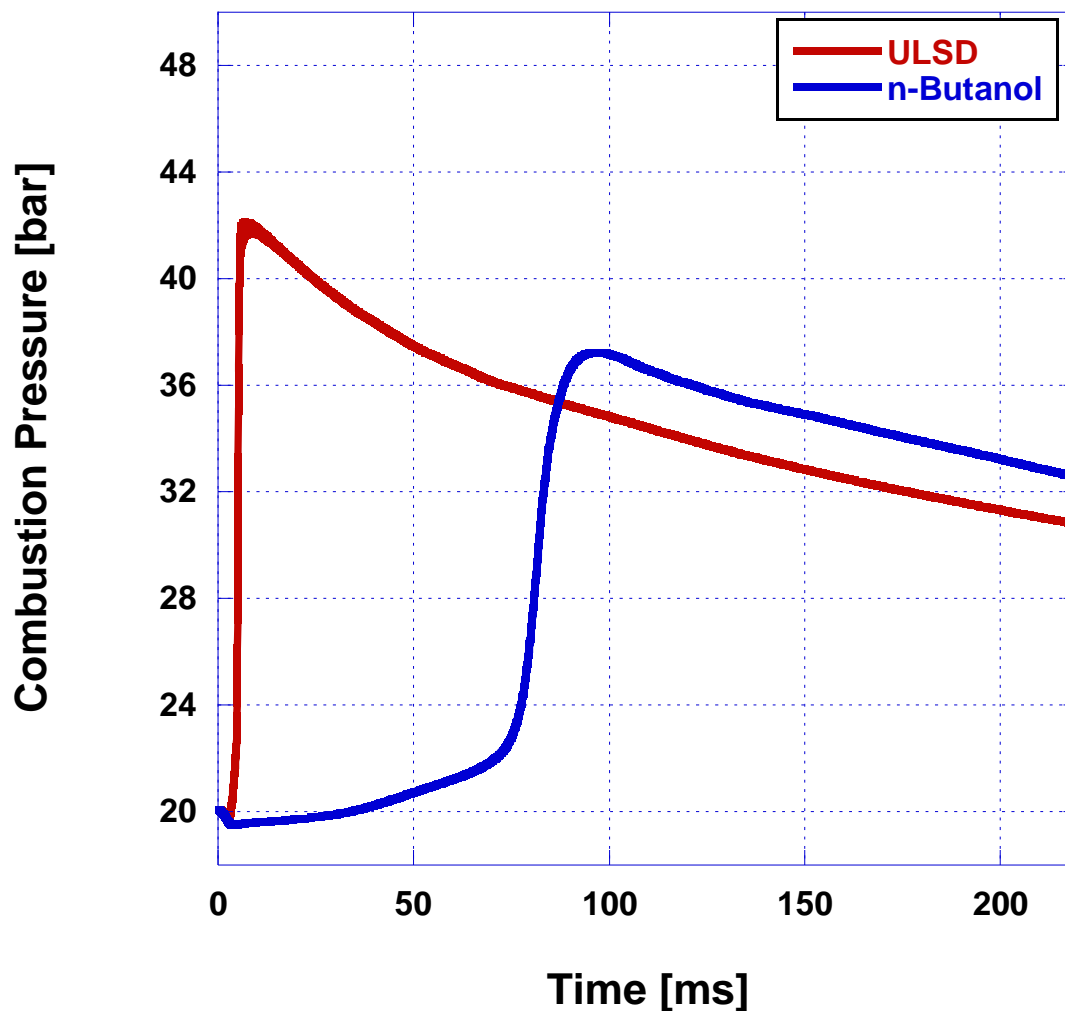


**Figure 44** Viscosity vs. Temperature of All Tested Fuels

#### 4.1.2 Ignition Quality

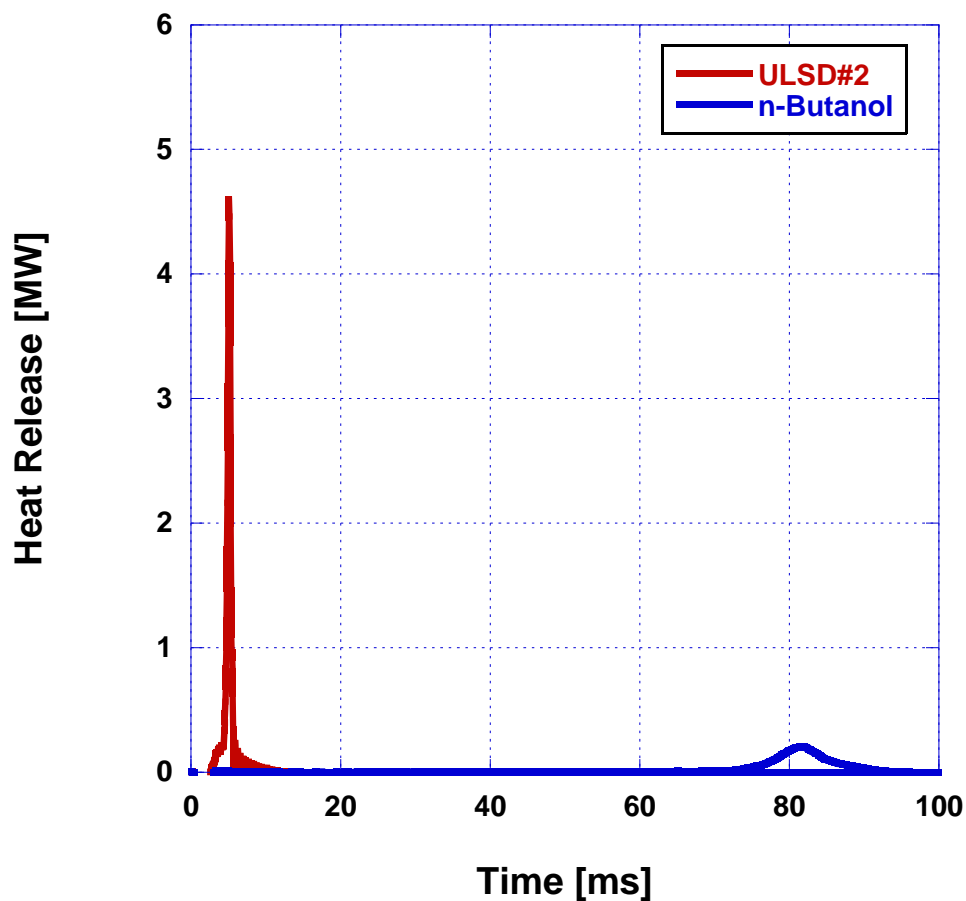
Three graphs were created to illustrate the difference between the two fuels, including the combustion pressure, apparent heat release rate (AHRR), and combustion temperature versus time.

Figure 45 is a plot of the combustion pressure for both fuels.



**Figure 45** Combustion Pressure of ULSD and n-Butanol in the Constant Volume Combustion Chamber

The reference parameters for both fuel test were constant. Temperature was kept at 595.5 °C, and initial chamber pressure was kept at 20 bar. The temperature of the cooling fluid was maintained at 50 °C. Injection pressure was held at 1000 bar for 2500 milliseconds. The curve for n-butanol can be observed to decrease in pressure due to the high latent heat of vaporization that is characteristic of this alcohol (Soloiu and Moncada<sup>A</sup> 2018).



**Figure 46** ULSD Heat Release Rate and n-Butanol in the Constant Volume Combustion Chamber

As observed in Figure 45, there was an oscillation in the combustion pressure of neat ULSD as well as an oscillation in the apparent heat release rate (shown in Figure 46). The oscillations in the graphs are indications of ringing within the constant volume chamber. The oscillations correlate to delayed combustion of small amounts of fuel that create a shock wave that is detectable by the pressure transducer inside the chamber. In Figure 46 it was observed that the apparent heat release output of neat n-butanol was significantly less, the low temperature heat release region was much longer, and the negative temperature coefficient region was much longer. Due to the slower pressure rise rate, the combustion delay is delayed. The longer NTC region of the n-butanol is a result of its' weaker ignition reactivity when compared to neat ULSD.



With longer CD being present for the alcohol, the result is a lower derived cetane number. The CVCC uses Equation 12 to calculate the DCN, using an average ignition delay and CD from a sweep of 15 injections.

$$DCN = 13.028 + \left(\frac{-5.3378}{ID}\right) + \left(\frac{300.18}{CD}\right) + \left(\frac{-1267.90}{CD^2}\right) + \left(\frac{3415.32}{CD^3}\right) \quad \text{Equation 12}$$

The DCN of n-butanol was calculated to be 65% lower than that of the DCN of ULSD. The high combustion delay, and the low apparent heat release rate resulted in a lower temperature distribution, shown in Figure 46.

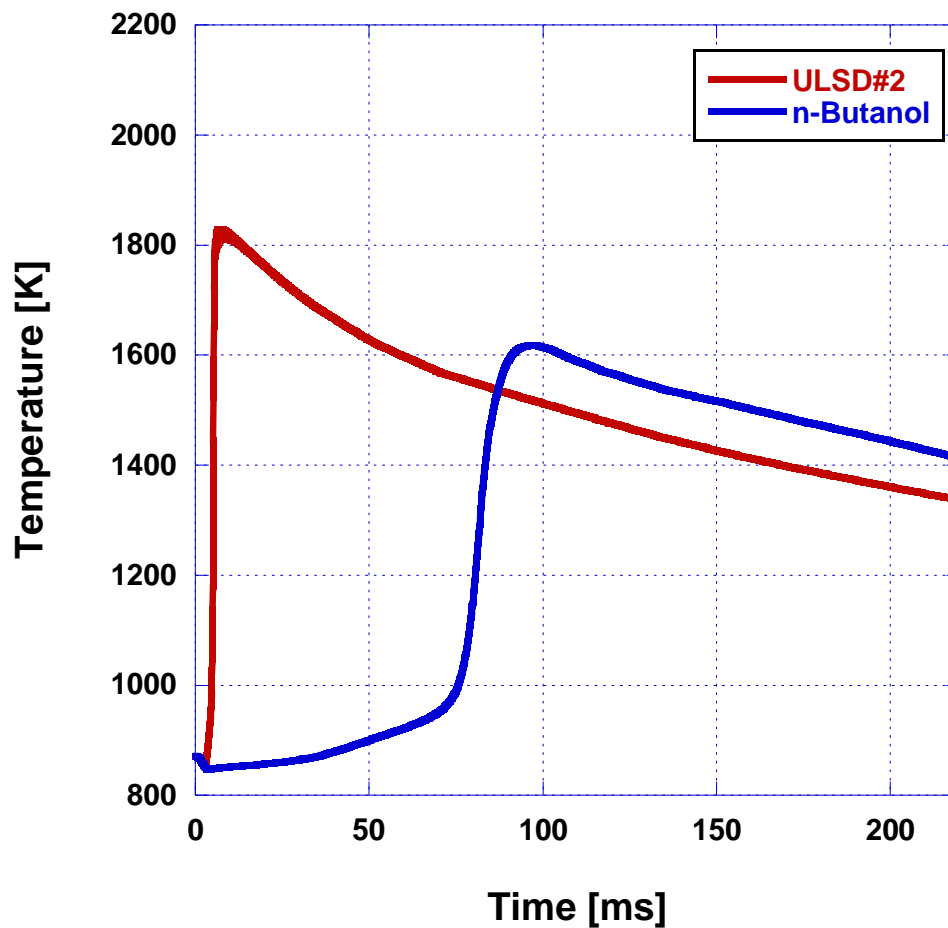


**Figure 47** Combustion Temperature of ULSD and n-Butanol in the Constant Volume Combustion Chamber.

The combustion temperatures of the two fuels reached the same maximum temperature. The major difference in the temperatures is the amount of time that it took the n-butanol to fully combust when compared to the ULSD.

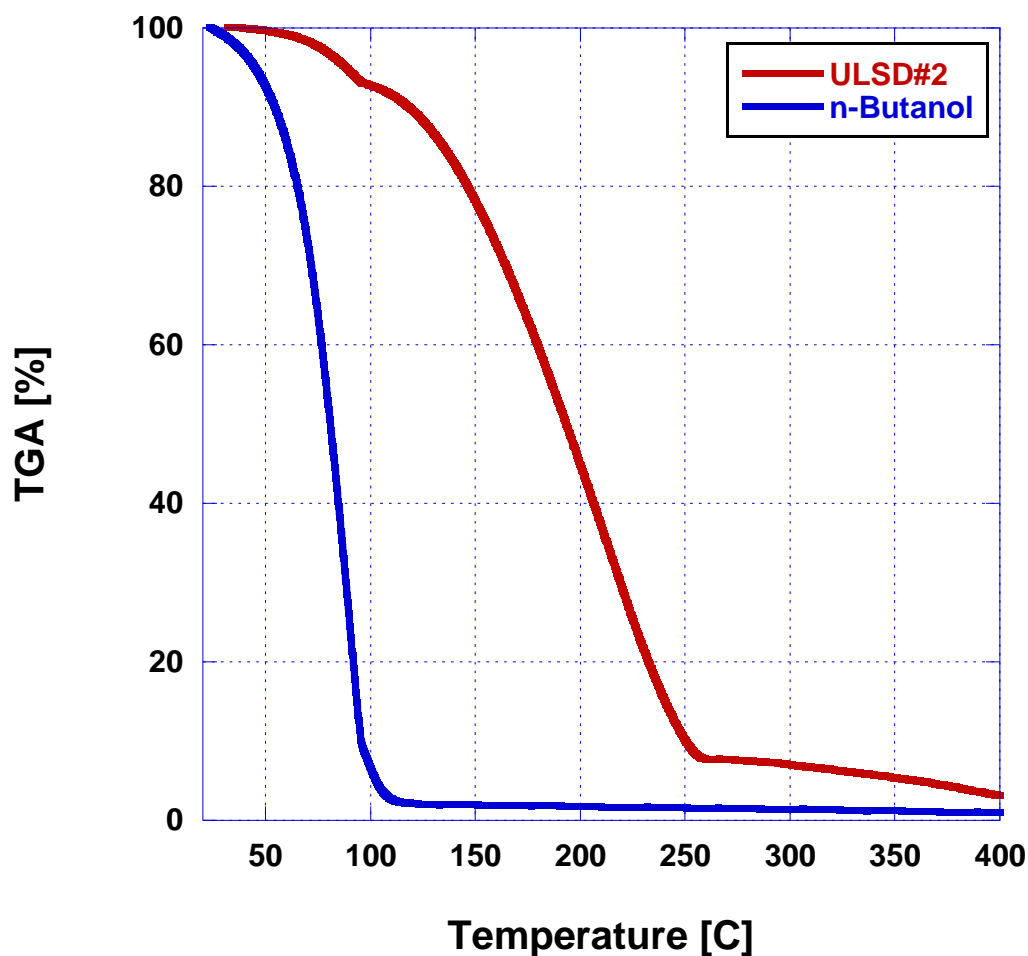
#### *4.1.3 Thermo-Gravimetric and Differential-Thermal Analysis*

The thermal gravimetric analysis (TGA) and differential thermal analysis (DTA) was performed on a Shimadzu DTG-60. An analysis of ULSD#2 and n-butanol was performed. Vaporization characteristics are determined from the TGA curve and endothermic and exothermic reactions are determined from the DTA curve. The TGA curve indicates the fuel's vaporization temperature and speed of vaporization. An increase in vaporization temperature indicates an increase in the droplets' momentum and an increase in the duration of travel time inside of the combustion chamber and the higher possibility of wall impact (Soloiu 2014). Lower vaporization temperatures are desirable because they lead to an increase in mixing in cylinder which facilitates a more complete combustion.

The results of the experiment are displayed in Figure 48 and Table XIX below. The TGA showed a decrease in vaporization temperature for n-butanol when compared to ULSD#2. The alcohol fuel began to vaporize at 54°C while ULSD#2 maintained stability until 110°C. n-Butanol then vaporized rapidly with TA50 and TA90 occurring at 80.8°C and 95.42°C respectively. The increase in vaporization rate could be related to the oxygen content of the fuel facilitating initial oxidation (Soloiu and Moncada<sup>A</sup> 2018). The differential thermal analysis results show that ULSD#2 reaches its maximum endothermic reaction around 190°C (absorbing the lower heat of vaporization). The maximum exothermic reaction (heat release) for ULSD#2 occurred around 300°C and lasted to approximately 375°C. The DTA of the alcohol fuel showed a maximum

endothermic reaction around 97°C (much higher than that of ULSD). n-butanol displayed exothermic reaction from 160°C to 340°C.

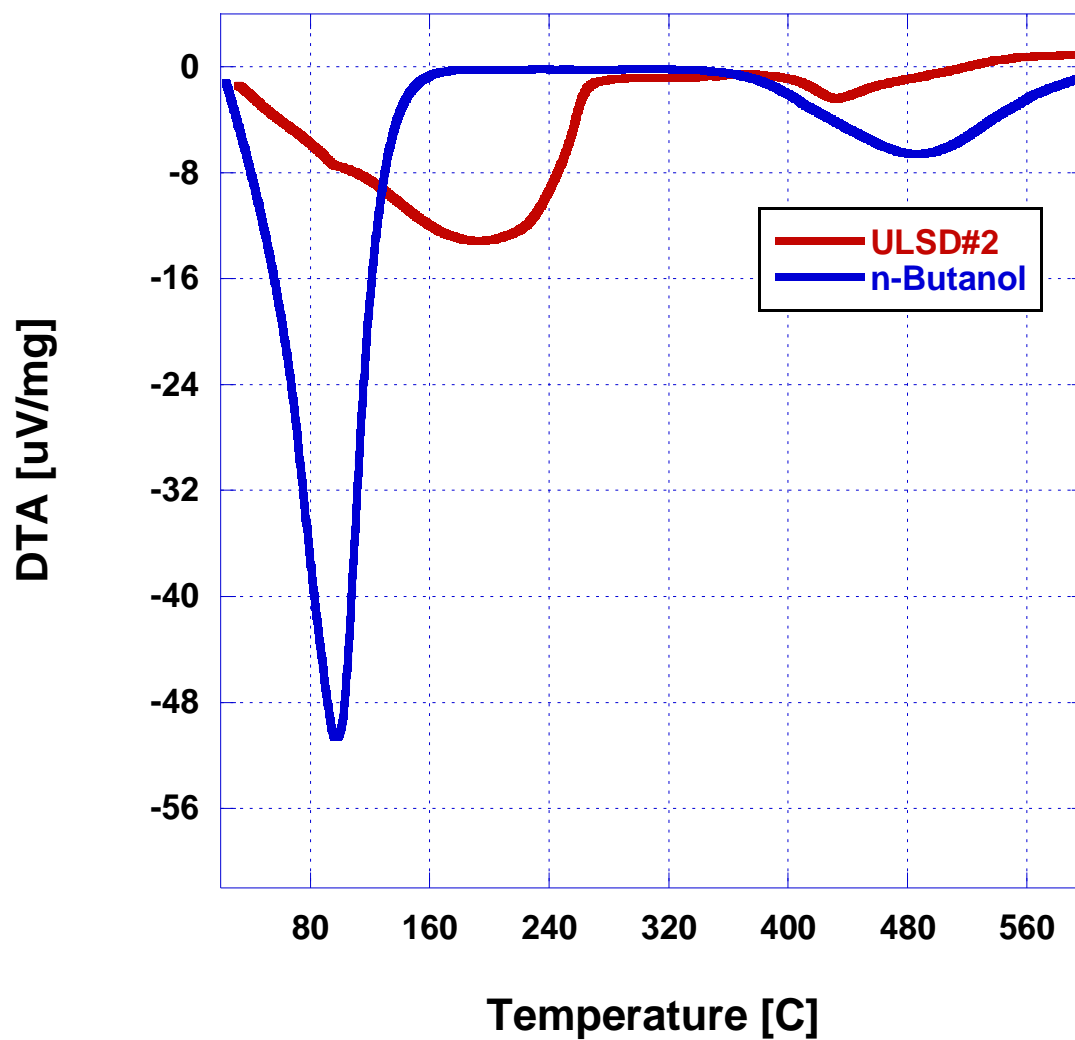
The energy release of the fuels is split into two stages. The initial endothermic reaction is due to oxidation. The second reaction takes place at high temperatures as a result of pyrolysis. The high latent heat of vaporization of butanol can be seen in the initial endothermic reaction. This is almost 5 times the magnitude of ULSD#2. This large absorption of energy creates a cooling effect in cylinder which has an impact on the formation of certain emissions species.



**Figure 48** TGA for ULSD#2 and n-Butanol

**Table XIX:** Thermal Gravimetric Analysis

	<b>ULSD#2</b>	<b>n-Butanol</b>
<b>TA10 (°C)</b>	110.05	54.35
<b>TA50 (°C)</b>	180.64	80.80
<b>TA90 (°C)</b>	239.63	95.42

**Figure 49** DTA for ULSD#2 and n-Butanol

#### *4.1.4 Mie Scattering Spray Analysis*

The fuel spray atomization determines the quality of the combustion and affects the amount of emissions produced. Efficient combustion is largely influenced by the size and distribution of the droplets. A decrease in the droplet size increases the surface area and increases the vaporization and air entrainment (Soloiu 2015). Spray analysis was performed with a Malvern Mie Scattering Laser using a 1×0.200mm pintle tip injector (same type as on the engine). The spray test injection pressure matched that of the experimental setup. The results of the analysis are shown in Figure 50. The figure presents the average of ten sprays for various blends shows the average SMD resulting by statistical analysis. SMD is shown as a function of time.

The results display a continuous increase in SMD with time for both fuels. Similar numbers were obtained for ULSD#2 and n-butanol with the alcohol based fuel having slightly larger values for  $D_v(10)$ ,  $D_v(50)$ , and  $D_v(90)$ , which are the largest droplet SMD for 10%, 50%, and 90% of the spray volume. This is most likely a result of a drop in injection pressure caused by the lower density and higher volatility of the alcohol fuel when compared to neat ULSD#2. Peak volume frequency distributions indicate the droplet size that is the most prevalent. This peak is around 34  $\mu\text{m}$  at 7% for both ULSD#2 and n-butanol. Table XX lists the particle size by volume and the percent spray volume under 10  $\mu\text{m}$ .

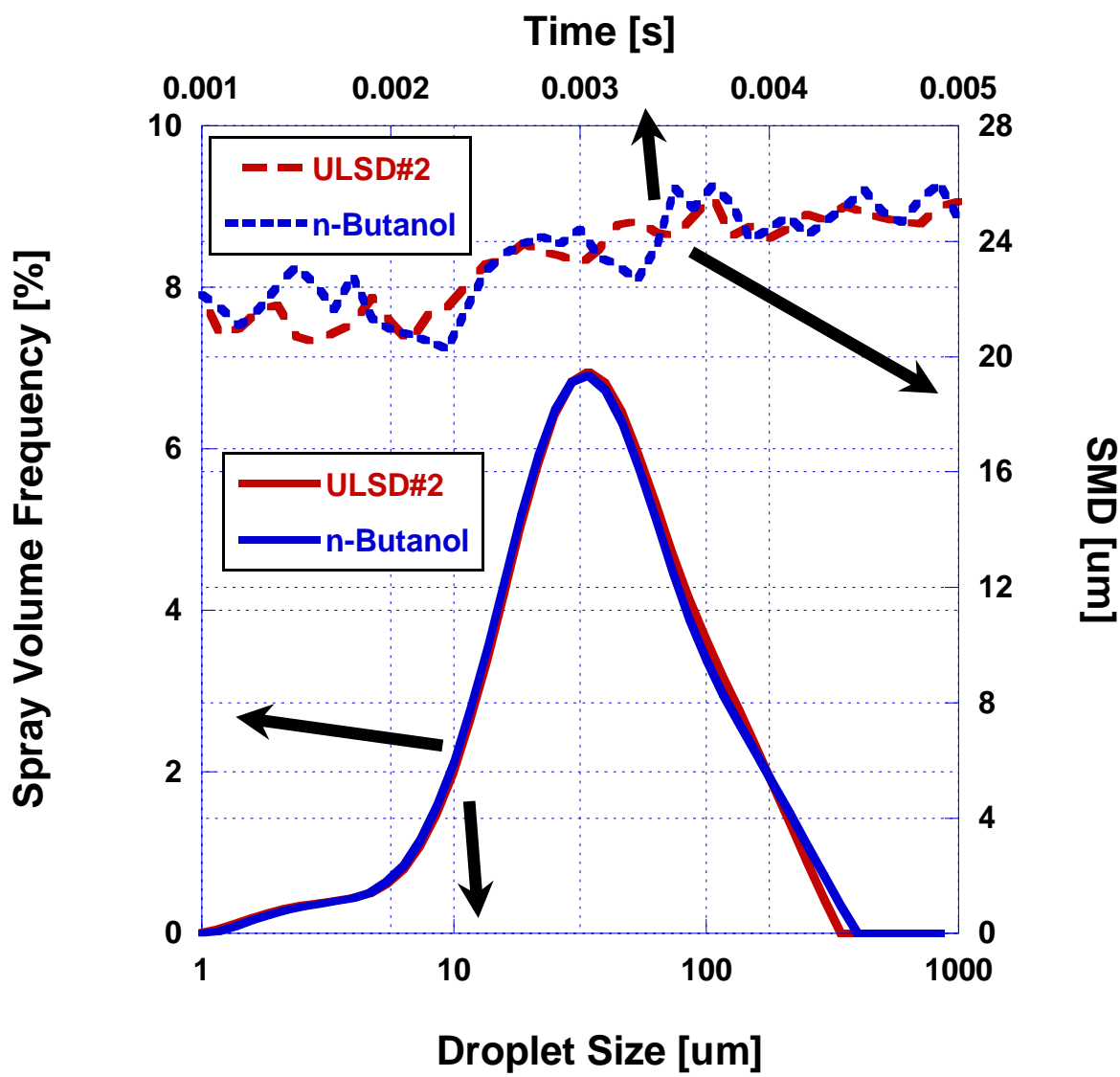


Figure 50 Sauter Mean Diameter and Droplet Frequency Distribution

Table XX: Particle Size Distribution by Volume (µm)

	Dv(10)	Dv(50)	Dv(90)	SMD	%v<10µm
ULSD	12.5	40.1	131.1	23.7	9.0
n-Butanol	12.4	39.5	136.7	23.9	9.1

## 4.2 Thermodynamic Combustion Analysis

### 4.2.1 Combustion Pressure

Direct measurement of the combustion pressure is possible by in-cylinder instrumentation of two Kistler Piezoelectric Pressure transducers. For the main chamber a Kistler 6053CC was used while a Kistler 6056A was used in the pre-chamber. The evaluation of the maximum combustion pressure for all fuel blends and injection regimes will be evaluated and compared to a reference fuel. Combustion pressure data will be averaged over approximately 100 cycles taken at intervals of 3-5 minutes. Proposed data will include the CAD at peak pressure and the magnitude of peak pressure along with a motoring curve to indicate the TDC of the engine. The combustion pressure will be pegged to an intake plenum at a particular CAD to ensure proper alignment. The figure below is sample data that was taken using cottonseed biodiesel injection strategies. Figure 51 displays the pressure traces for each fueling strategy. Conventional diesel combustion (CDC) saw similar peak compression at 63 bar to the 10% dual fuel strategy. After 10% a trend can be seen where cylinder pressure increases with the increasing concentration of n-butanol with a maximum pressure of 73 bar being observed at 40% dual fuel strategy. This correlates to the longer mixing time available to the butanol (Soloiu and Moncada<sup>B</sup> 2018). The location of the peak pressure can be seen to shift early in the cycle with the 40% dual fuel strategy reaching peak pressure 4° earlier than CDC. This correlates to the shorter ignition delay observed from the dual fuel strategies, which is a result of the increased oxygen content of the butanol causing a more rapid combustion. An inflection in the pressure trace can be seen just after TDC, due to the cooling effect of n-butanol (Soloiu and Gaubert 2018).

The maximum pressure rise rate (MPRR) can be seen in Figure 52. A steady increase in MPRR can be seen from CDC to the 30% dual fuel strategy showing an increase of 35%. By 40% injection of n-butanol a MPRR of 4.98 bar/degree is observed. This is a 127% increase over CDC which had a MPRR of 2.19 bar/degree. These increases are a result of smaller reactivity gradients at the time of combustion (Li 2015).

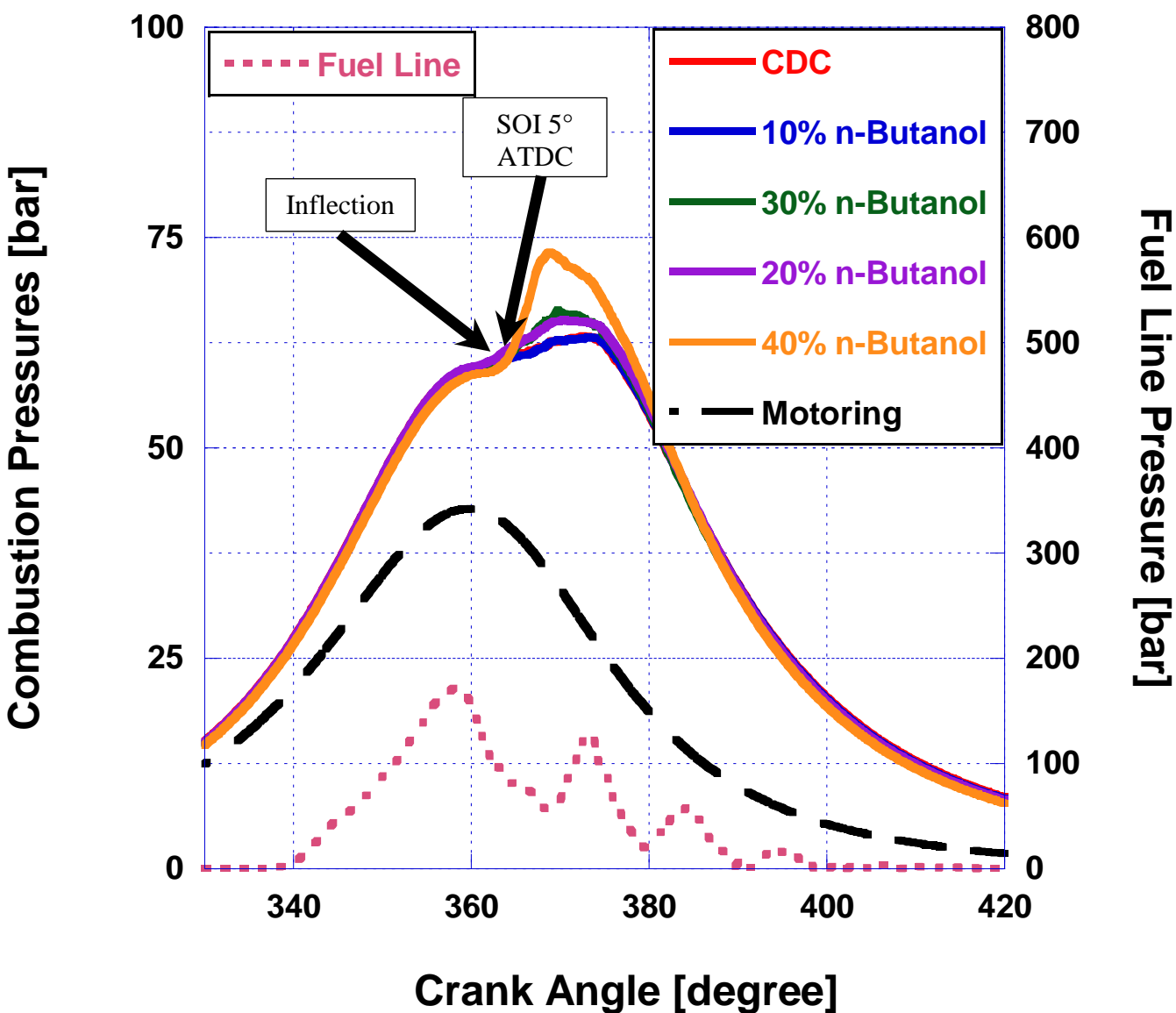
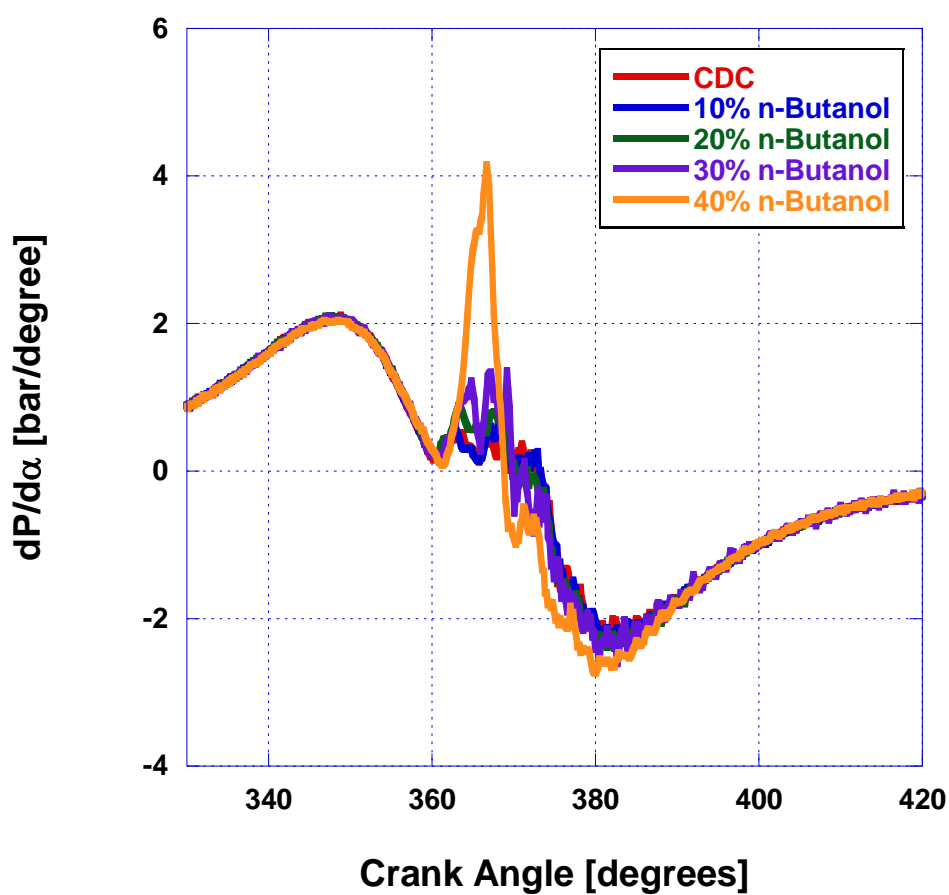


Figure 51 Maximum Combustion Pressure



**Table XXI:** Maximum Combustion Pressure and Respective Crank Angle

Fueling Strategy	Peak Pressure (bar)	Crank Angle
CDC	63.33	372.60°
10% n-Butanol	63.22	373.32°
20% n-Butanol	65.21	370.44°
30% n-Butanol	66.43	369.72°
40% n-Butanol	73.25	368.82°

**Figure 52** Maximum Pressure Rise Rate

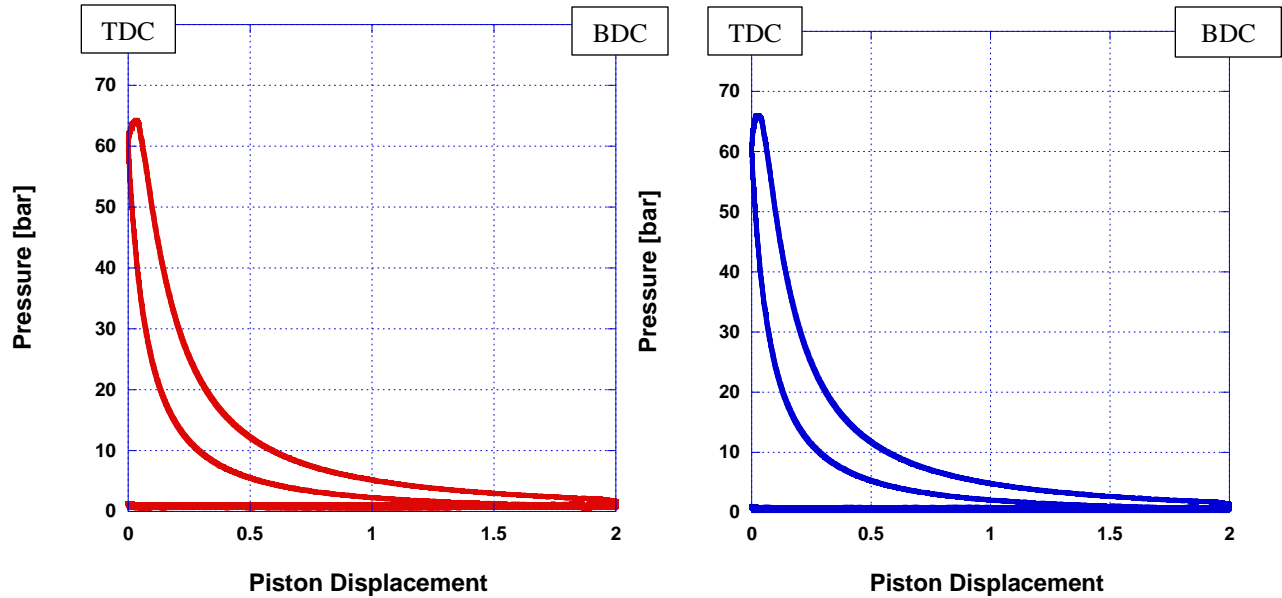


**Figure 53** P-V Diagrams for CDC (left) and 20% n-Butanol (right)

Figure 53 above displays the P-V diagrams for CDC and the 20% dual fuel strategy. The dual fuel mode has a peak pressure 2 bar higher than CDC giving it a narrower area under the compression and combustion areas of the curve.

#### 4.2.2 Apparent Heat Release

The net rate at which heat is absorbed and released is described as the apparent heat release. The work done on the piston and the heat transfer from the hot gasses to the cylinder walls must be accounted for to gain quantitative information about this process. We made the assumption that the system is closed, and the mass transfer of the injected fuel is omitted. Other assumptions were: the working fluid of the combustion chamber operates under the laws of ideal gas and the first law of thermodynamics. Crevice flow and blow by were ignored since it represents less than 2% of the system's mass. Equivalent substitutions were made where necessary. For analysis, Equation 13 below is used. Referencing the equation  $Q$  is in Joules,  $\Theta$  is crank angle degrees,  $\gamma$  is the specific heat capacity of air,  $V$  is the cylinder volume in liters, and  $P$  is combustion pressure in bar.

$$\frac{dQ}{d\theta} = \frac{1}{(\gamma-1)} V \frac{dP}{d\theta} + \frac{\gamma}{\gamma-1} P \frac{dv}{d\theta} \quad \text{Equation 13}$$

The figure below represents the apparent heat release rates (AHRR) for each fueling strategy. Values of peak heat release and the respective CAD can be seen in Table XX. In Figure 54 and Figure 55 below, the apparent heat release for each fueling strategy is presented. The apparent heat release reaches a maximum of approximately 21.45 J/degree for the CDC. From 10% to 30% dual fuel strategies a decrease in the AHRR can be seen. This is due to the lower energy content of the alcohol fuel. The 40% dual fuel strategy displays the maximum AHRR of almost 28 J/degrees. This is a 30% increase over what was observed for CDC. This deviation from the trend observed previously is a result of an increase in the premixed heat release from the n-butanol. This is visible as the first peak. The high latent heat of vaporization of both the n-butanol led to more prominent concave minimums in the dual fuel strategies (Soloiu and Gaubert 2018).

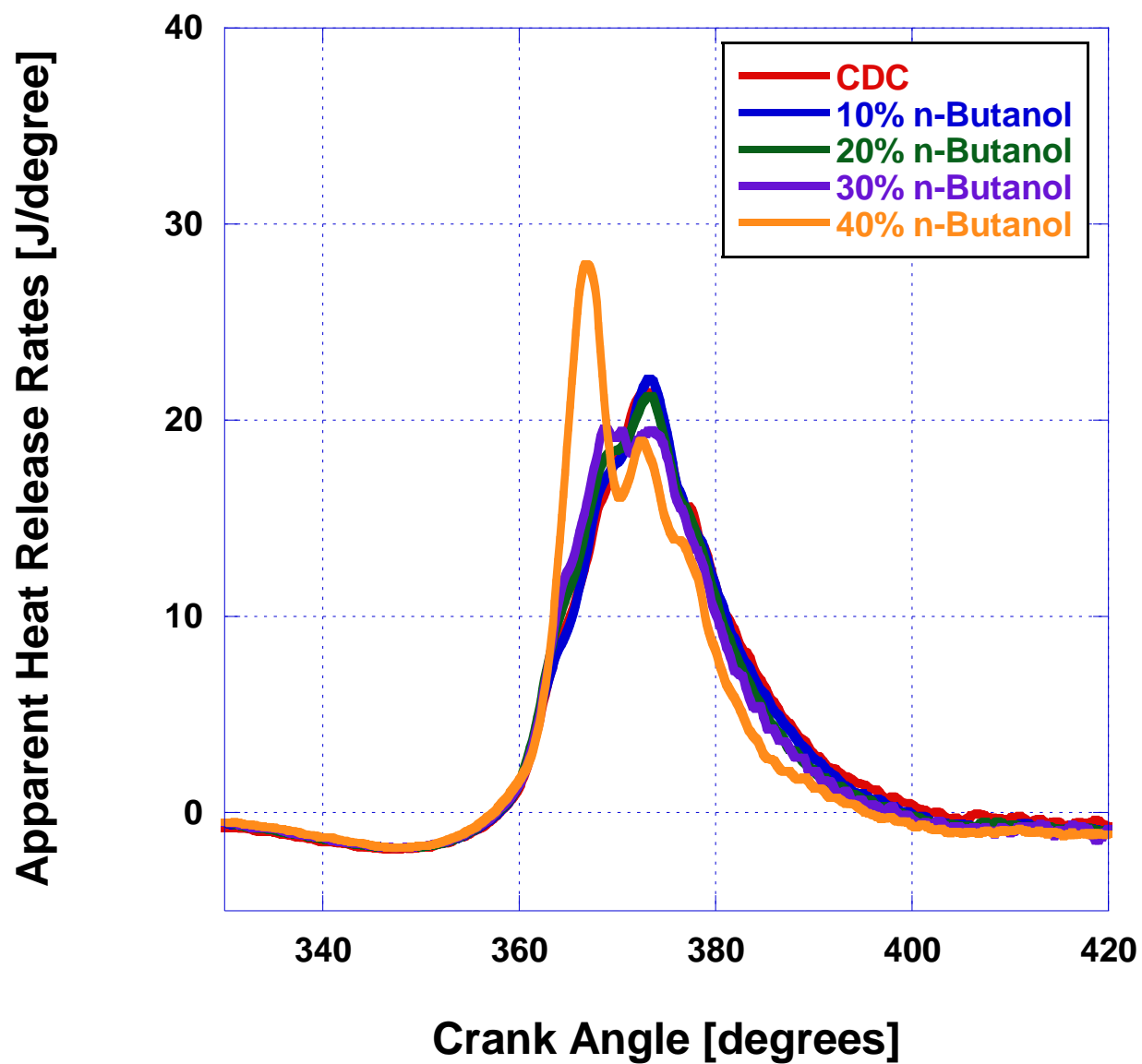


Figure 54 Apparent Heat Release Rate

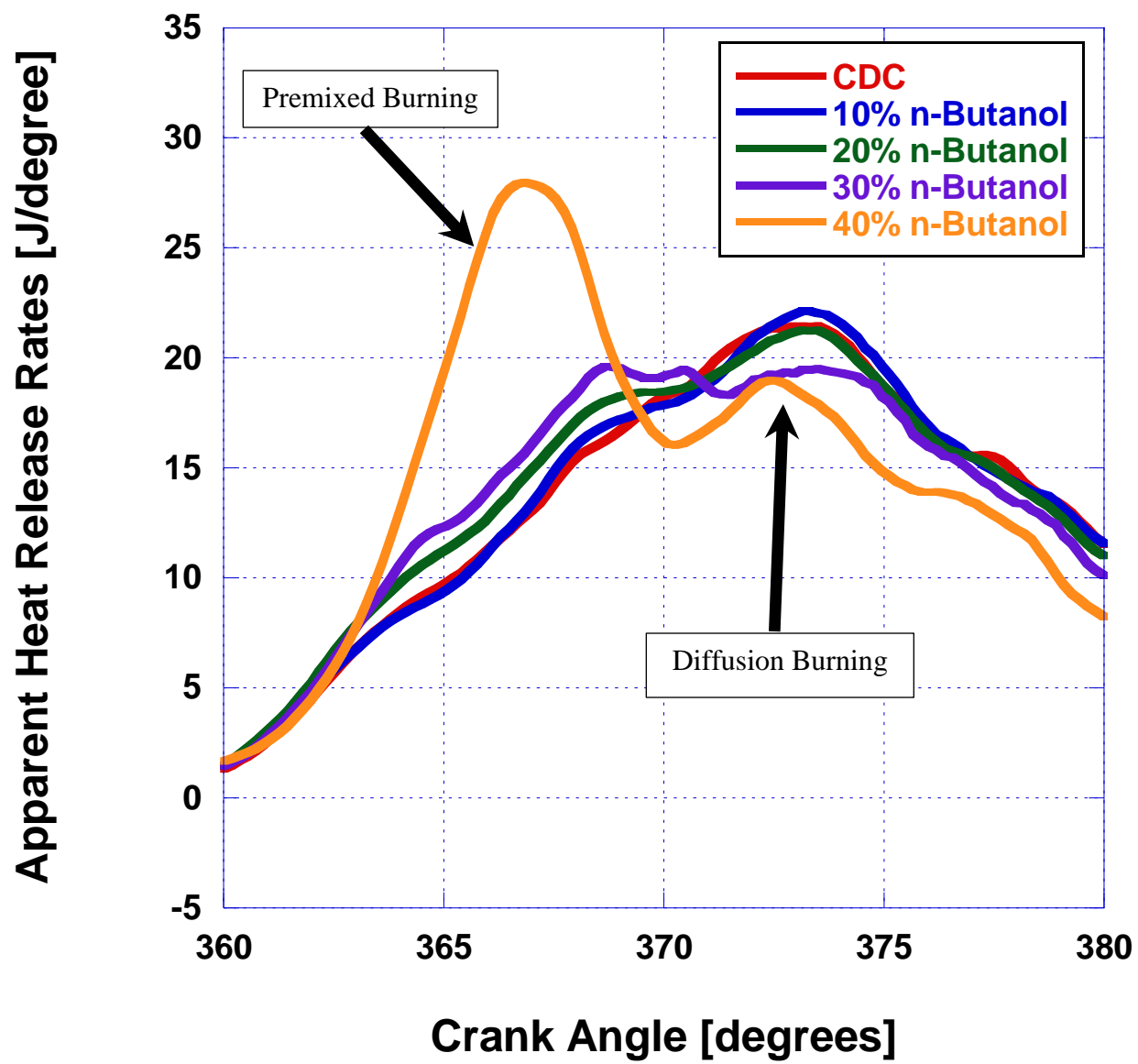


Figure 55 Apparent Heat Release Rate- Detail of Figure 54

**Table XXII:** Maximum Apparent Heat Release Rate and Respective CAD

<b>Fueling Strategy</b>	<b>Peak Heat Release Rate (J/degree)</b>	<b>Crank Angle</b>
<b>CDC</b>	21.45	373.50°
<b>10% n-Butanol</b>	22.13	373.14°
<b>20% n-Butanol</b>	21.26	373.14°
<b>30% n-Butanol</b>	19.60	368.82°
<b>40% n-Butanol</b>	27.99	366.84°

#### 4.2.3 Mass Fraction Burned

Mass fraction burned is a cumulative characteristic of heat release, specifically the integration of gross heat release plotted against the CAD. It gives insight to the burning rate of the fuel where CA10, CA50, and CA90 are representative of 10%, 50%, and 90% of the mass of the fuel being consumed. In Figure 56 below, the mass fraction burned for each fueling strategy is presented. Ignition delay and combustion duration can be analyzed from this data. Ignition delay as defined above is the time from the start of injection to CA10, while the combustion duration is the time from CA10 to CA90. The test fuels behave similarly due to the engines high temperature & high vortex auxiliary chamber. The overlap of the mass fraction burned is a good indication of the engines ability to burn various fuels. This is shown by CA50 for each fueling strategy which falls within  $375^{\circ} \pm 2^{\circ}$  with respect to the crank angle. A decrease in both ignition delay and combustion duration can be seen as the concentration of n-butanol being injected increases. This contradicts what would be expected given the alcohol based fuel's lower cetane number when compared to neat ULSD#2. This is a result of both the chemical and physical properties of the fuel as well as the injection strategy. The volatility of n-butanol as observed by the thermogravimetric

analysis, combined with its' lower viscosity promoted increased atomization and evaporation. When combined with the increased mixing time obtained by injecting into the intake manifold a more premixed charge is introduced into the combustion chamber allowing for the shorter ignition delay and faster rate of combustion (Soloiu and Gaubert 2018). Overall a 12.5% decrease in ignition delay and a 31.6% decrease in combustion duration was observed between CDC and the 40% dual fuel strategy.

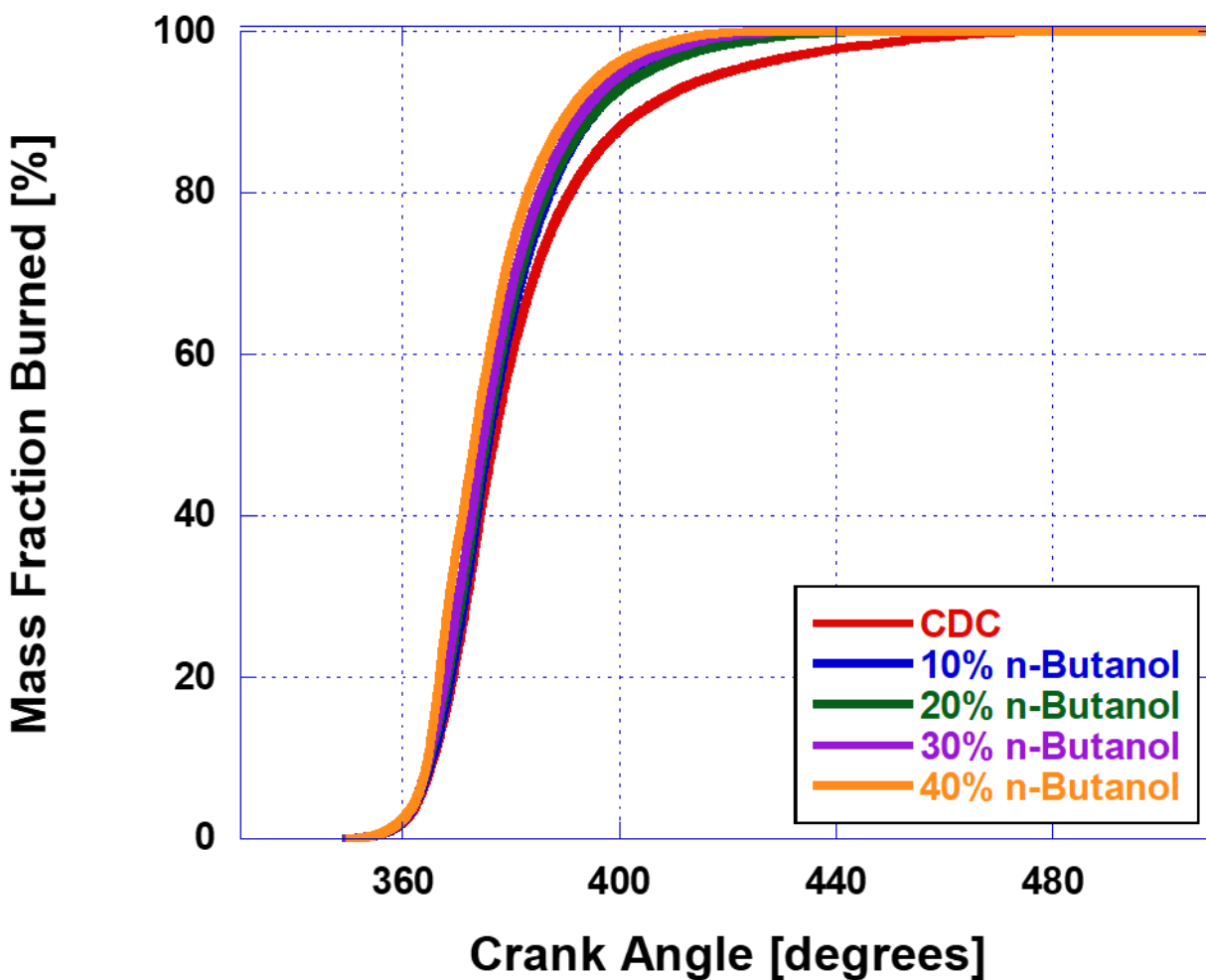


Figure 56 Mass Fraction Burned

**Table XXIII: Mass Fraction Burned**

	<b>CDC</b>	<b>10% n-Butanol</b>	<b>20% n-Butanol</b>	<b>30% n-Butanol</b>	<b>40% n-Butanol</b>
<b>CA10</b>	365.76°	365.40°	365.04°	364.86°	364.68°
<b>CA50</b>	377.10°	376.02°	375.48°	375.12°	373.50°
<b>CA90</b>	403.92°	395.64°	395.46°	393.30°	390.78°

**Table XXIV: Combustion Duration**

	<b>CDC</b>	<b>10% n-Butanol</b>	<b>20% n-Butanol</b>	<b>30% n-Butanol</b>	<b>40% n-Butanol</b>
<b>Ignition Delay</b>	14.4°/ 1 ms	13.68°/ 0.95 ms	13.14°/ 0.93 ms	12.24°/ 0.85 ms	12.6°/ 0.88 ms
<b>Combustion Duration</b>	38.16°/ 2.65 ms	30.24°/ 2.10 ms	30.42°/ 2.11 ms	28.44°/ 1.98 ms	26.10°/ 1.81 ms

#### *4.2.4 Instantaneous Volume Averaged Maximum Gas Temperature*

To maintain the integrity of the engine, a vital parameter to consider is instantaneous volume averaged maximum gas temperature. If the maximum temperature inside the cylinder becomes too high and the oil film is negatively affected, then the reliability and lifespan of the engine will be compromised. The max gas temperature also directly correlates to the amount of NO<sub>x</sub> and soot emissions produced. Higher concentrations of NO<sub>x</sub> occur as a result of a higher maximum temperature. Soot had an inverse relationship. It decreases with increasing temperature and pressure.

In the ideal diesel cycle during the compression stroke the pressure in the cylinder increases, which correlates to an increase in temperature. The high compression ratio of the diesel engine causes the temperature of the combustion chamber to be above that of the ignition point. In order to accurately calculate the maximum gas temperature a zero dimensional model was used and the contents of the cylinder are considered homogeneous and operate under the ideal gas law.



Figure 57 below presents the instantaneous volume averaged maximum gas temperature for all fueling strategies. Maximum temperatures range from a minimum of 1760 K observed in the 30% dual fuel strategy to a maximum of 1794 K observed in the 40% dual fuel strategy. This is a 1.9% difference. This consistency is a result of the extensive premixing from both the use of an auxiliary combustion chamber as well as the port fuel injection. The rapid inflections in temperature correlate to the delays in premixed combustion (Soloiu and Moncada<sup>B</sup> 2018).

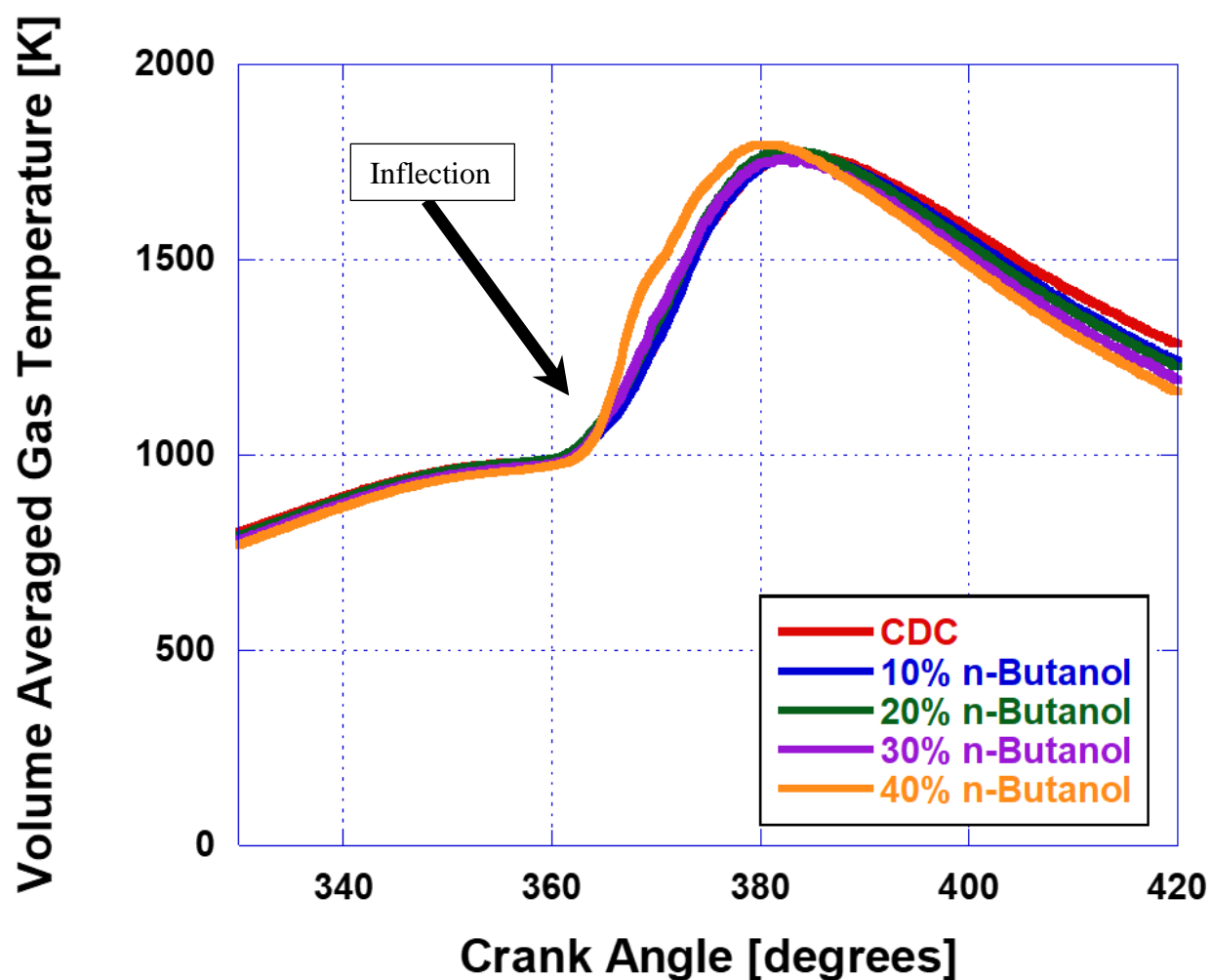


**Figure 57** Instantaneous Volume Averaged Maximum Gas Temperature

#### 4.2.5 Ringing Intensity

Fuel properties, mixture composition and heat release rates will all influence the rate of pressure rise in cylinder. The magnitude of pressure waves will impact the life of an engine as well as the noise it produces. Gaseous pollution is a prominent concern when it comes to IC engines. *Noise pollution is also a concern due to the higher compression ratios and autoignition behavior of CI engines.* Ringing Intensity (RI) was calculated using Equation 14. A value of 0.05 was used for  $\beta$ , which is a constant that relates pressure rise rate and pulsation amplitude (J.A. Eng 2002).

$$RI = \frac{\left(\beta \left(\frac{dP}{dt}\right)_{max}\right)^2}{2\gamma P_{max}} \sqrt{\gamma R T_{max}} \quad \text{Equation 14}$$

Ringling intensity for all fueling strategies are displayed in Figure 58. *RI increased with the mass flow rate of n-butanol.* The 40% dual fuel strategy had the highest RI at 5.66 MW/m<sup>2</sup>. This was 220% higher than conventional diesel combustion. CDC had the lowest RI at 1.77 MW/m<sup>2</sup>. The influence of the maximum gas temperature can be considered negligible due to the narrow range in which they fell. The biggest influences on the RI of each strategy would therefore be the maximum pressure release rates. The 40% dual fuel strategy had the highest RI intensity due the MPRR being 127% higher than that of CDC.

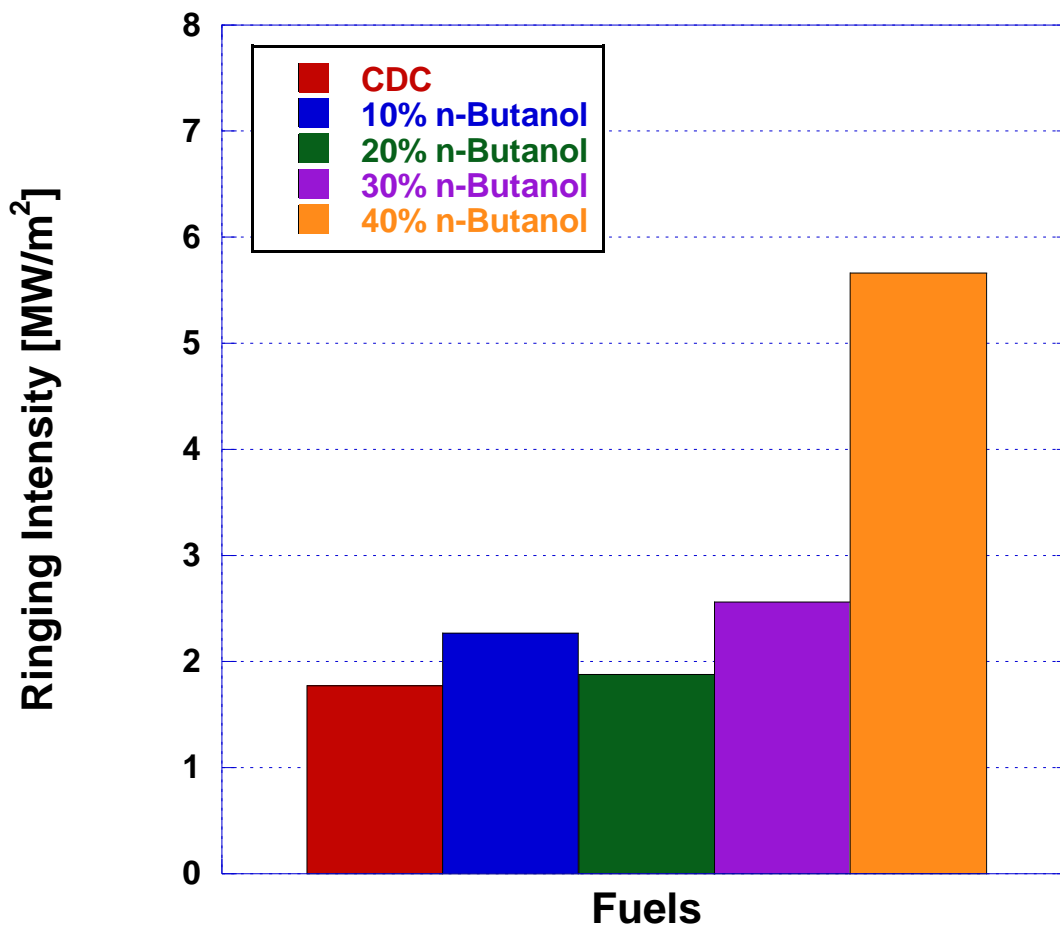


**Figure 58** Ringing Intensity

#### 4.2.6 Cylinder Heat Fluxes and Heat Transfer

Evaluation of the heat fluxes is necessary to evaluate the heat transfer. The models used are based off the work of Borman and Nishiwaki (1987) and were further developed by Soloiu (Soloiu 2012). To evaluate the heat fluxes the in-cylinder Reynolds number must be calculated. Equation 15 below is used to calculate instantaneous volume-averaged in-cylinder Reynolds number.

$$Re(\alpha) = \rho(\alpha) \frac{S \cdot N \cdot D}{30 \cdot \mu(\alpha)} \quad \text{Equation 15}$$

Where  $\rho$  is the density of in-cylinder gas,  $S$  is the engine stroke,  $N$  is the engine speed,  $D$  the piston diameter, and  $\mu$  is the air viscosity. Equation 16 below was used for the calculation of the air viscosity.

$$\mu(\alpha) = 4.94 \cdot \frac{1273.15 + 110.4}{T_A(\alpha) + 110.4} \cdot \left( \frac{T_A(\alpha)}{1273.5} \right)^{1.5} - 10^{-5} \quad \text{Equation 16}$$

$T_A$  is the cylinder gas temperature at each increment of  $0.18^\circ\text{CAD}$ . For the convection flux,  $\sigma$  is the Stefan-Boltzmann constant, while the emissivity factor  $\varepsilon$  was considered for the smoothed walls of the combustion chamber.

$$\dot{q}(\alpha) = A \frac{\lambda_A(\alpha)}{D} Re(\alpha)^{0.7} (T_A(\alpha) - T_w) + \sigma \cdot \varepsilon (T_A^4(\alpha) - T_w^4) \quad \text{Equation 17}$$

The air conductivity is calculated using the following formula.

$$\lambda_A(\alpha) = -1.2775 \cdot 10^{-8} \cdot T_A(\alpha) + 7.66696 \cdot 10^{-5} \cdot T_A(\alpha) + 0.00444888 \quad \text{Equation 18}$$

Due to the triple vortex separate combustion chamber, the conditions inside the combustion chamber reach a Reynolds numbers well above 100,000 which is considered highly turbulent. The Reynolds numbers varied with CDC having the lowest and the 30% dual fuel strategy having the highest. The magnitude and crank angle locations of the radiation, convection, and total heat fluxes are visible in Figure 59. Shown in the figure, the total heat fluxes are relatively similar for CDC up to 30% port fuel injection of n-butanol. The 40% dual fuel strategy had the highest fluxes and deviated from the other strategies. This correlates to the higher AHRR observed. The total flux (solid line) is a combination of the convection and radiation heat fluxes (dashed lines). The primary source of heat transfer comes from the forced convection from the bulk gas to the cylinder walls as seen in Figure 58.

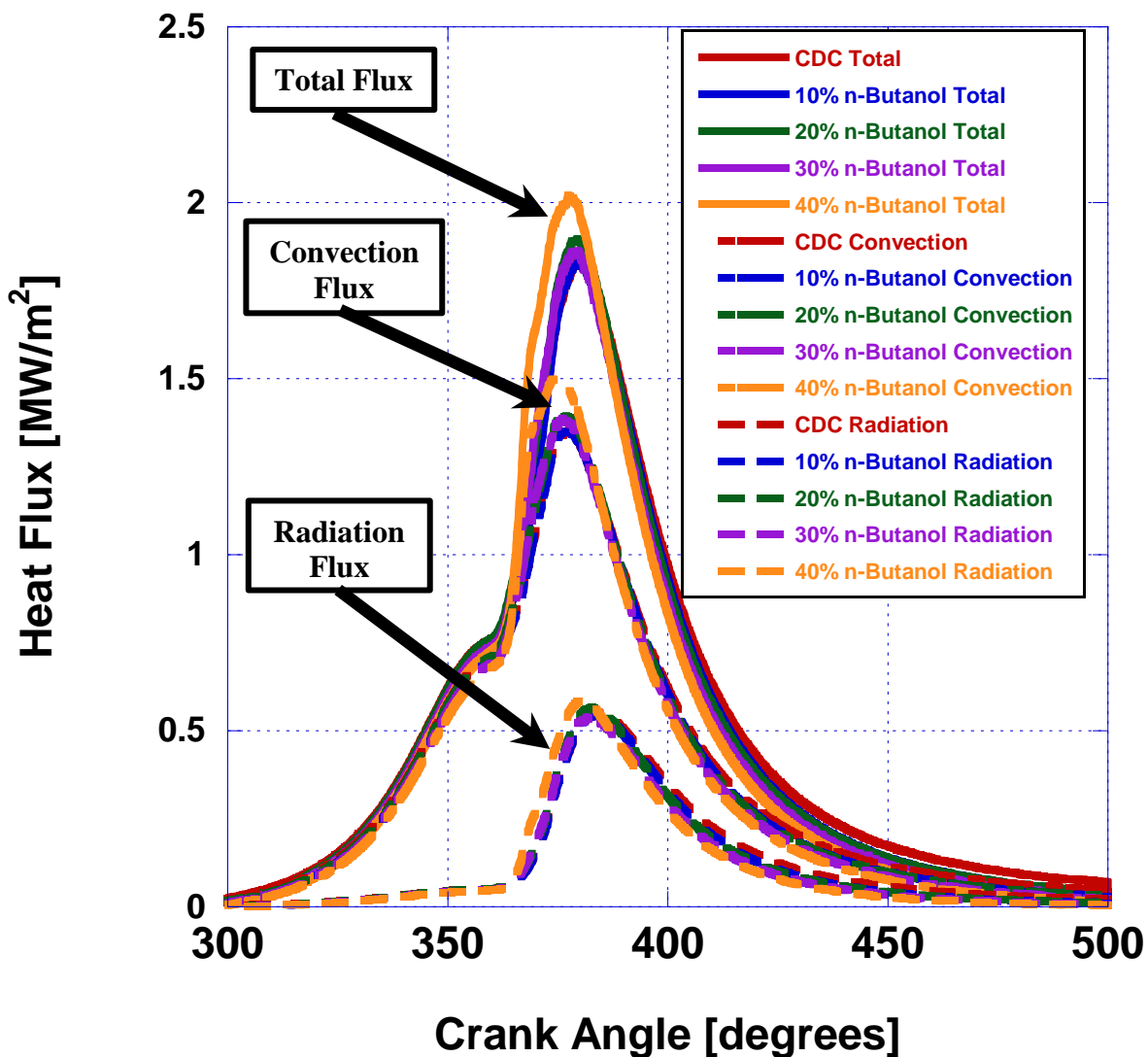


**Figure 59** Heat Fluxes

The heat losses in the cylinder are based on the heat fluxes and the apparent heat release calculated in previous sections. Figure 60 and Figure 61 below show the losses throughout the cycle for CDC and 40% n-butanol dual fuel strategy respectively. The heat losses described as convection is shown as the blue area on each plot. The radiation heat losses are represented by the green area, between the blue line and red gross heat release line. The heat losses for all fuels across all loads are very similar with the heat losses due to convection being larger in every case. The

heat losses at TDC are minimal and begin to grow with the expansion of the gasses and the increase in combustion chamber volume. The presence of n-butanol affected the local droplet temperatures and vapor pressures due to the higher vaporization rate, increasing convection fluxes. The radiation flux followed the in-cylinder temperature curve (Soloiu and Gaubert 2018). Combustion efficiency was higher at 100% at 450° crank angle for the 40% fueling strategy due to the shorter combustion duration experienced.

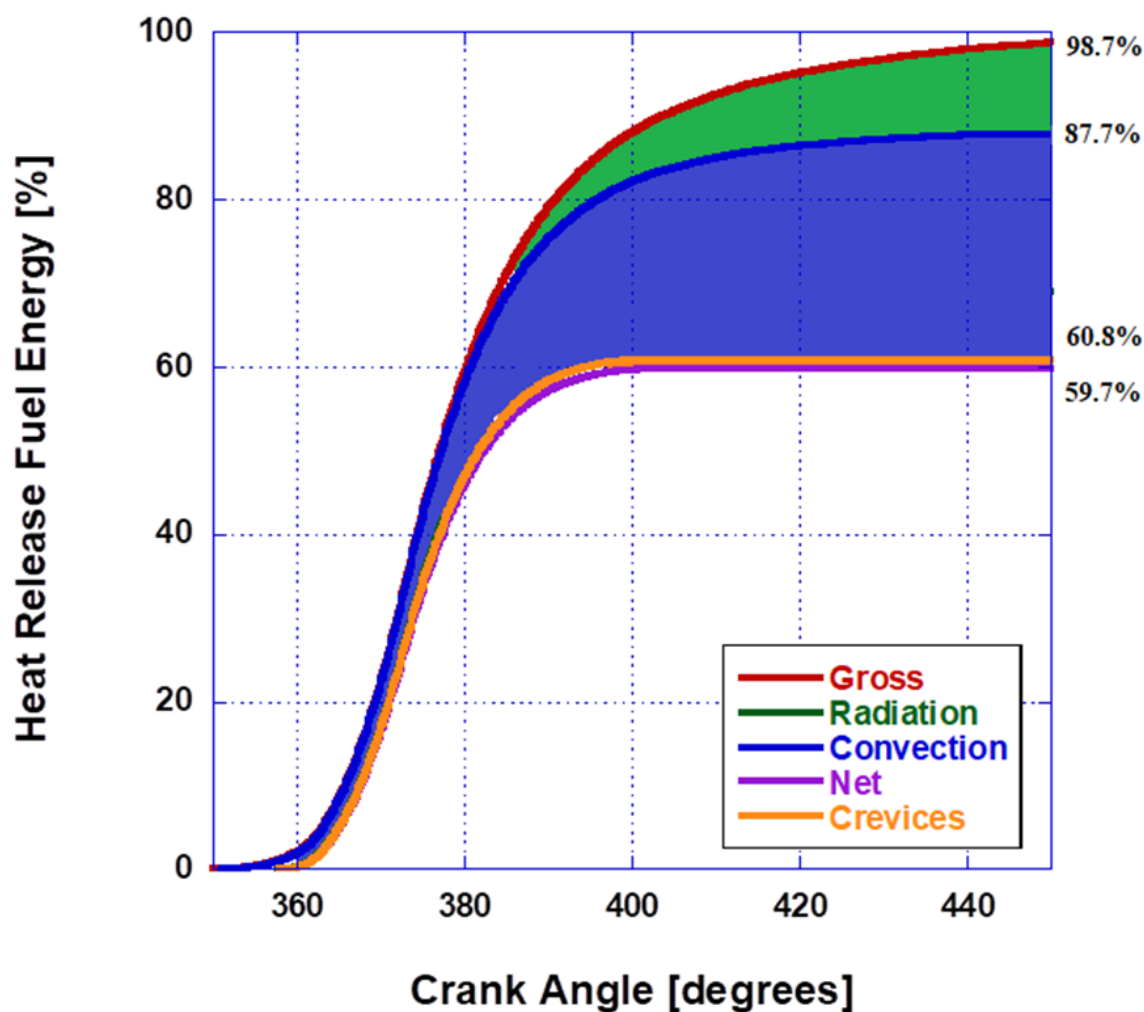


**Figure 60** Heat Losses for Conventional Diesel Combustion

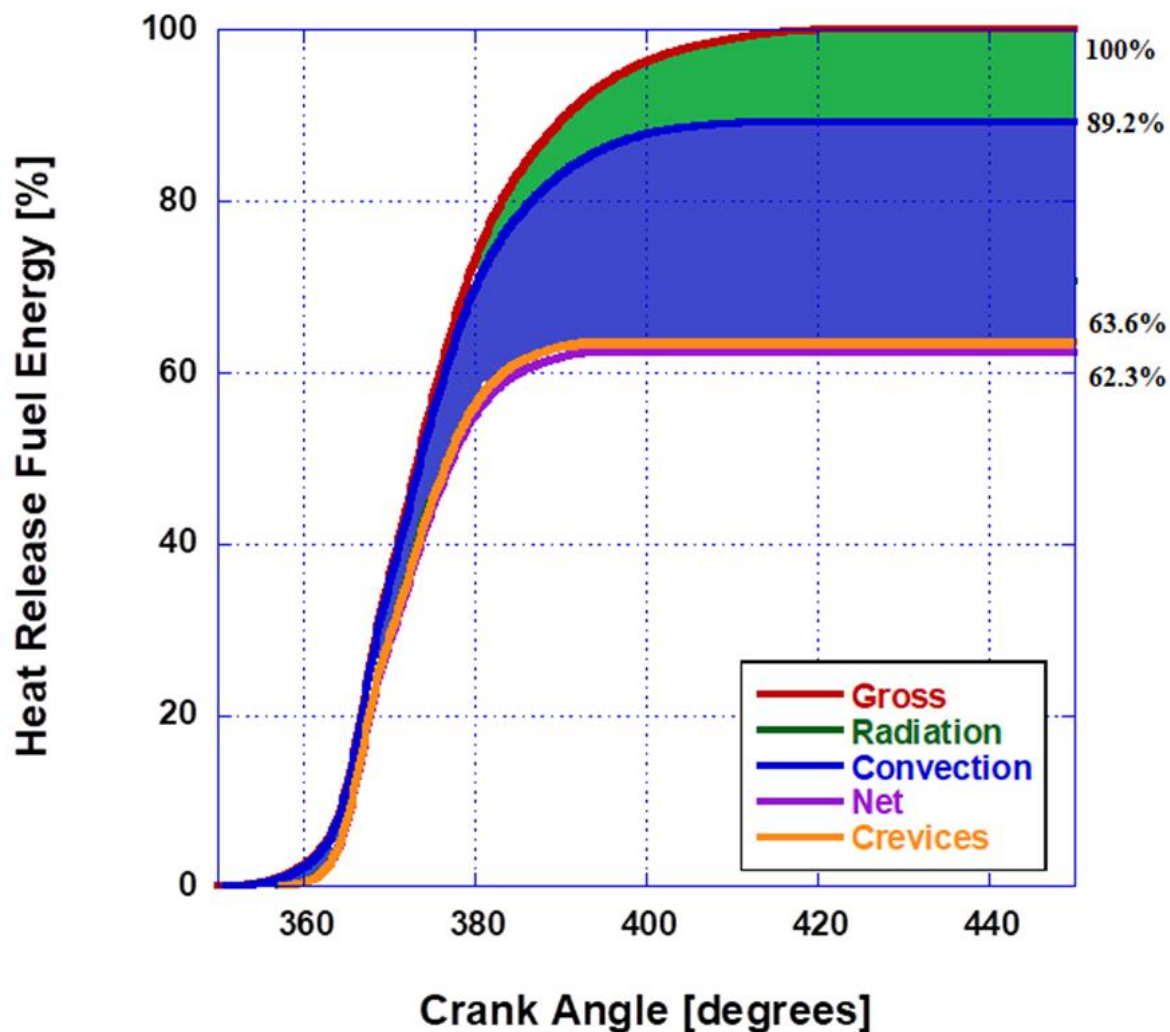


**Figure 61** Heat Losses for Dual Fuel Combustion at 40% of the Total Fuel Mass Flow Rate

#### 4.3 Emissions and Efficiencies Investigation

##### 4.3.1 Nitrogen Oxides and Soot

The main goal of this study was to reduce the emissions produced from combustion by controlling the reactivity of the air/fuel charge through the use of dual fuel combustion. The emissions data is collected and analyzed based on a reference measurement of conventional diesel combustion at the same speed and load. Data is converted to the mass in grams of the select

emission per kilowatt-hour. Shown in Figure 62 below the concentrations of NO<sub>x</sub> emissions are plotted based on concentration of n-butanol. A decrease in NO<sub>x</sub> was observed from CDC to the 30% dual fuel strategy. This was a reduction from a maximum of 3.0 g/kWh to a minimum of 2.4 g/kWh which is a 20% reduction. The 40% dual fuel strategy increased from the 30% strategy by 8%. The decrease in NO<sub>x</sub> emissions was a result of the cooling effect of the alcohol based fuel caused by its' higher latent heat of vaporization.

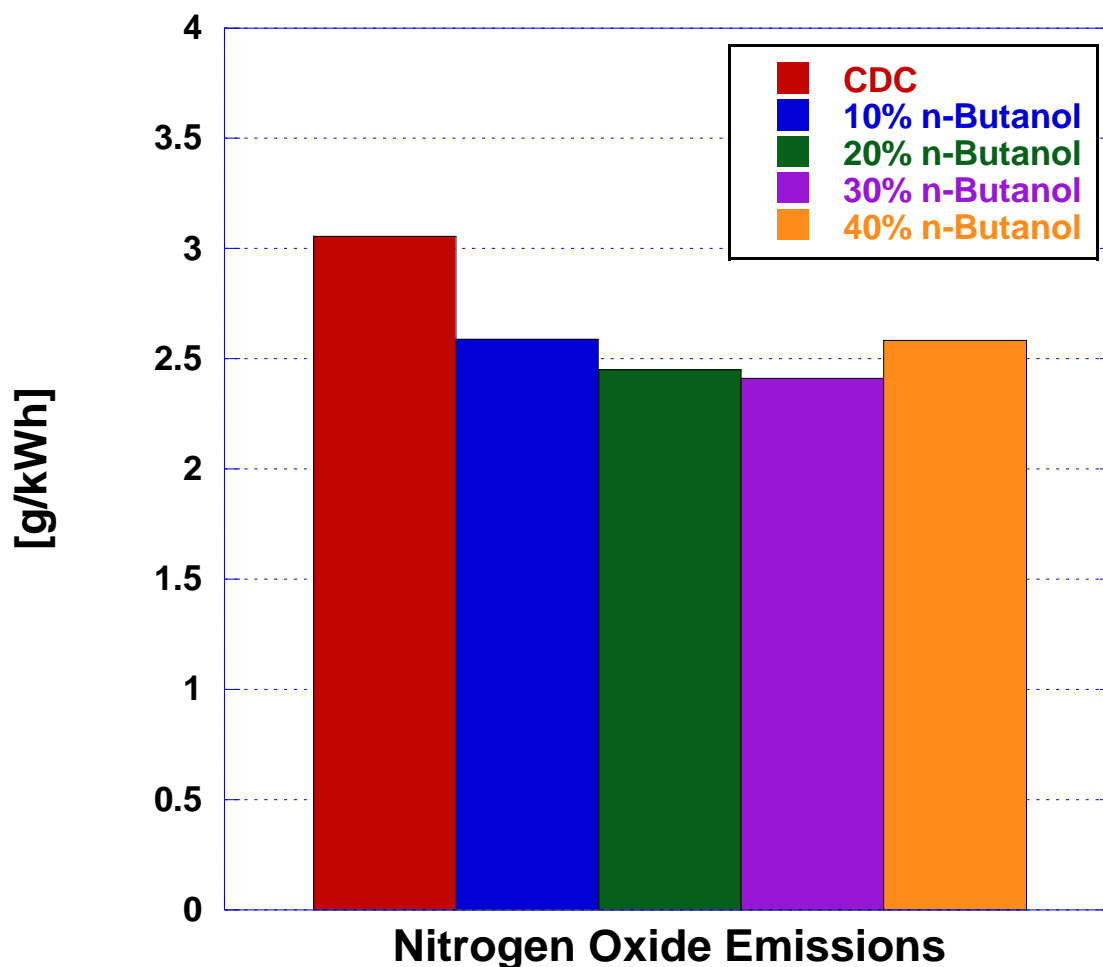


**Figure 62** Nitrogen Oxide Emissions for increasing n-Butanol Concentrations



The port fuel injection of n-butanol resulted in a homogeneous air/fuel mixture prior to ignition, resulting in much lower levels compared to CDC. The slight change in trend for n-butanol blends can be related to some increases seen in AHRR, specifically the 40% dual fuel strategy which lead to the increase in NO<sub>x</sub> observed (Soloiu and Gaubert 2018).

Soot emissions are shown in Figure 63. A steady decrease in soot can be seen as the concentration of n-butanol increases. CDC has the highest concentration of soot at 0.37 g/kWh. The 30% dual fuel strategy had the lowest concentration of soot at 0.073 g/kWh. The 40% fueling strategy was marginally higher at 0.074 g/kWh. Between the 30% dual fuel strategy and CDC a reduction of soot of 80% was observed. Port fuel injection allowed for in-cylinder mixing which created a more homogenous mixture, reducing fuel rich areas across the chamber. The higher oxygen content of n-butanol allowed a more complete combustion by enhancing soot oxidation (Soloiu and Gaubert 2018). This also happens as a result of butanol's high volatility which increased mixing rates and carbon recession rates (Amann et al 1980).

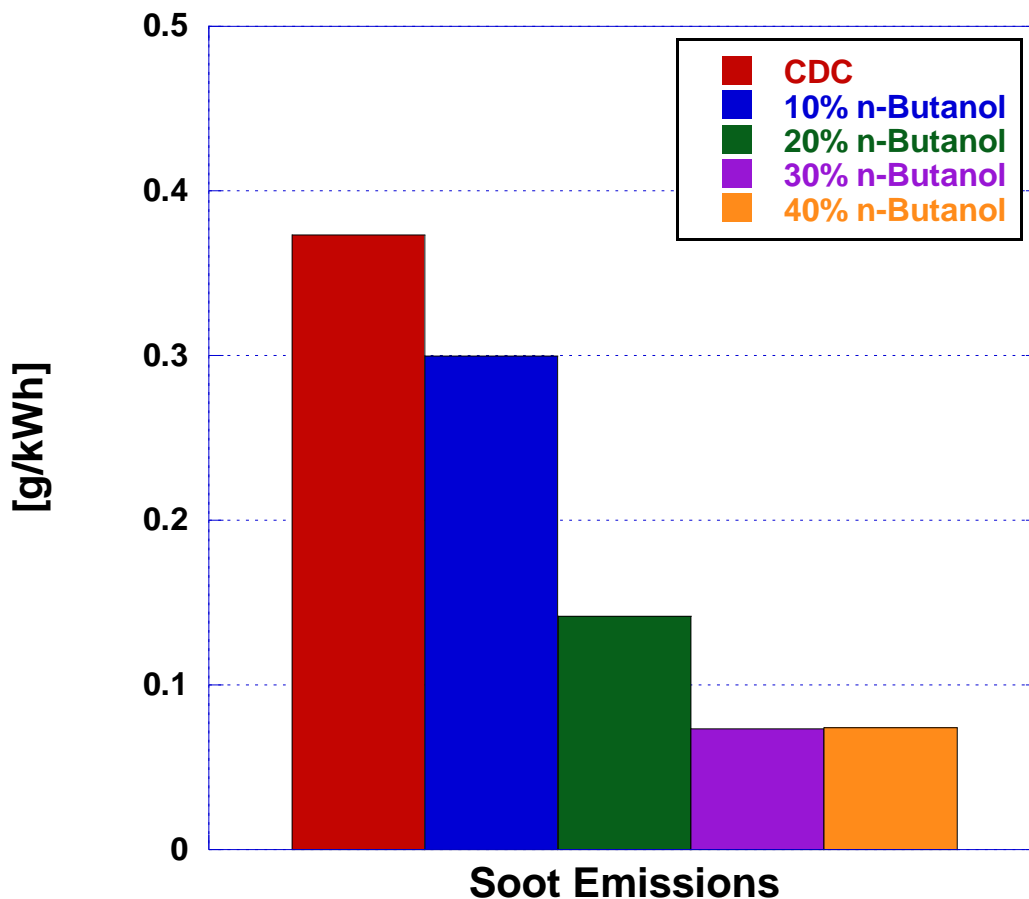
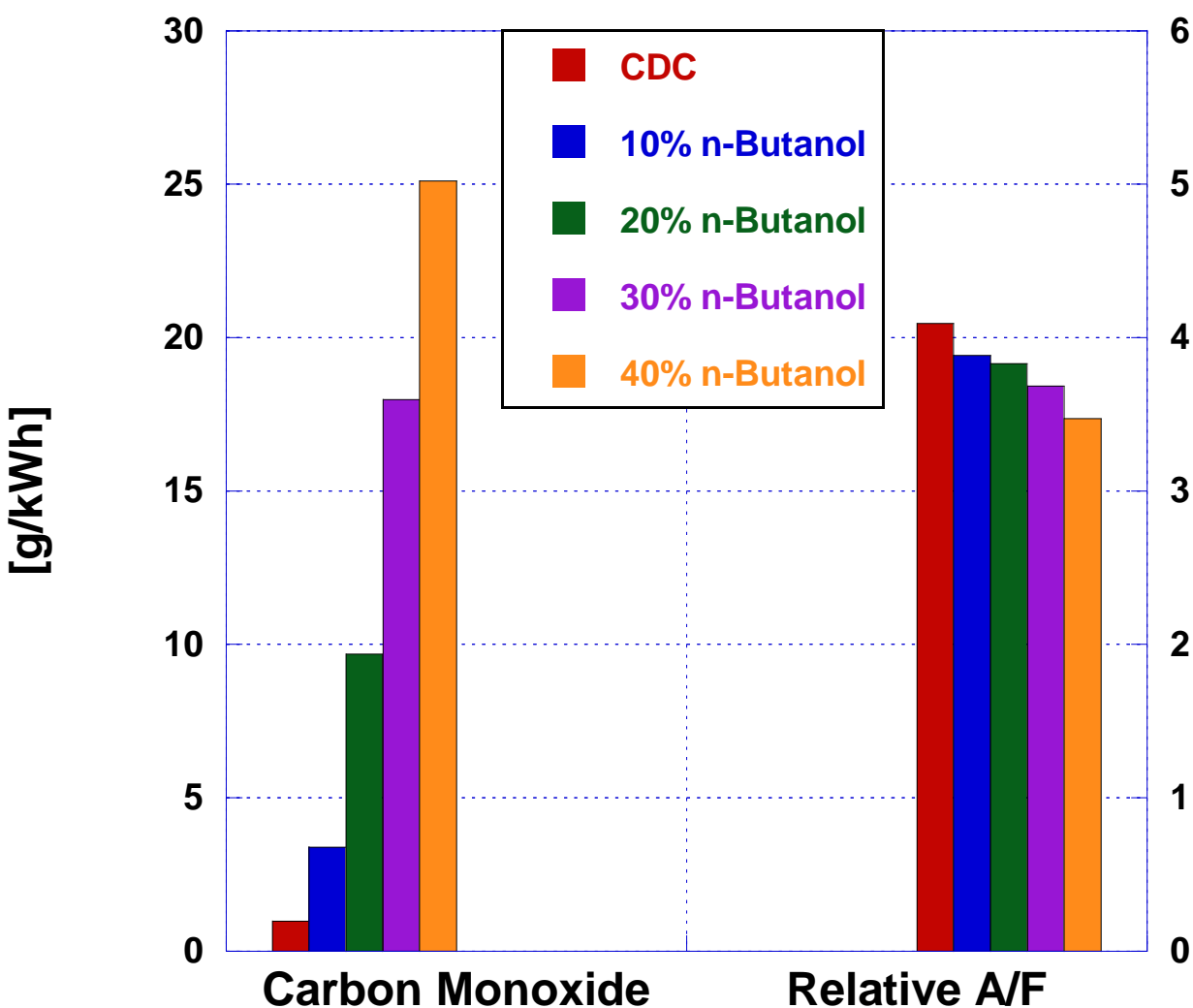


**Figure 63** Soot Emissions for increasing n-Butanol Concentrations

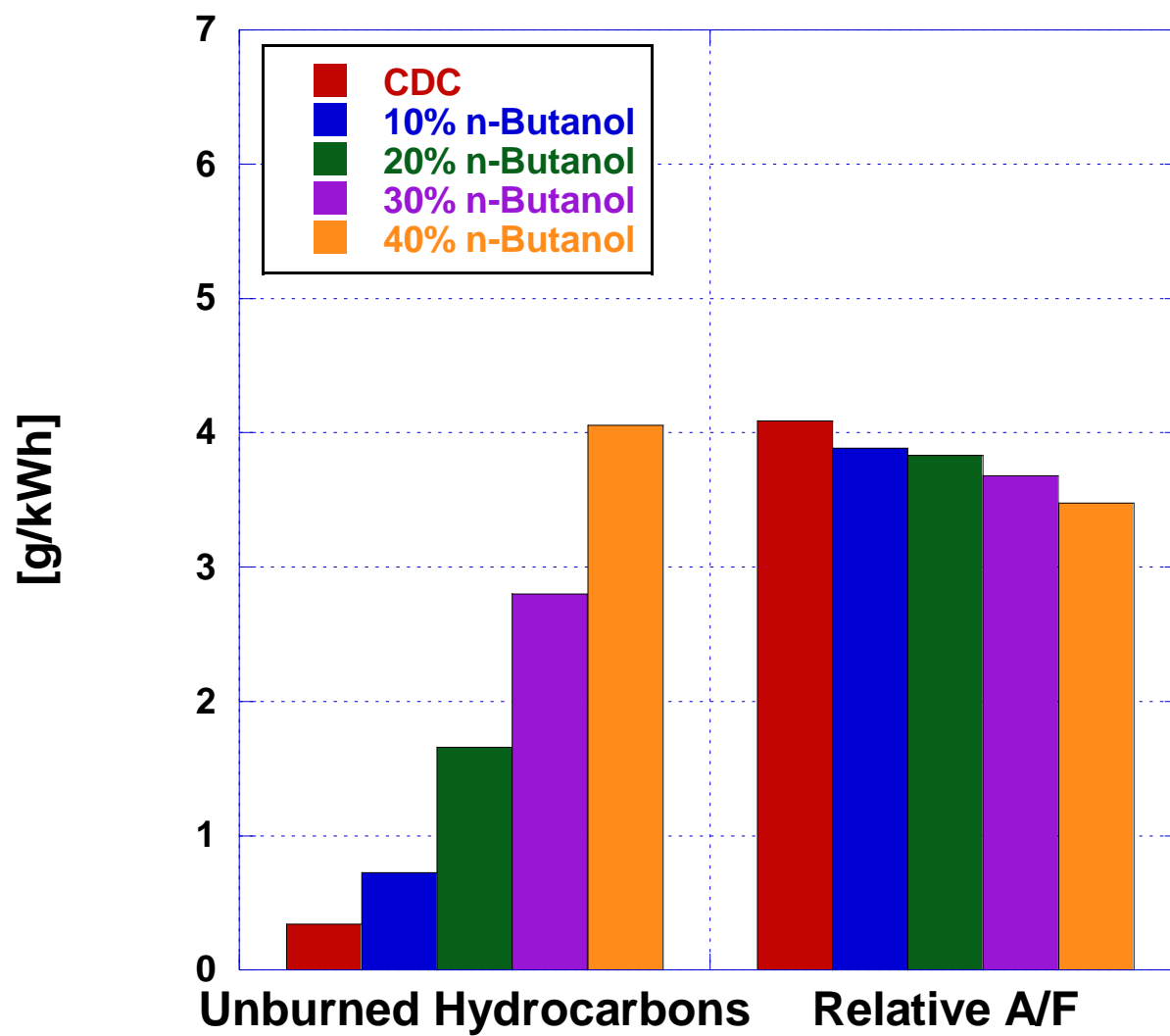
#### 4.3.2 Carbon Monoxide and Unburned Hydrocarbons

Figure 64 and Figure 66 display the carbon monoxide CO emissions and unburned hydrocarbon UHC emissions for each fueling strategy. Both CO and UHC emissions increased with n-butanol concentration. CO emissions increased from 0.98 g/kWh for CDC to 25.1 g/kWh for the 40% dual fuel strategy. This is a 2461% increase. This results from CO being unable to fully oxidize because of the decreased combustion duration and the increase in the total amount of fuel present at the time of combustion (Soloiu and Gaubert 2018). This correlates to the

decrease in the relative air/fuel ratio visible in Figure 65. UHC emissions weren't as drastic with a 1091% increase from CDC to the 40% dual fuel strategy. This is a result of butanol passing straight through the cylinder during valve overlap as well as the decreased air fuel ratio causing a lower combustion efficiency. Increases in CO and UHC can also be attributed to over mixing (Soloiu and Moncada<sup>B</sup> 2018).



**Figure 64** Carbon Monoxide Emissions for increasing n-Butanol Concentrations



**Figure 65** Unburned Hydrocarbons Emissions for increasing n-Butanol Concentrations

### 4.3.3 Aldehyde Emissions

Aldehyde emissions are shown in Figure 67. The aldehyde emissions recorded were for formaldehyde only. Dual fuel combustion increases formaldehyde emissions due to the combustion of the oxygenated alcohol. This is confirmed by the observed trend. As n-butanol concentration increases so does the aldehyde emissions. The increase in aldehyde emissions contributes to the increase in convection heat losses due to a quenching effect (CIMAC WG 17).

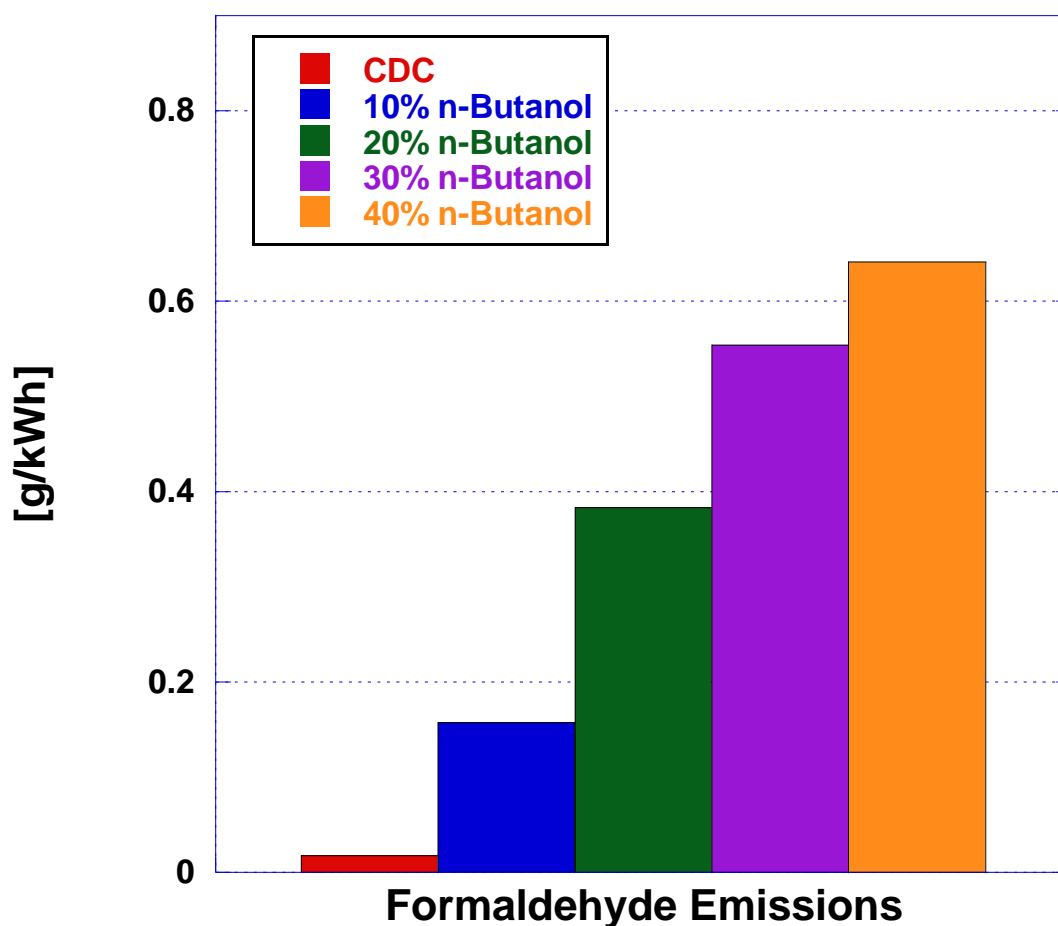


**Figure 66** Formaldehyde Emissions for increasing n-Butanol Concentrations

#### 4.3.4 *Efficiencies and Specific Fuel Consumption*

The efficiency of the engine is a vital parameter to knowing whether or not the injection strategy is viable. Mechanical and indicated thermal efficiencies (ITE) give an indication to how the engine is operating.

The efficiencies of the investigation are presented in Figure 68 below. Mechanical efficiency is defined as the ratio of BMEP to IMEP. Indicated thermal efficiency is the ratio of indicated power to fuel energy. Mechanical efficiencies were higher for the alcohol fumigation strategies. This was a result of the higher cylinder pressures observed as well as negating parasitic losses due to the external injection pump for the n-butanol. The maximum mechanical efficiency was 58% for the 30% dual fuel strategy, while the minimum was 56% for CDC. A trend should be observed with the mechanical efficiency increasing with increasing cylinder pressure. This trend holds true to the up to the 30% dual fuel strategy. The 40% dual fuel strategy breaks the trend. This is due to the earlier onset of combustion decreasing the amount of energy released during the expansion stroke as well as the higher heat transfer observed (Soloiu and Gaubert 2018). Indicated thermal efficiencies decreased with increasing n-butanol fumigation. CDC had the highest ITE at 43% and dropped to the lowest at 37.8% for the 40% dual fuel strategy. This occurred because the total fuel energy increased with the increasing n-butanol concentration, while the indicate power remained consistent for all fueling strategies at 3.4 kW.

The diesel equivalent brake specific fuel consumption (BSFC) was selected instead of the standard brake specific fuel consumption (BSFC) to account for the decrease in flow through the primary injector caused by the secondary injection source. Equation 19 below was used to calculate the Diesel equivalent BSFC (Xing-cai et al 2004).

$$\text{Diesel Equivalent BSFC} = \text{BSFC} \times \frac{\text{LHV}_{\text{Blend}}}{\text{LHV}_{\text{ULSD}}} \quad \text{Equation 19}$$

Figure 69 below presents the diesel equivalent BSFC for all fueling strategies. A linear increase was seen from CDC to the 40% dual fuel strategy. CDC had a BSFC of 273.17 g/kWh while the 40% dual fuel strategy had a BSFC of 314.30 g/kWh. This is a 15.1% increase. The increase results from the lower energy density of the n-butanol. This also corresponds to an increase in mechanical efficiency (Soloiu and Gaubert 2018).

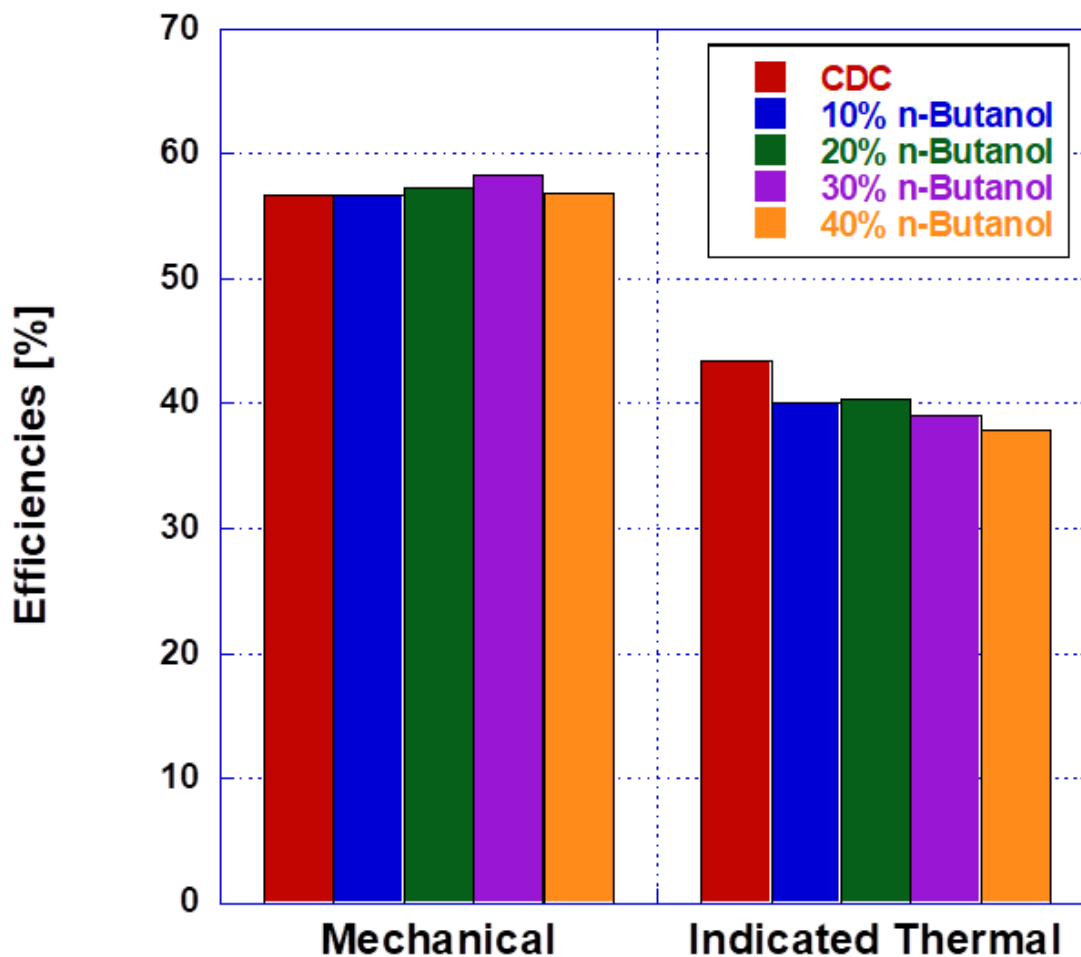


**Figure 67** Mechanical and Thermal Efficiencies for increasing n-Butanol Concentrations

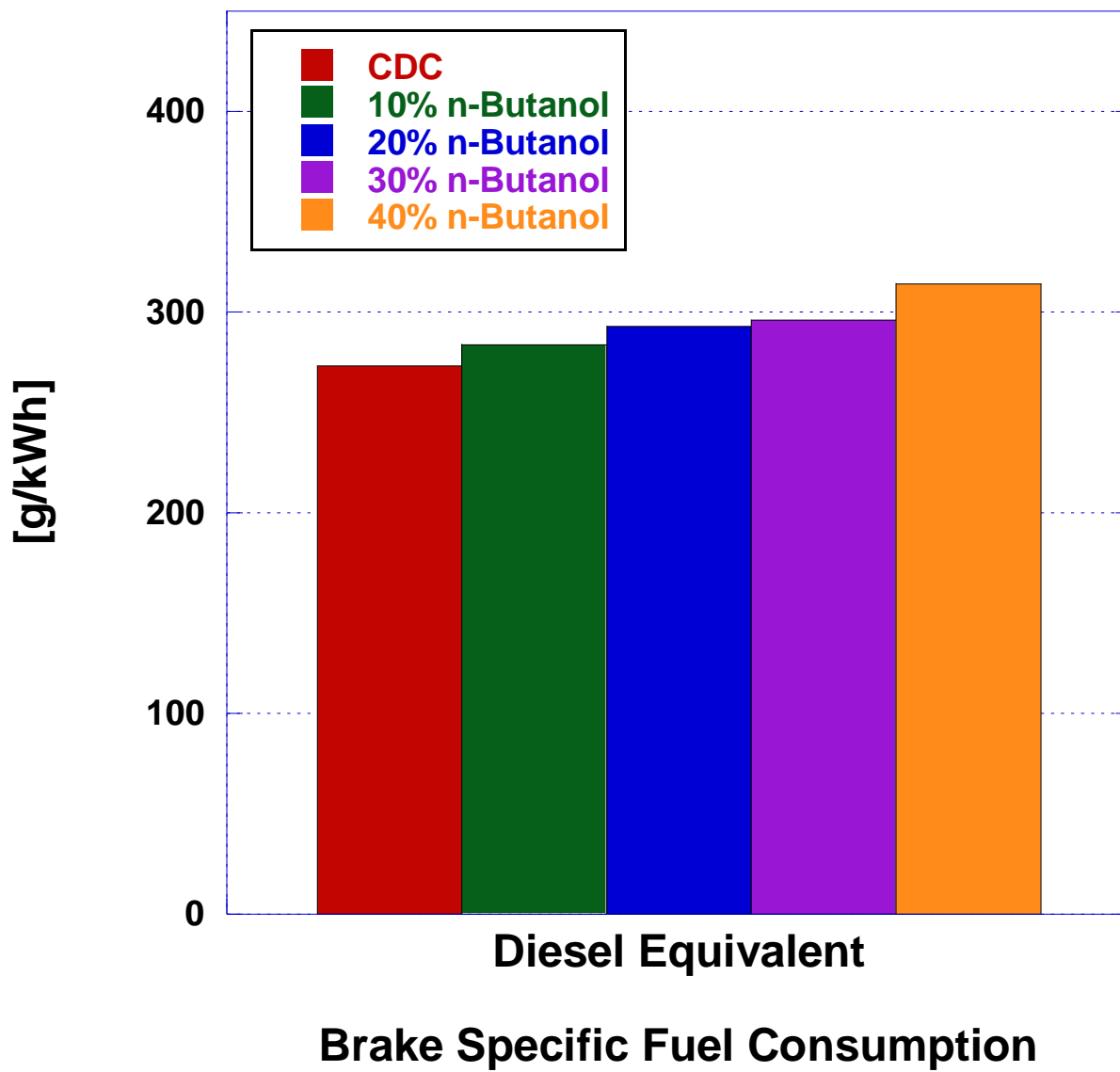


**Figure 68** Diesel Equivalent Brake Specific Fuel Consumption for increasing n-Butanol Concentrations



## CHAPTER 5: CONCLUSIONS

### 5.1 Conclusions

Dual fuel combustion in an indirect injected diesel engine was researched to study its characteristics and exhaust gas emissions.

The hypothesis for research stated: *If a dual fuel combustion strategy involving the port fuel injection of n-butanol is used in conjunction with the indirect injection of ultra-low sulfur diesel, then engine out emissions for nitrogen oxides and soot in single cylinder, off-road diesel engines can be reduced below Tier 4 EPA while maintaining engine performance.* Combustion results validate the stated hypothesis with significant reductions being made in both NO<sub>x</sub> and soot emissions. At 2400 rpm and 3 bar brake mean effective pressure a 21% reduction in NO<sub>x</sub> from a maximum of 3.0 g/kWh to a minimum of 2.4 g/kWh was observed due to the cooling effect of the butanol. Soot emissions were reduced by 80% from 0.37 g/kWh to 0.073 g/kWh due to more complete combustion caused by the increased oxygen content of the butanol. Port fuel injection also allowed for greater in-cylinder mixing which created a more homogenous mixture, reducing fuel rich areas across the chamber. Peak reductions were all made at the 30% butanol mass flow rate.

Combustion pressure results show an increase in peak pressure with increasing mass flow rates of n-butanol. For the highest concentration of butanol tested at 40% of the total fuel flow rate, displayed pressure rise rates 127% higher than that of conventional diesel combustion. This is due to the volatility of the alcohol fuel and the increased mixing from injecting butanol into the intake manifold. Peak heat release rates were observed to increase with the mass flow rate of butanol with a 30.5% increase between CDC and the 40% dual fuel combustion strategy. The increase in peak

pressure, maximum pressure rise rates, and heat release rates can be attributed to the shorter ignition delay and combustion duration. Both decreased with increasing butanol mass flow rates. This contradicts what would be expected given the alcohol based fuel's lower cetane number when compared to neat ULSD#2. This is a result of both the chemical and physical properties of the fuel as well as the injection strategy. The volatility of n-butanol and its' lower viscosity promoted increased atomization and evaporation. When combined with the increased mixing time obtained by injecting into the intake manifold a more premixed charge is introduced into the combustion chamber. Overall a 3.6% decrease in ignition delay and a 31.6% decrease in combustion duration was observed between CDC and the 40% dual fuel strategy.

Peak temperatures remained consistent around 1800 K. Ringing intensity for dual fuel strategies exceeded that of CDC, increasing with the increasing mass flow rates of butanol. RI for the 40% dual fuel strategy was the highest. This was a result of the substantial increase in peak pressure rise rates for this fueling strategy. The lowest RI for the dual fuel strategies was for the 20% dual fuel strategy which was higher than CDC by 6.2%. The heat flux was increased with increasing butanol content. Butanol blends increased the heat flux from the high vaporization rate of the fuel. Carbon monoxide and unburned hydrocarbon emissions increased by 2461% and 1091% respectively for the 40% dual fuel strategy. This results from CO being unable to fully oxidize because of the decreased combustion duration and the increase in the total amount of fuel present at the time of combustion. UHC emissions increased as a result of butanol passing straight through the cylinder during valve overlap as well as the increased lower air/fuel ratios caused by the increase of fuel in cylinder from the alcohol injection. Despite increases  $\text{NO}_x + \text{NMHC}$  emissions for all fuel strategies remained below EPA standards. CO emissions exceeded EPA

standards once the flow rate of n-butanol reached 20%. Optimization of the injection timing for both the port fuel injector and main injector could reduce both CO and UHC emissions.

Mechanical efficiencies were 1-2% higher for the alcohol fumigation strategies with the maximum occurring with the 30% dual fuel strategy. This was a result of the higher cylinder pressures observed as well as negating parasitic losses due to the external injection pump for the n-butanol. Indicated thermal efficiencies decreased with increasing n-butanol concentration. CDC had the highest ITE at 43% and dropped to the lowest at 37.8% for the 40% dual fuel strategy. This occurred because the total fuel energy increased with the increasing n-butanol concentration. A linear decrease was seen in diesel equivalent BSFC from CDC to the 40% dual fuel strategy. The largest contributor to this result is the lower energy content of n-butanol. *Comparing parameters suggests that the optimum dual fuel mode is at the 20% flow rate.* RI intensity is at a minimum for the dual fuel combustion modes, indicated thermal efficiency reaches a maximum of 40% for the dual fuel modes, mechanical efficiency is close to the maximum at 58%, and significant reductions in both NO<sub>x</sub> (19.8%) and soot (62%) are achieved. CO monoxide emissions do increase past EPA standards here but could be reduced through optimization of the injection timing. The combustion and emissions characteristics for dual fuel combustion displayed promising results with potential to reduce emissions in cylinder and promote the increase use of renewable fuels.

## 5.2 Future Work

This study focused primarily on the effect the mass flow rate of the butanol would have on combustion characteristics and emissions. There are many factors that influence the production of gaseous emissions including the injection timing, operating speed, operating load, and the use of

exhaust gas re-circulation (EGR). Through the development of an EGR system NO<sub>x</sub> emissions could be further reduced. The effect that injection timing would have on carbon monoxide and unburned hydrocarbon emissions could also be explored.

## REFERENCES

- Abu-Qudais, M., Haddad, O., Qudaisat, M. 2000. "The effect of alcohol fumigation on diesel engine performance and emissions." *Energy Conversion and Management*, Volume 41, Issue 4, Pages 389-399, [https://doi.org/10.1016/S0196-8904\(99\)00099-0](https://doi.org/10.1016/S0196-8904(99)00099-0).
- Al-Hasan, Mohammad Ibrahim, and Muntaser Al-Momany. 2008. "The Effects of Iso-Butanol Diesel Blends on Engine Performance." *Transport*, 23:4: 306-310, <https://doi.org/10.3846/1648-4142.2008.23.306-310>
- Amann, C., Stivender, D., Plee, S., and MacDonald, J. 1980. "Some Rudiments of Diesel Particulate Emissions." SAE Technical paper 800251. <https://doi.org/10.4271/800251>.
- ANSYS Inc. 2013. "ANSYS Fluent Theory Guide." Canonsburg, PA.
- Arduino. 2018. "Getting Started with Arduino and Genuino MEGA2560."  
Last modified January 11, 2017; Accessed October 20, 2018;  
<https://www.arduino.cc/en/Guide/ArduinoMega2560>
- ASTM D240-17, Standard Test Method for Heat of Combustion of Liquid Hydrocarbon Fuels by Bomb Calorimeter, ASTM International, West Conshohocken, PA, 2017, [www.astm.org](http://www.astm.org)
- ASTM D7668-14a, Standard Test Method for Determination of Derived Cetane Number (DCN) of Diesel 692 Fuel Oils—Ignition Delay and Combustion Delay Using a Constant Volume Combustion Chamber 693 Method, ed. West Conshohocken, PA: ASTM International, 2014.

Atsumi, S., Hanai, T., and Liao, J. C. 2008. "Non-fermentative pathways for synthesis of branched-chain higher alcohols as biofuels". *Nature*. 451 (7174): 86–9. doi:10.1038/nature06450. PMID 18172501.

AVL Group. 2011. "AVL 415S Smoke Meter G002 Maintenance Guide" Graz, Austria.

Borman, Gary, and Kazuie Nishiwaki; (1987); "Internal-Combustion Heat Transfer." *Progress in Energy and Combustion Science* 1 (1987): 1-46.

Center for Disease Control and Prevention. 2017. "Carbon Monoxide Poisoning." U.S. Department of Health & Human Services; Last modified October 26, 2016; Accessed August 22, 2018; 2018; <https://ephtracking.cdc.gov/showCoRisk.action>.

Chen, Z., Liu, J., Wu, Z., Lee, C. 2013. "Effects of port fuel injection (PFI) of n-butanol and EGR on combustion and emissions of a direct injection diesel engine," *Energy Conversion and Management*, Volume 76, Pages 725-731, <https://doi.org/10.1016/j.enconman.2013.08.030>.

CIMAC WG 17. 2014. "Gas Engines. Methane and Formaldehyde Emissions of Gas Engines." CIMAC Position Paper WG 17.

Cummin, Jr., C. L. 1976. "Early IC and Automobile Engines," SAE paper 760604 in *A History of the Automotive Internal Combustion Engine*, SP-409, SAE Trans, vol. 85.

Dempsey, P. (2007). "Troubleshooting and Repair of Diesel Engines." McGraw Hill Professional. ISBN 9780071595186.

- Dürre, Peter. 2008. "Fermentative Butanol Production." *Annals of the New York Academy of Sciences* (Blackwell Publishing Inc) 1125, no. 1: 353-362.
- Environmental Protection Agency. 1999. "Technical Bulletin: Nitrogen Oxides (NO<sub>x</sub>), Why and How They are Controlled," Office of Air Quality Planning and Standards EPA 456/F-99-006R.
- Environmental Protection Agency. 2003. "Particle Pollution and Your Health" Office of Air Quality Planning and Standards EPA-452/F-03-001.
- Environmental Protection Agency. 2007. "The Plain English Guide to the Clean Air Act" Office of Air Quality Planning and Standards EPA-456/K-07-001.
- Environmental Protection Agency. 2008. "EPA Finalizes Emission Standards for New Nonroad Spark-Ignition Engines." Office of Transportation and Air Quality EPA420-F-08-013.
- Environmental Protection Agency. 2014. " 2014 National Emissions Inventory Report." <https://gispub.epa.gov/neireport/2014/>
- Environmental Protection Agency. 2016. "Nonroad Compression-Ignition Engines: Exhaust Emissions Standards." Office of Transportation and Air Quality; EPA-420-B-16-022.
- H. Burtscher. 2015. "Physical characterization of particulate emissions from diesel engines: a review." *Aerosol Science* 36: 896–932; Accessed August 22, 2018; doi:10.1016/j.jaerosci.2004.12.001
- Heywood. 1988. *Internal Combustion Engines Fundamentals*. McGraw-Hill.
- Imran, A., Varman, M., Masjuki, H.H., Kalam, M.A. 2013. "Review on alcohol fumigation on diesel engine: A viable alternative dual fuel technology for satisfactory engine performance

and reduction of environment concerning emission,” *Renewable and Sustainable Energy Reviews*, Volume 26, Pages 739-751, <https://doi.org/10.1016/j.rser.2013.05.070>.

J.A. Eng. 2002. “Characterization of pressure waves in HCCI combustion,” *SAE Int.*  
<https://doi.org/10.4271/2002-01-2859>

Kato, Shoichi, Takanori Hayashida, and Minoru Iida. 2008. "The Influence of Port Fuel Injection on Combustion Stability." *Yamaha Motor Technical Review*.

Kistler Instruments Corp. 1997. "Data sheet, Type 6229A." Winterthur, Switzerland.

Kistler Instruments Corp. 2010. "Dual Mode Amplifier." Winterthur, Switzerland.

Kistler Instruments Corp. 2011. "Miniature Measuring Probe for Non-Cooled Cylinder Pressure Measurement, M5 Thread." Winterthur, Switzerland.

Kistler Instruments Corp. 2013. " Glow Plug Adapter for Cylinder Pressure Measurement in Diesel Engines." Winterthur, Switzerland.

Kistler Instruments Corp. 2017. " High Temperature Pressure Sensor for Cylinder Pressure Measurement in Glow Plug Adapter." Winterthur, Switzerland.

Kittelson DB.1998. "Engines and nanoparticles: a review." *Journal of Aerosol Science* 29(5–6):575–588.

Krzyzanowski M, Kuna-Dibbert B, Schneider J. 2005. "Health effects of transport-related air pollution." WHO, Denmark.

Kubota Engine America Corporation. 2014. "Industrial Diesel Engine Kubota EA Series, EA330-E4-NB1." Lincolnshire, Illinois.



Lapuerta M., Garcia-Contreras R., Campos-Fernandez J., and Pilar Dorado M. 2010.

“Stability, Lubricity, Viscosity, and Cold-Flow Properties of Alcohol – Diesel Blends.” *Energy & Fuels* 24: 4497-4502; Accessed August 20, 2018

Li, J., Yang, W.M., An, A., et al; (2015); “Numerical Investigation on the Effect of Reactivity Gradient in an RCCI Engine Fueled with Gasoline and Diesel.” *Energy Conversion and Management* 92 (2015): 342-352.

Liu, H., Wang, X., Zheng, Z., Gu, J., Wang, H., Yao, M. 2014. “Experimental and simulation investigation of the combustion characteristics and emissions using n-butanol/biodiesel dual-fuel injection on a diesel engine,” *Energy*, Volume 74, Pages 741-752, <https://doi.org/10.1016/j.energy.2014.07.041>.

Majewski, W. Addy, and Magdi Khair. 2006. *Diesel emissions and their control*. Warrendale, PA: SAE International; ISBN: 978-0-7680-0674-2.

Majewski, W Addy. 2012. “What Are Diesel Emissions.” *DieselNet: Diesel Emissions Online*, Ecopoint Inc, [www.dieselnet.com/tech/emi\\_intro.php](http://www.dieselnet.com/tech/emi_intro.php).

Malvern Instruments Ltd. 2006. "Spraytec User Manual." Malvern, Worcestershire: pp. 69-420.

Max Machinery Inc. 2017. "P-Series Positive Displacement - Piston Flow Meters." Healdsburg, California.

Meriam Process Technologies. 2018. "Meriam Laminar Flow Elements." Cleveland, Ohio.

MKS Instruments Inc. 2017. "MultiGas 2030 On-line Gas Analysis." Andover,

Massachusetts.

Norman, A. 2016. Diesel Technology Fundamentals, Service, Repair Eight Edition.

Tinley Park, IL: Goodheart-Willcox Co., Inc

Omron Corp. 2015. "Slim Incremental 50-mm-dia. Rotary Encoder E6C2-C." Kyoto, Japan.

Omron Corp. 2015. "Temperature Controllers E5CS." Kyoto, Japan.

Organization for Economic Co-operation and Development. 2012. "OECD Environmental Outlook to 2050." OECD Publishing. <http://dx.doi.org/10.1787/9789264122246-en>

Park, S.H., Yoon, S.H., Lee, C.S. 2014. "Bioethanol and gasoline premixing effect on combustion and emission characteristics in biodiesel dual-fuel combustion engine." Applied Energy, Volume 135, Pages 286-298, <https://doi.org/10.1016/j.apenergy.2014.08.056>.

Parr Instrument Company. 2014. "1341 Plain Jacket Calorimeter Operating Instruction Manual." Moline, IL.

Qureshi, N., Blaschek, H.P. 2006. "Butanol production from agricultural biomass." In: Shetty, K., Paliyath, G., Pometto, A., Levin, R.E., editors. Food Biotechnology. Boca Raton, FL: Taylor & Francis. p. 525-549.

Resitoğlu, Ibrahim, and Kemal Altinisik. 2016. "Emissions from Diesel Engine and Exhaust After Treatment Technologies." 4th International Conference on Energy, Environment and Sustainable Development, Mehran University of Engineering and Technology, Jamshoro, Sindh, Pakistan. Volume: Version: 01.11.2016; Accessed August 17, 2018;

- Resitoğlu, Ibrahim, and Kemal Altinisik. 2015. "The Pollutant Emissions from Diesel-Engine Vehicles and Exhaust Aftertreatment Systems." *Clean Technology Environmental Policy* 17: 15-27; Accessed August 16, 2018; DOI 10.1007/s10098-014-0793-9.
- Sarjovaara, T., Larmi, M. 2015. "Dual fuel diesel combustion with an E85 ethanol/gasoline blend," *Fuel*, Volume 139, Pages 704-714,  
<https://doi.org/10.1016/j.fuel.2014.09.049>.
- Shimadzu Corporation. 2012. "Thermal Analysis Instruments: 60 Series." Kyoto, Japan.
- Soloiu, V., Duggan, M., Ochieng, H., Williams, D., Molina, G., Vlcek, B. 2012. "Investigation of Low Temperature Combustion Regimes with n-Butanol Injected in the Intake Manifold of a Compression Ignition Engine," ICEF2012-92053 Internal Combustion Engine Division Fall Technical Conference. Vancouver: ASME, 2012. 15. doi:10.1115/ICEF2012-92053
- Soloiu, V., Rivero-Castillo, A., Muinos, M., Duggan, M., Harp, S., Peavy, W., . . . Vlcek, B. 2014. Simultaneous Reduction of NO<sub>x</sub> and soot in a Diesel Engine through RCCI Operation with PFI of n-butanol and DI of Cottonseed Biodiesel. SAE International, doi: 10.4271/2014-01-1322.
- Soloiu, V., Harp, S., Watson, C., Muinos, M. et al. 2015. "Performance of an IDI Engine Fueled with Fatty Acid Methyl Esters Formulated from Cotton Seeds Oils." *SAE Int. J. Fuels Lubr.* 8(2). doi: 10.4271/2015-01-0806.
- Soloiu, V., Gaubert, R., Moncada, J., Wiley, J., Williams, J., Harp, S., Ilie, M., Molina, G., Mothershed, D. (2018) "Reactivity Controlled Compression Ignition and Low Temperature Combustion of Fischer-Tropsch Fuel Blended with n-Butanol", Elsevier *Renewable Energy*, <https://doi.org/10.1016/j.renene.2018.09.047>.

- Soloiu<sup>A</sup>, V., Moncada, J., Gaubert, R., Knowles, A., Molina, G., Ilie, M., Harp, S., Wiley, J. (2018) “Reactivity Controlled Compression Ignition combustion and emissions using *n*-butanol and methyl oleate.” Elsevier Energy, <https://doi.org/10.1016/j.energy.2018.09.181>.
- Soloiu<sup>B</sup>, V., Moncada, J., Gaubert, R., Muinos, M., Harp, S., Ilie, M., Zdanowicz, A., Molina, G. (2018) “LTC (low-temperature combustion) analysis of PCCI (premixed charge compression ignition) with *n*-butanol and cotton seed biodiesel versus combustion and emissions characteristics of their binary mixtures.” Elsevier Renewable Energy, <https://doi.org/10.1016/j.renene.2018.02.061>
- Stone, R. 1993. Introduction to Internal Combustion Engines. Society of Automotive Engineers INC.
- Szybist, J., Boehman, A., Haworth, D., and Koga, H. 2007. “Premixed ignition behavior of alternative diesel fuel-relevant compounds in a motored engine experiment.” Combustion and Flame 149, pp. 112-128. <https://doi.org/10.1016/j.combustflame.2006.12.011>
- Tutak, W., Lukács, K., Szwaja, S., Bereczky, Á. 2015. “Alcohol–diesel fuel combustion in the compression ignition engine.” Fuel, Volume 154, Pages 196-206, <https://doi.org/10.1016/j.fuel.2015.03.071>
- Tutak, W. 2014. ”Bioethanol E85 as a fuel for dual fuel diesel engine.” Energy Conversion and Management, Volume 86, Pages 39-48, <https://doi.org/10.1016/j.enconman.2014.05.016>.
- U.S. Energy Information Administration. 2014. Annual Energy Outlook. Retrieved October 2014, from <http://www.eia.gov/forecasts/aeo/>

- Veltman, M. K., Karra, P. K., & Kong, S. 2009. Effects of Biodiesel Blends on Emissions in Low Temperature Diesel Combustion. SAE Technical Paper, ISSN 0148-7191.
- Vivid Racing LLC. 2018. "RC Engineering 155 CC Peak & Hold Low Impedance Injector." <https://www.vividracing.com/engineering-155cc-peak-hold-low-impedance-injector-p-151344014.html>.
- Wang TJ, Baek SW, Lee JH. 2008. Kinetic parameter estimation of a diesel oxidation catalyst under actual vehicle operating conditions. *Ind Eng Chem Res* 47:2528–2537
- World Health Organization. 2007. "Estimated deaths & DALYs attributable to selected environmental risk factors, by WHO member state." Department of Public Health & Environment.